Development and Validation of a Numerical Model of the CO_2 Dry-ice Blasting Process for Aircraft Engine Cleaning Applications

by

Arthur Rudek M.Sc., B.Eng.

A thesis submitted in partial fulfilment of the requirements for the degree of Doctor of Philosophy (PhD) of the Dublin Institute of Technology

Volume 2/2

School of Mechanical and Design Engineering

Dublin Institute of Technology

May 2018

Dr. Barry Duignan

Dr. G. Reilly **Prof. Dr.-Ing. Gerald Ruß**

Head of School Supervisors

7 Validation case study

This part of the study was supported by REIS, P. [VI] *and by* MUCKENHAUPT, D. and SCHIEMER, B. [VIII] *and their work was supervised by the author.*

In this chapter an experiment is presented for the validation of the particle breakup and defouling erosion models developed in this work, as implemented in Ansys CFX.

Air flows laden with a number of dry-ice particles are observed in an optically accessible stream channel containing a flat plate target. The disintegration and defouling process of these particles is recorded with HSCs and the main parameters, such as number and size of secondary particles or indentation size in fouling layers are processed and compared to corresponding numerical results.

The target plate angle and air velocity are parametrized within this study and dry-ice particles of random size and shape are injected into the flow. The experiment is set up in a wind-tunnel test-rig and all recordings are made using two HSCs, a digital camera and Prandtl probe measurement. Experimental and numerical results show good overall agreement and it can therefore be concluded that it is possible to predict dry-ice breakup and defouling scenarios with the simulation strategy presented.

Section 7.1 gives an initial overview of the experimental set-up. Section 7.2 presents the numerical modelling of pure air flow and particle tracking through the stream channel, as well as an initial validation study. Finally, the main comparison study between numerical simulation and experiment to determine the predictive capabilities of the novel model implementations in Ansys CFX in conjunction with appropriate simulation set-ups of the validation cases are covered in detail in section 7.3.

7.1 General problem description

A wind-tunnel experiment is designed in order to create an optically accessible validation scenario towards the novel models and this set-up is shown in Fig. 7.1 and 7.2. The main dimensions of the testing section are displayed in both figures. This testing section is directly flanged to the nozzle of the wind-tunnel, which delivers the air flow (a) at various air velocities.

Probe bars (b) and (c) are used for the positioning of Prandtl probes with integrated thermocouples (type K) and these are located at the inlet and the outlet of the rectangular shaped main part of the testing section. These probes are used to measure flow properties such as pressure, velocity and temperature.

Flow profiles can be recorded in both horizontal and vertical directions, as indicated by the red arrows in Fig. 7.1. A number of particles can be introduced into the air-flow via the tubular injection system (d) and these are transported by the flow and impact upon the target plate (e).

The vertical and angular positions of the injection tube as well as the angle of the target plate can be varied, as indicated by the red arrows in Fig. 7.2. The testing section is optically accessible through transparent upper and side walls (f) which make the utilization of HSCs possible for tracking and sizing of

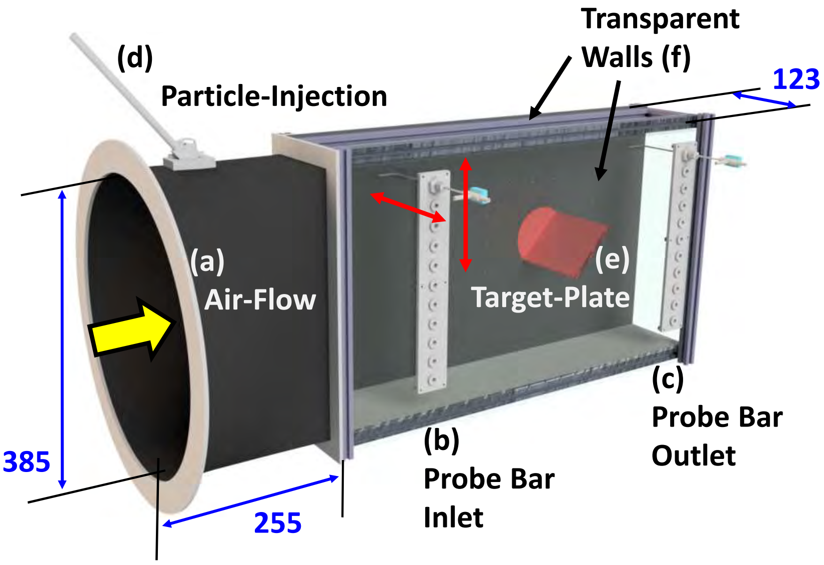

Figure 7.1.: Schematic of wind-tunnel experiment for numerical validation.

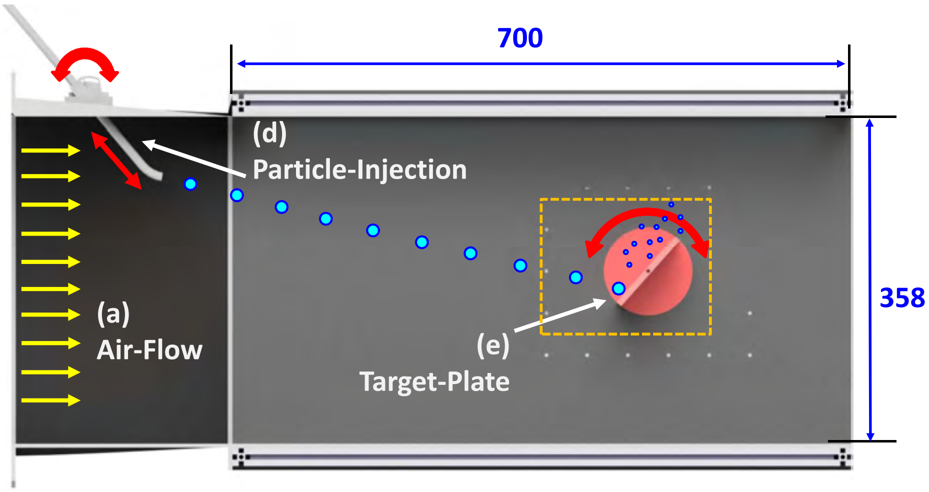

Figure 7.2.: Section view of wind-tunnel experiment for numerical validation.

primary and secondary dry-ice particles. Furthermore, an exchangeable target plate is used for defouling tests (not shown) with which defouling action is measured after a number of particle impacts. To achieve this, images of the target plate surfaces are recorded before and after particle impacts outside the testing section and these are compared by image post-processing.

7.2 Modelling details and run-up study

Initially a pure air-flow run-up study is carried out and it is described in detail in section D.1 to D.3 in the Appendix. A representative selection of results is presented here and these highlight the most important findings of the final particle laden flow simulations. The whole study comprises

- a systematic grid study,
- the discussion of a symmetry assumption,
- comparison of numerical to experimental results for air flow properties.

An overview of the cases investigated is given in Tab. 7.1 and it comprises all parameters considered and summarizes the mean particle impact properties measured. More detailed information about the meshing and the numerical set-up can be found in section D.1 in the Appendix.

Case no.	Nominal air inlet vel.	Nominal target angle	Mean particle impact vel.	Mean particle impact ang.
1	30 m/s	30°	5.79 m/s	51.66°
2	50 m/s	30°	11.71 m/s	53.91°
3	25 m/s	60°	5.02 m/s	21.98°
4	45 m/s	60°	9.65 m/s	26.30°

Table 7.1.: Overview of validation case parameters; air-flow and channel settings (left column block) and mean particle impact values (right column block).

It is assumed that the behaviour of the validation experiment can be numerically predicted by considering a mid-plane cut through the rectangular part of the experimental set-up, assuming periodical symmetry at its sides. This assumption is based on preliminary observations of POM and dry-ice particle tracks. These particles are injected at the mid-channel and in all cases considered they impact the target in the central 33 % of the channel.

In order to show that side wall effects do not significantly influence the mid-plane flow, flow parameters were measured at a grid of locations across a number of vertical and horizontal positions across the section at the inlet and at the outlet planes of the channel. The results from this study are presented in detail in section D.2 in the Appendix. Based on these results and on the above particle tracking observations it was decided to simulate the central 33 % of the channel depth (i.e. a depth of 41 mm) with free-slip conditions at the sides.

7.2.1 Pure air-flow validation

In this section, results from air flow simulations are compared to experimental data recorded in the mid plane of the channel at all vertical positions. Figure 7.3 shows some simulation results of the two most extreme flow conditions (i.e. case #1 with lowest velocity and lowest target angle as well as case #4 with highest velocity and highest target angle).

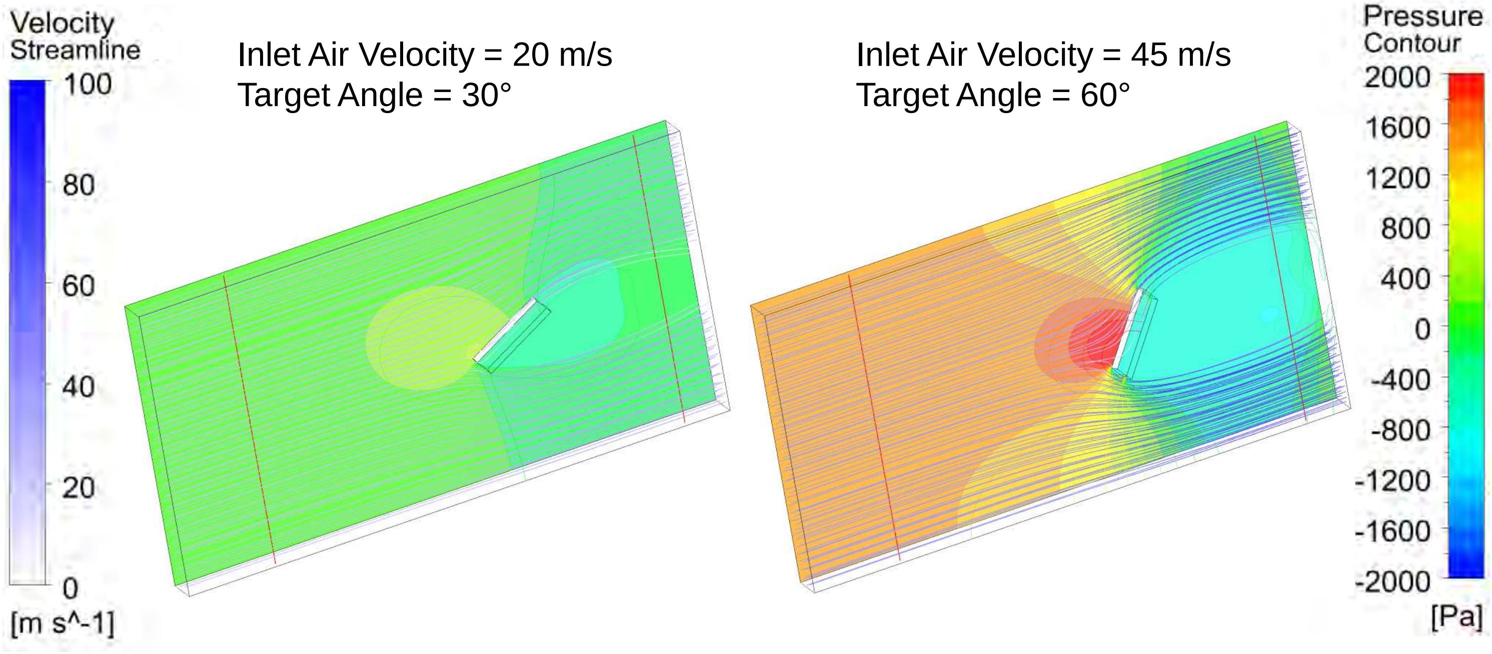

Figure 7.3.: Numerical results for pure air flow in mid-plane symmetry volume for case#1 (left) and case#4 (right) - velocity streamlines and contours of static pressure (NOTE: steady state RANS simulations cannot capture possible velocity fluctuations downstream the target plate, only the mean flow pattern is predicted which is sufficient for the particle model validation cases).

Contours of static pressure are projected to the rear symmetry plane of the numerical volume and velocity streamlines are drawn from the inlet to the outlet plane. A wake region is clearly visible for both cases and the target influence upon the pressure field is also clearly visible. A high forebody and low afterbody pressure field is found to establish and it is mainly influenced by the air velocity and the target plate angle.

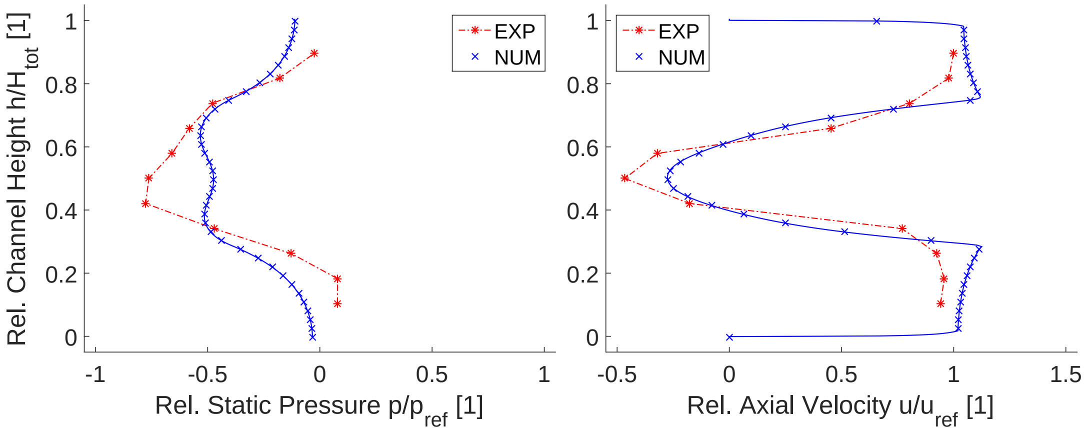

Figure 7.4.: Case#4: air flow pressure (left) and velocity (right) profiles at the outlet plane - comparison of numerical to experimental data.

A typical comparison of pressure and velocity profiles at the outlet measurement plane (both inlet and outlet measurement positions are indicated by the red vertical lines in Fig. 7.3) is shown in Fig. 7.4 for case #4. The predicted pressure and velocity trends are comparable to the experimental data and the mean deviations between predicted and experimental data are 12 % for the pressure profile and 16 % for the velocity profile. A more detailed discussion of this air-flow validation study is presented in section D.3 in the Appendix. Based on these results the set-up is assumed to be valid for the later particle model validation simulations.

7.2.2 Particle tracking validation

In the last step of the run-up study a number of POM particle tracks is experimentally and numerically investigated. The main goal of this study is to assess the predictive capabilities of the particle transportation and impact predictions of the numerical set-up. Particle injection is implemented in the numerical set-up by setting the initial particle velocity vector and its position in vertical direction at the inlet boundary corresponding to data measured in the experiment.

Figure 7.5 shows a montage of typical experimental recordings of a POM particle with a diameter of 3.0 mm at various instants of time pre- and post-impact. The corresponding pre- and post impact angles of the particles are measured with respect to the horizontal plane of the set-up (indicated in the figure). Hence, negative angle values indicate negative vertical particle velocity components. The particle velocity is post-processed with the recordings using the procedure presented in Sections 4.1.2 and A.1.

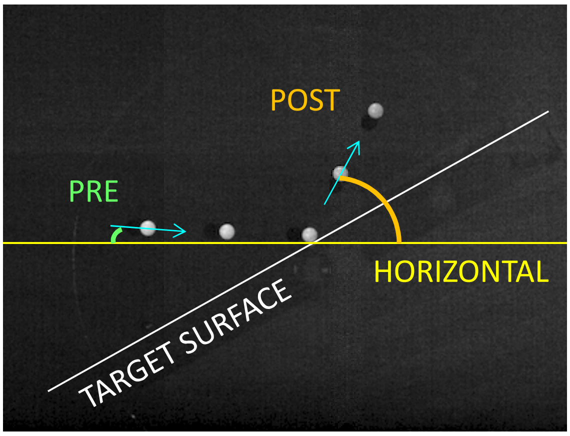

Figure 7.5.: Montage of typical HSC POM particle track recordings at various pre- and post-impact instants of time.

Figure 7.6 shows a comparable result from numerical simulation of this situation and it incorporates a number of POM particle tracks with a diameter of 1.5 mm, high inlet air velocity (i.e. 50 m/s) and low target angle (i.e. 30°). Contours of absolute air velocity are projected to the rear symmetry plane of the numerical volume.

The comparison of the data from this run-up study with POM particles is displayed in Fig. 7.7. The diagram shows the pre- and post-impact flight path angles of the particles (i.e. measured to the horizontal as explained in the discussion of the above Fig. 7.5) and the absolute pre- and post-impact velocity values from both numerical and experimental results. Reasonable agreement

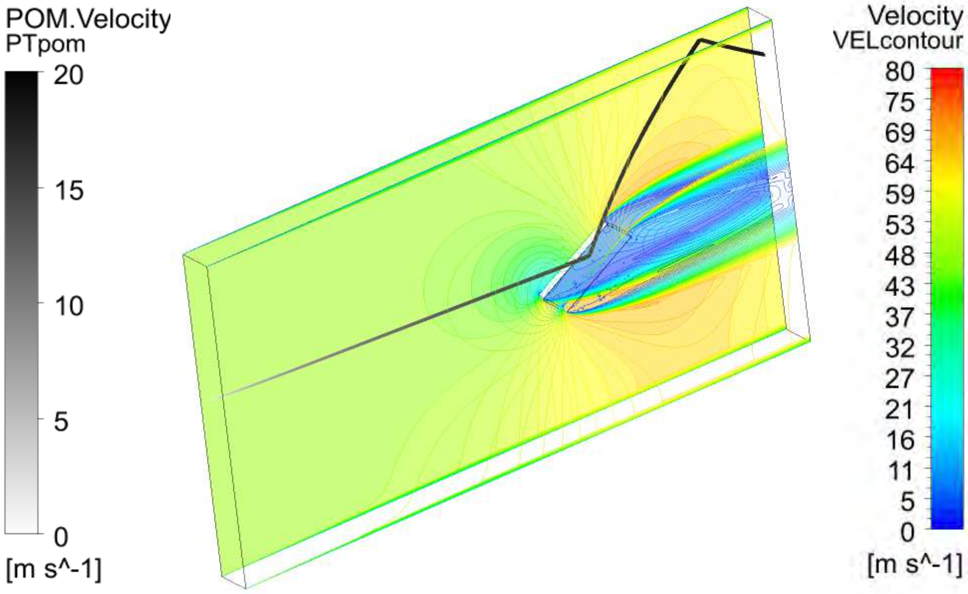

Figure 7.6.: Typical result from POM particle tracking simulations with contours of air velocity.

between numerical and experimental data is achieved with the simulation set-up chosen.

Particle velocities prior to and after the instant of collision with the target plate are found to be precisely predicted. The impact angles are underpredicted and, as a consequence, the outbound angles are overpredicted. These deviations are more significant for larger particles at lower velocities. Possible causes for

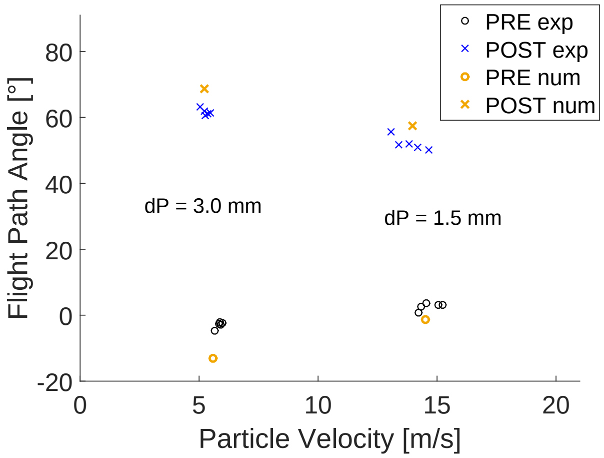

Figure 7.7.: Comparison of numerical and experimental POM particle tracking results - particle impact behaviour.

Case No	Particle Impact Velocity [m/s]	Particle Rebound Velocity [m/s]	Particle Impact Angle [°]	Particle Rebound Angle [°]
1	0.9893	1.0099	0.9566	1.1022
2	0.9570	0.9893	0.8820	1.1133

Tabelle 7.2.: Mean value comparison of validation data for air-flow and particle impingement.

these deviations are the simplifications of the simulation assuming constant coefficients of restitution and neglecting rotation of the particles.

The overall agreement of all numerical data compared to experimental results is satisfactory and a final mean value comparison is listed in Tab. 7.2. The deviations of the velocities range from 1 % to 5 % and these of the angles range from 5 % to 12 %. Parts study were carried out with the opening boundary condition at the outlet of the numerical control volume and this leads to more significant deviations in the pressure profiles prediced at this position which is discussed in detail in section D.3 in the Appendix. However, the particle tracks seem to be independent of these deviations and it can therefore be concluded that the set-up chosen is adequate for all cases considered.

The whole set-up presented above is assumed to be valid for the prediction of the main validation situations presented in the next section 7.3. A grid is used which gives results independent from spatial discretization and the mid plane cut is applied because the above study showed no influence of the side walls upon the particle tracks in the middle of the experimental set-up. In addition, the boundary conditions applied showed no negative influence upon the predicted particle tracks.

7.3 Validation of dry-ice simulations

Based on the initial study described above, the numerical set-up for the main validation case investigations of the newly developed models is chosen. A parameter discussion is presented to determine the predictive capabilities of the models in conjunction with Ansys CFX simulations. Experimental data is recorded for particle breakup and defouling erosion and numerical results are compared to experimental data. The first part of this section describes the particle breakup model study for dry-ice and the second part deals with the new defouling erosion model.

A calibration of various additional parameters of the CFX implementation of the breakup model is necessary before starting the simulations and this is described in detail in section D.4 in the Appendix. These parameters are not originally contained in the model, however, they are useful to avoid possible computational or memory exceptions caused by numerous breakup scenarios and huge amounts of secondary particles in large scale simulations. They increase numerical robustness but decrease the degree of predictive capability of the model. The settings presented in section D.4 for the validation study also represent a possible choice for the final engine defouling simulations.

7.3.1 Particle breakup simulations

Experimental data for the impact and breakup process of dry-ice particles is recorded by means of two HSCs and this situation is displayed in Fig. 7.8. The side view recordings made with HSC #1 are used to determine primary particle size, velocity and impact angle and those made with HSC #2 are used to determine the number and the sizes of secondary particles. The field of view of HSC #2 is focussed to the target plate's trailing edge because it was observed in preliminary recordings that most of the secondary particles pass through this area. This observation is in accordance with the findings that dry-ice particle rebound is almost plastic (i.e. only low normal rebound velocity components are expected). Table 7.3 comprises the most important HSC settings of the experiments.

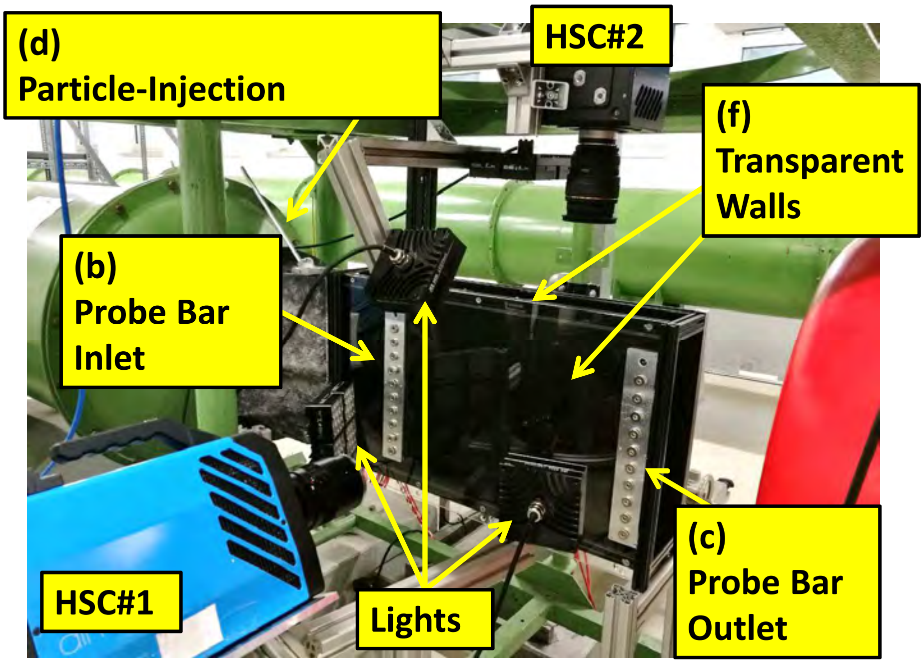

Figure 7.8.: Experimental set-up in particle breakup assessment configuration with two HSCs (note: probe bars are not instrumented).

Typical examples of primary particles impinging the target plate are displayed in Fig. 7.9. The left-hand scene is recorded by HSC #1 and a comparable recording (not the same primary particle) from HSC #2 is shown in the right-hand scene. The tracking and sizing procedures described in Sections A.1 and A.5 in the Appendix are used to post-process this experimental data.

Figure 7.10 shows a typical impact scenario from simulations and it comprises 6 primary dry-ice particles of which 5 impact the target plate at high air velocity (i.e. 45 m/s) and steep target angle (i.e. 60°). These primary particles are disintegrated into 34 secondary particles each and all secondary particle

Camera	Field of View [px x px]	Spatial discrt. [px/mm]	Temporal discrt. [fps]
HSC #1	2016 x 1248	23	2044
HSC #2	2016 x 1248	14 ... 17	2044

Table 7.3.: High speed camera settings for dry-ice validation experiments for the new models.

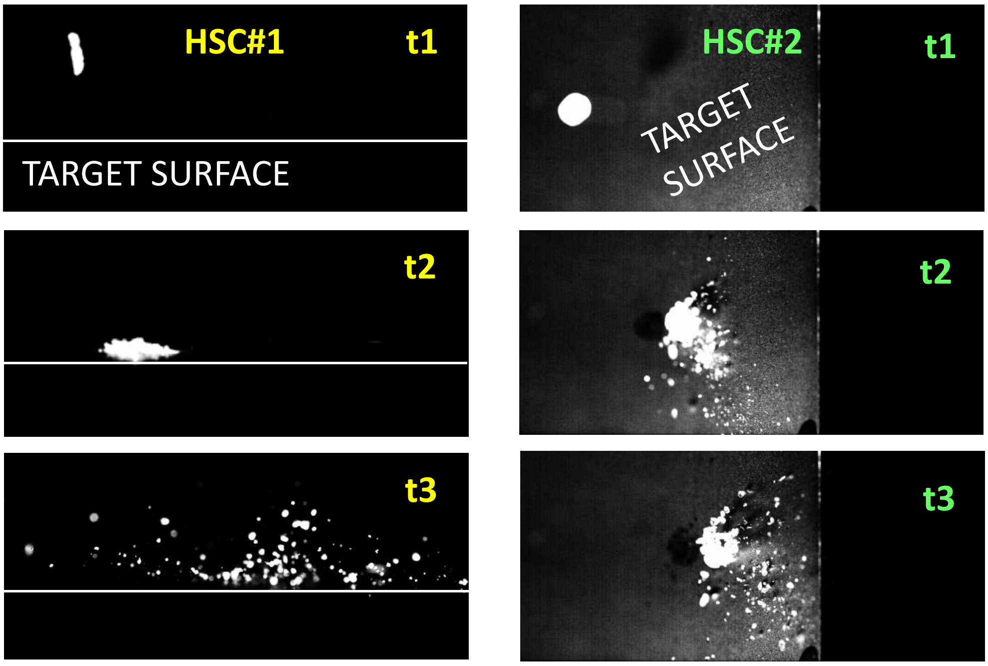

Figure 7.9.: Typical HSC dry-ice recordings of primary particle by HSC #1 (left, showing the side view), and of secondary particles by HSC #2 (right, showing the top view) (note: the scenes do not show the same primary particle).

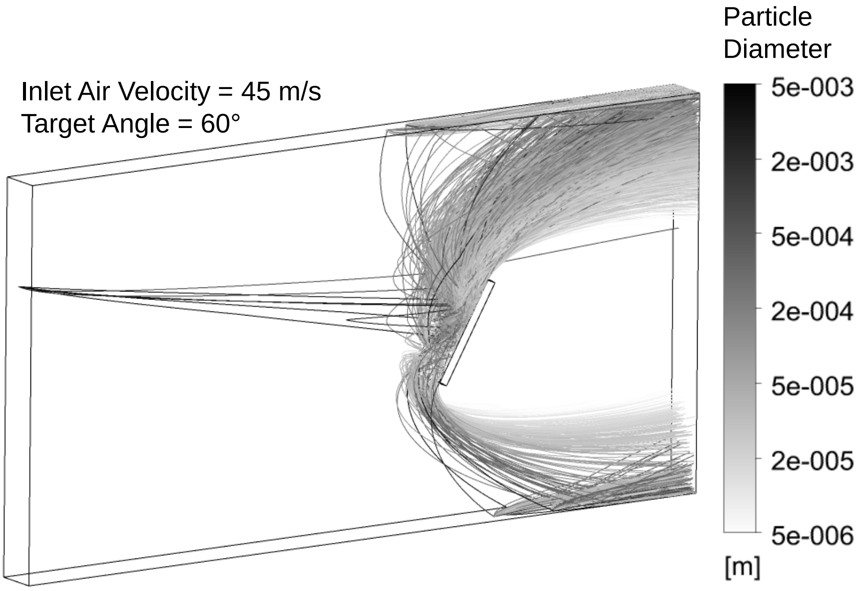

Figure 7.10.: Typical result from dry-ice particle tracking simulations with application of particle breakup model - primary and secondary particle tracks for a number of primary particle impacts.

tracks are displayed. Primary particle sizes are derived from experimental data statistics and a uniform size distribution is assumed at the injection point. The main parameters applied to the CFX implementation of the breakup model, such as the number of secondary particles allowed in the simulations, are listed in Tab. D.4 in the Appendix.

Figure 7.11, left, shows the number of secondary particles generated from primary particle impacts. Equivalent numbers are calculated from predicted number rates in order to make the numerical and the experimental results comparable. Good overall agreement can be seen for the number of secondary particles. The main numerical values are located within the scattering bounds of the experimental data in all cases. In general, the deviations of predicted numbers can be explained by the closing procedure of the CFX implementation of the model, which modifies the number of secondary particles to enforce mass conservation (details are discussed in Sections 5.4.3 and 5.4.4). The mean secondary particle size predictions, presented in Fig. 7.11, right, are also in good agreement with the experimental results and all mean values predicted fit the experimental scattering bounds.

An overprediction of the number of secondary particles and a corresponding underprediction of the mean secondary particle size is detected in the case of low air velocity and low target angle (i.e. 30°, 25 m/s). Additional investigations

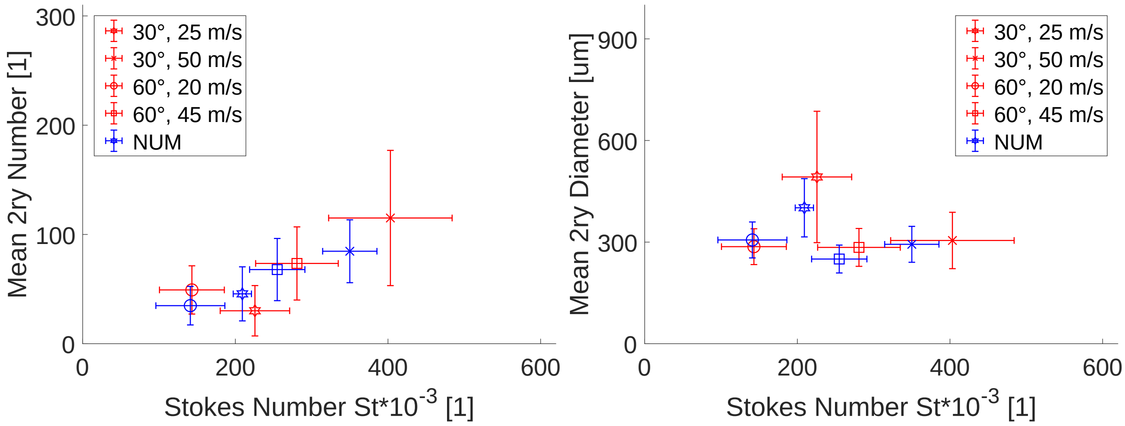

Figure 7.11.: Comparison of numerical to experimental data - number of secondary particles (left) and mean diameter of all dispersed secondary particles (right).

into this particular deviation revealed that the corresponding particle breakup scenarios happen in the mixed breakup zone, which is not accounted for in the model (details are discussed in section 5.3.3). The model only applies the lower boundary between minor and major breakup of dry-ice particles and it can therefore happen that the simulation predicts particle breakup where some of the primary particles do not actually break. As a consequence, more smaller particles are predicted in such situations. The other deviations encountered can be attributed to the closing procedure and to the scattering of the statistical database of the model and of the experiment presented here.

Furthermore, the comparison is extended to the main secondary particle size classes (i.e. residual and debris) and predicted particle sizes of these are compared to experimental data in Fig. 7.12. Both diagrams show good overall agreement of the data. Even in the case discussed above (i.e. 30°, 25 m/s) the predicted particle sizes of the classes are in good agreement with the experimental data. It can therefore be concluded that the model overpredicts the number of secondary debris particles and hence it underpredicts the overall secondary particle size if the primary particle impacts happen in the mixed breakup zone. This indicates that the breakup boundary function applied may be too strict in such cases.

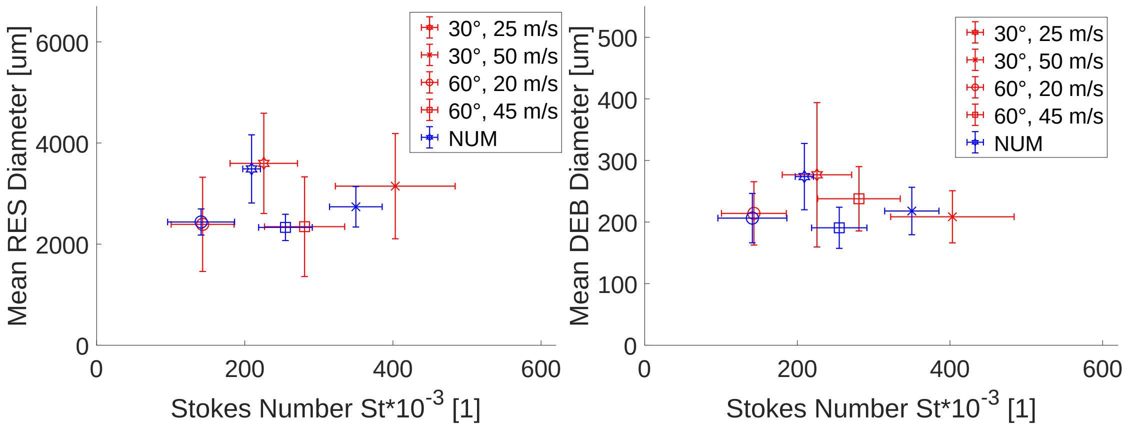

Figure 7.12.: Comparison of numerical to experimental data - mean diameter of residual particles (left) and mean diameter of debris particles (right).

Additional investigation of the upper boundary of this mixed breakup zone and the application of a further random variable are necessary to overcome this systematic issue. However, if the current setting is applied, the model tends to be conservative for defouling erosion predictions, because smaller particles remove lower proportions of fouling compared to larger ones. It is therefore concluded that the application of the boundary function as proposed in section 5.3.3 is acceptable for this work.

The overall agreement of the predicted mean values to the corresponding experimental data is presented in Tab. 7.4 and the general assessment variable, Eqn. (A.6), is used. It can be seen that mean deviations of 5 to 10 % are encountered for the prediction of the secondary particle sizes and that the prediction of the particles of the size classes is more precise than the prediction of the overall particle size. This can be attributed to more significant inaccuracies in the predictions of the numbers of secondary particles which show mean deviations as high as 27 %.

However, there is a significant overlapping of the scattering ranges detected for all values compared. It is therefore concluded that the new breakup model is able to predict the dry-ice breakup process for engineering applications. The range of inaccuracies discussed above is assumed to be adequate given the stochastic nature of the whole process.

Variable ϕ	MAX deviation	MIN deviation	MEAN deviation
n_{SEK}	49 %	8 %	27 %
d_{TOT}	18 %	4 %	10 %
d_{RES}	13 %	1 %	5 %
d_{DEB}	20 %	1 %	7 %

Table 7.4.: Overview of mean value deviations of numerical to experimental results for breakup model variables.

7.3.2 Defouling erosion simulations

The set-up presented above is used to assess the predictive capabilities of the CFX implementation of the novel defouling erosion model. For this reason HSC #2 (top-view recordings) is removed from the experiment and only HSC #1 is used to record the primary particles impacting the target plate. Furthermore, an exchangeable target surface is used, which is coated with either PTFE or SALT and photographed before starting the experiment. After a certain number of primary particle impingements (i.e. 30 - 50 per parameter) the target plate is removed and its partially defouled surface is photographed again. A before-after comparison, comparable to what is described in section 6.3.1, delivers the desired defouling statistics. Figure 7.13 shows a typical result from post-processing and the original image of the defouled surface is compared to the binary outcome from post-processing.

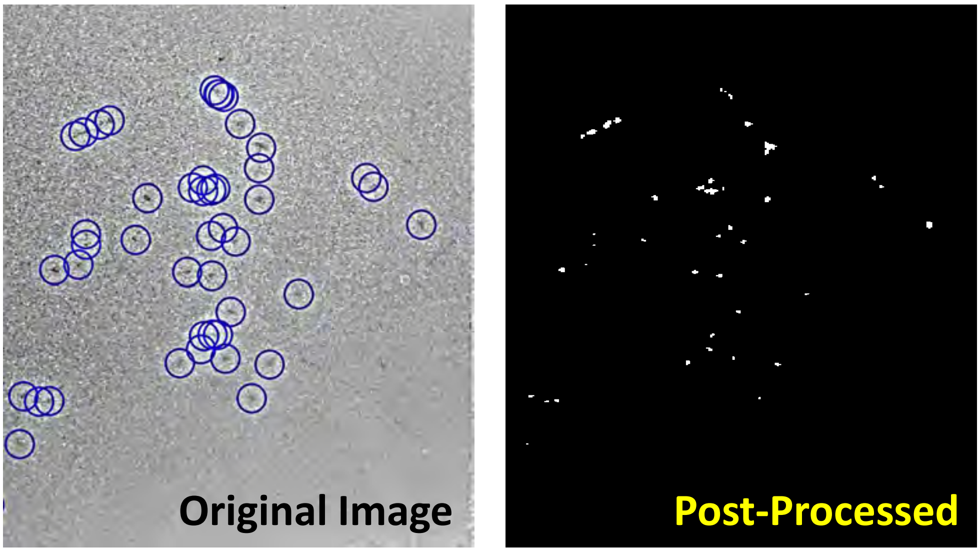

Figure 7.13.: Typical indentation pattern from PTFE defouling (left) and corresponding result from post-processing (right).

Numerical simulations are carried out in a similar manner to those described for the particle breakup model. The primary particle injection position, velocity, direction and size distribution are derived from experimental measurements. Furthermore, the experimental parameters listed in Tab. 7.1 are used for the defouling tests and the two artificial fouling materials, PTFE and SALT, are used for each parameter.

This results in a total of 8 tests, each of which was experimentally carried out twice. In the corresponding numerical simulations a total of 30 primary particles was considered for each parameter. Typical results from numerical defouling predictions are presented in Fig. 7.14: the left-hand image shows little defouling of the SALT layer in the case of 25 m/s nominal air velocity and 30° target angle compared to significant defouling of PTFE with 45 m/s nominal air velocity and 60° target angle.

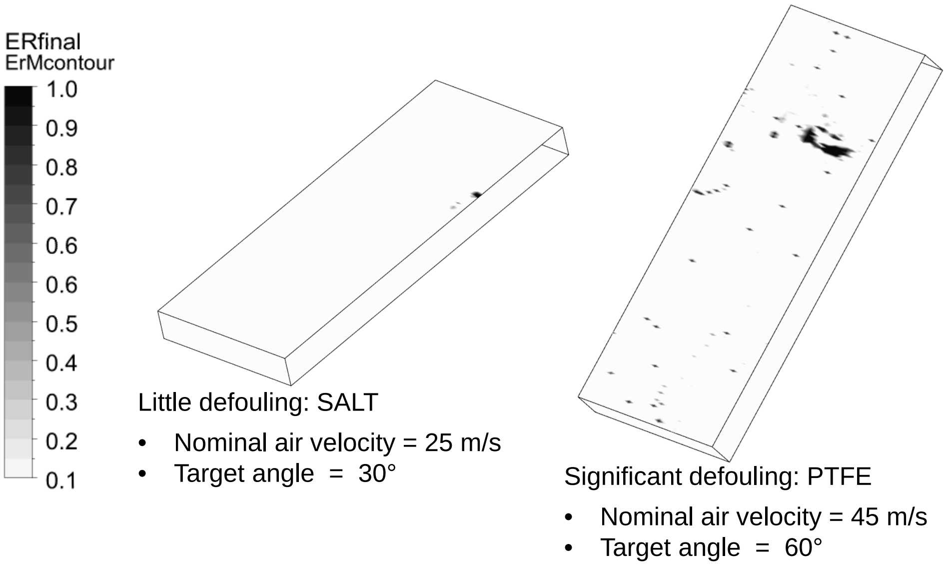

Little defouling: SALT

- Nominal air velocity = 25 m/s
- Target angle = 30°

Significant defouling: PTFE

- Nominal air velocity = 45 m/s
- Target angle = 60°

Figure 7.14.: Typical indentation pattern from defouling simulations - little defouling of SALT coating (left) and significant defouling of PTFE coating (right).

A qualitative comparison of predicted defouling to experimental results is shown in Fig. 7.15 and typical patterns from both SALT and PTFE coatings are displayed. The comparability of the defouling patterns can be seen. From this comparison it becomes clear that secondary particle indentations play a key role in PTFE defouling but this is not the case for SALT. For this reason the first comparison of numerical to experimental data deals with the number of indentations per primary particle and this is presented in Fig. 7.16.

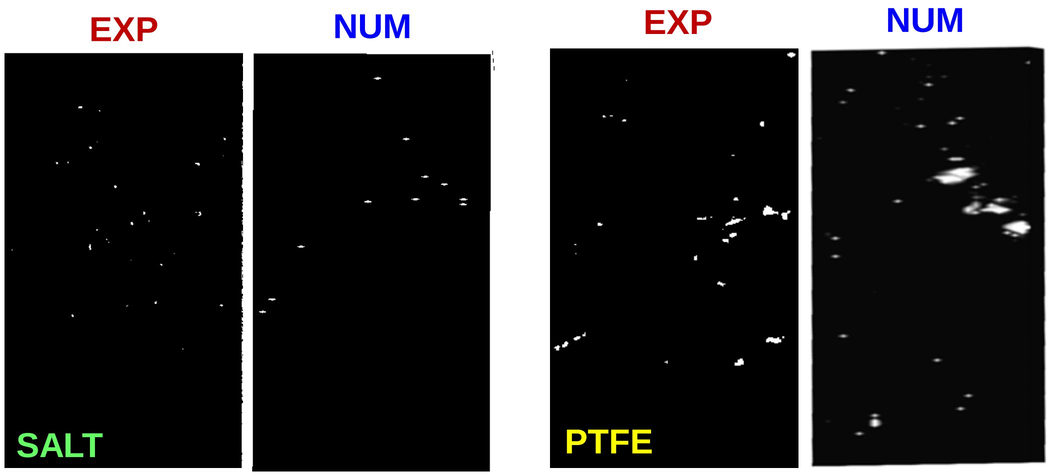

Figure 7.15.: Qualitative comparison of typical indentation patterns from predicted and experimental defouling - SALT (left) and PTFE (right).

The left-hand display shows results from PTFE testing and the right-hand display those from SALT layer investigations. Both diagrams show mean values from 8 experiments and 4 corresponding simulations. Increasing the primary particle Stokes numbers increases the number of indentations per particle and this can be seen for both PTFE and SALT layers. The mean values for PTFE are higher compared to those for SALT. The numerical predictions are comparable to the experimental results and it is therefore concluded that the secondary particle indentations are generally captured by the model set-up presented.

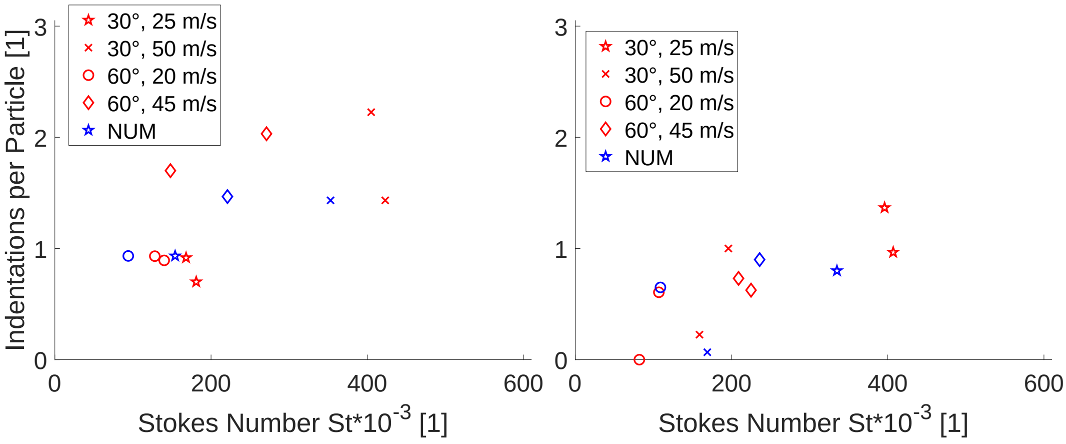

Figure 7.16.: Number of indentations per primary particle from tests with PTFE (left) and SALT (right) - numerical and experimental data.

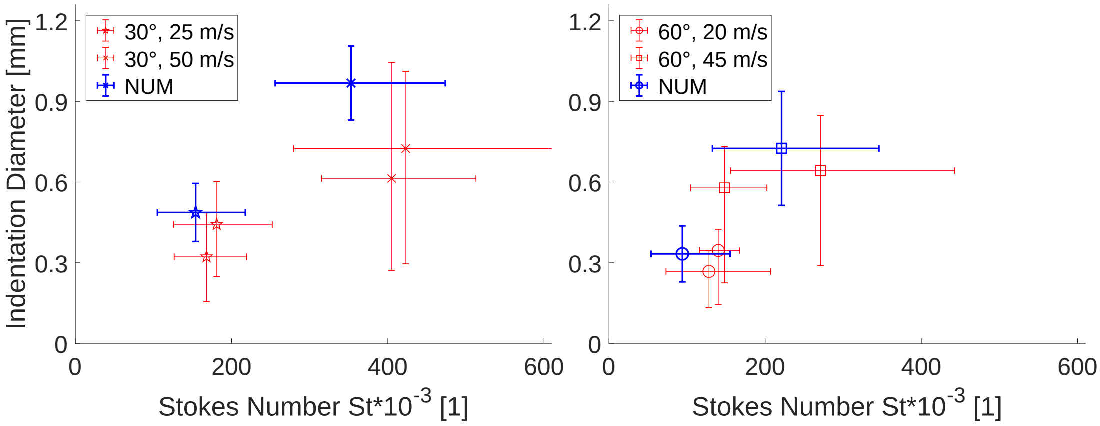

Figure 7.17.: Indentation sizes from tests with PTFE at low (left) and steep target angles (right) - comparison of numerical to experimental data.

The next comparison deals with the indentation sizes after the defouling tests and it is presented for PTFE in Fig. 7.17 and for SALT in Fig. 7.18. The left-hand display of Fig. 7.17 shows the mean values and scattering bars for low target angle (i.e. 30°) and both nominal air velocities and the right-hand graph shows comparable results from steep target angles (i.e. 60°).

In both cases the mean numerical values tend to overpredict the mean experimental outcomes. Good agreement can be seen when comparing the overlapping of the scattering ranges. However, the lower range of indentation diameters is not captured by the simulations. This can be attributed to the actual contribution of very small secondary particles defouling, of which thousands

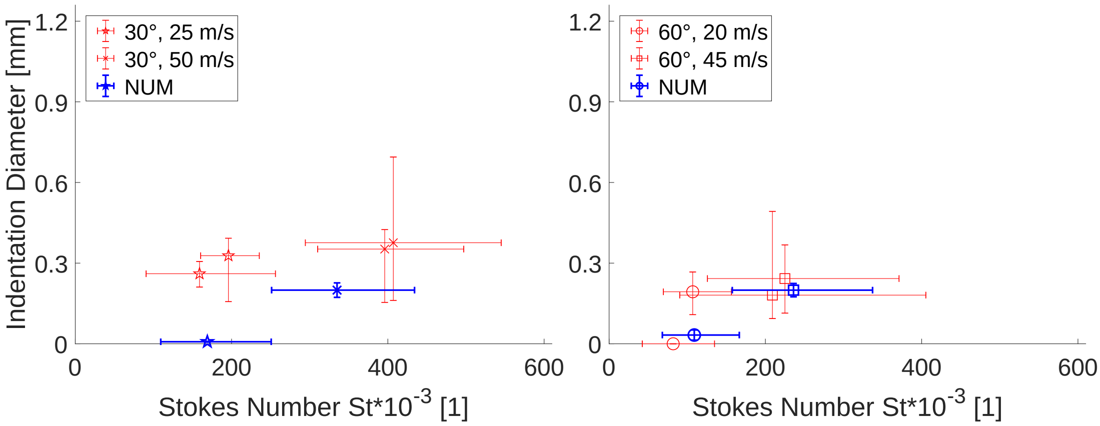

Figure 7.18.: Indentation sizes from tests with SALT at low (left) and steep target angles (right) - comparison of numerical to experimental data.

actually exist but just a number is simulated (see Tab. D.4 and corresponding discussion in section D.4). The predictions for steep target angles are closer to the experimental data compared to these for low target angles.

Results from SALT defouling investigations are presented in Fig. 7.18 in a comparable manner. The mean numerical results for low target angles clearly underpredict the experimental results. In case of the low nominal velocity there is almost no defouling predicted but there are significant indentations detected in the experiment. The predictions for the higher nominal velocity also underestimate the reality, however these are found to be located in the lower scattering bound of the experimental data.

In contrast, the comparison of numerical to experimental data for steeper target angle indentations shows good agreement of the mean values. The predicted scattering bars of the indentation sizes are much narrower compared to the experimental data. A possible cause for this may be natural scattering experimentally encountered for salt layer defouling, which is not accounted for in the model at the moment (details can be found in Sections 6.3.2 and C.3).

Summary

Based on the above results it can be concluded that the CFX implementation of the defouling erosion model adequately predicts actual defouling of PTFE and SALT layers. However, it must be noted that it failed to predict the defouling of SALT at low nominal air velocity and low target angle. The lower bounds of the experimental scattering of the PTFE defouling are not captured by the model. In addition the model underpredicts the scatter for salt defouling.

The mean deviations between numerical and experimental results are summarized in Tab. 7.5. These mean values predicted are in good agreement with the experimental data for steep target angles (mean deviations ca. 15 %) but show significant differences for low target angles (mean deviations ca. 40 %).

The major differences between the PTFE and SALT layer defouling are well predicted for steep target angles and these for the low target angle are found to be within the range of experimental scatter, despite the case where the model failed to predict defouling. Furthermore, the particle breakup model set-up presented in Chapter 5 can be seen to be valid in conjunction with the defouling erosion model because secondary particle indentations are predicted when investigating PTFE defouling.

Case	MAX deviation	MIN deviation	MEAN deviation
PTFE, 30° target	57 %	10 %	38 %
PTFE, 60° target	25 %	4 %	15 %
SALT, 30° target	45 %	43 %	44 %
SALT, 60° target	17 %	9 %	13 %

Table 7.5.: Overview of mean numerical value deviations related to experimental data.

Potential improvement to the defouling erosion model presented can be achieved by the consideration of scattering in the defouling functions. This can be done by introduction of an additional random parameter which must be derived from statistical data processing of the underpinning experiments. Such an additional variable may improve the range of the scatter predicted as well as the prediction of the onset of erosion, which is a solid bound at the moment. This uncertainty is comparable to what was reported above when discussing of the function which describes the onset of dry-ice particle breakup.

Finally, both models are considered to be valid for the prediction of axial aircraft compressor defouling simulations and this final application case is addressed in the next Chapter 8. The mean deviations encountered in the validation case study must be kept in mind when discussing results from application case simulations.

8 Application case study

This chapter documents the final application case study. The main common goal of the studies presented in this work is to simulate axial aircraft compressor defouling in a computationally affordable manner. Therefore a comparison study between a number of typical defouling tests conducted with a GE CF6-500E2 engine at the test-rig are compared to corresponding simulations of this defouling procedure. Tests with indicator coating (i.e. PTFE) applied to the high pressure compressor of the engine and with the final prototype set-up of the new “Cyclean” engine wash unit from Lufthansa Technik are selected for this study because, for these parameters, a large experimental database is available and comparison between simulations and experiments can be presented.

The comparison of numerical to experimental cleaning results and of predicted particle sizes and velocities to experimental data shows good overall agreement. These predictive capabilities of the new models developed in the validation case study (see Chapter 7) are confirmed based on the results presented here.

In section 8.1 the test-rig and the experimental set-up are described and in section 8.2 a preliminary study is described which highlights the pure air flow simulations of the compressor of the dry-cranked engine in comparison to experimental data from the test-rig. A best case scenario is described which is used for the later defouling simulations and the most significant simplifications and assumptions concerning the air flow simulations are highlighted. The final section 8.3 presents all relevant information from defouling experiments and those from additional experiments using a high-speed camera (HSC) to generate local particle tracking and sizing data inside the engine during the defouling run. The results from the final defouling simulations are compared to the aforementioned experimental database and good overall agreement is found.

8.1 General problem description

This part of the study was supported by: MUCKENHAUPT, D. [IX] *and by* ENGEL, M. [X] *and their work was supervised by the author.*

The test engine used for the final application case study is a two shaft type and it encompasses a low- and a high-pressure shaft and these shafts are aerodynamically coupled. The low pressure compressor (LPC) consists of three stages and the high pressure compressor (HPC) consists of 14 stages.

The engine is mounted on a stationary test-rig and the high pressure shaft is driven by an external electric motor. It delivers approximately 130 kW shaft power and it can crank the engine at speeds up to 22.5 % nominal speed of the high pressure shaft. In the dry-crank mode, which is investigated for the defouling process, 20 % of this nominal shaft speed is applied (i.e. ca. 2000 rpm). The low pressure shaft turns at approximately 180 rpm if a steady operational state is achieved.

A section view of the engine is shown in Fig. 8.1 and the indicated positions of instrumentation are described below. The engine is equipped with six Prandtl probes with integrated type K thermocouples. These probes are located along the flow path in the compressor and they can be turned (i.e. to

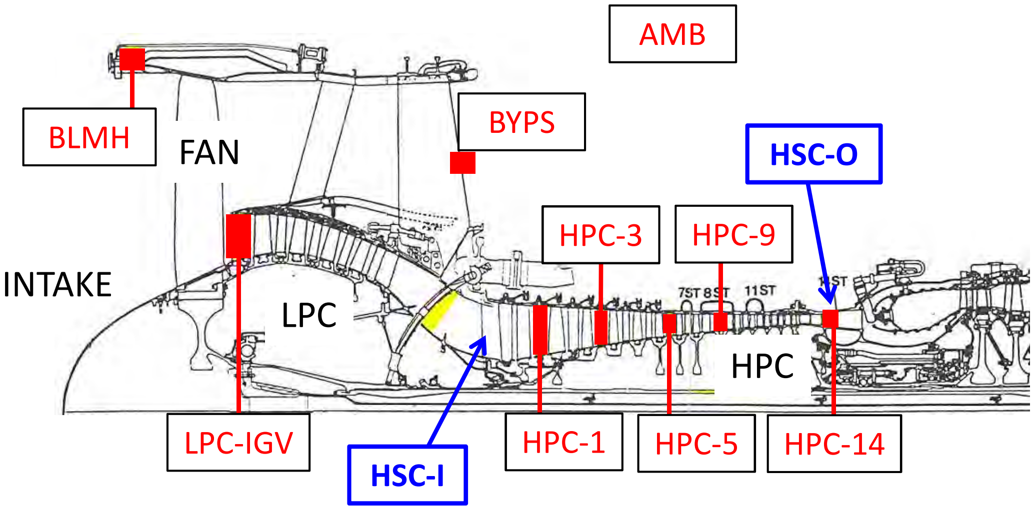

Figure 8.1.: Section view of the test engine GE CF6-50E2 with all relevant instrumentation positions indicated.

measure counter-current flows) and their positions can be varied in radial direction (i.e. to measure span-wise flow profiles). The first probe position is in the IGV row behind the fan (LPC-IGV) and it is followed by five downstream positions in the HPC stages 1, 3, 5, 9 and 14 (HPC-1 to -14). With these probes static and total pressure as well as total temperature are measured.

Furthermore, there is a static pressure probe ring installed in the bell-mouth of the engine (probe name ’BLMH’) and it consists of 12 bores. A hot-wire anemometer is used to measure air velocity at the outlet of the bypass (probe name ’BYPS’) and a static pressure probe and a type K thermocouple are used to measure static pressure and total temperature. Ambient pressure, temperature and humidity are measured away from the flow path. A more detailed description of the probe positioning and measurement concept is given in section E.1 in the Appendix. The corresponding measurement uncertainties have been assessed by MUCKENHAUPT in [IX] and these are summarized in Tab. 8.1 (note: velocity is derived from total and static pressure).

Position	Pressure	Velocity	Temperature
Bellmouth	± 9.5 %	n.a.	± 0.5 %
Bypass	± 4.0 %	± 2.5 %	± 0.5 %
LPC-HPC	± 4.0 %	± 2.5 %	± 0.5 %

Table 8.1.: Measurement uncertainties at various measurement positions in the engine for all variables.

Dry-ice particles are sized and tracked with HSCs placed at specific positions in the high-pressure compressor. Two positions are accessed and these are the IGV row of the HPC (HSC-I in Fig. 8.1) and a position behind the OGV row of the HPC (HPC-O in Fig. 8.1). In the first IGV row three vanes have been removed and their shrouds have been replaced with glass plates. The lighting system and the HSC are mounted in front of these holes as shown schematically in Fig. 8.2.

Similar holes were drilled into the casing at the outlet of the high pressure compressor and the HSC is placed downstream of the OGV row. The uncertainty analysis and post-processing strategy reported in section A.5 in the Appendix also apply for the HSC experiments presented here. The implementation of

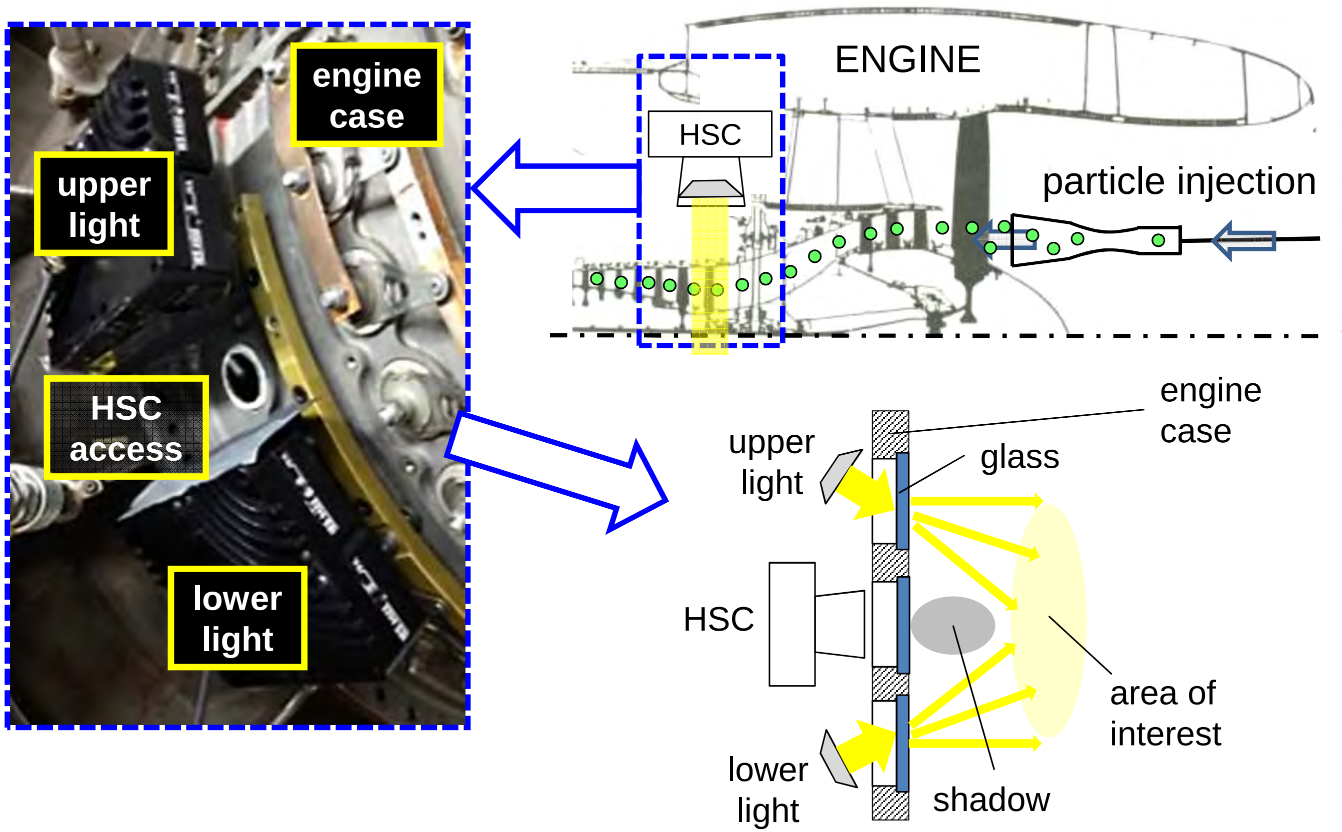

Figure 8.2.: Photography (left) and schematic (right) of the implementation of the HSC measurement for particle sizing and tracking experiments at the test engine.

the HSC technique at the engine test-rig was undertaken by ENGEL [X]; a full description of this experimental set-up and its preliminary results can be found in his thesis.

Figure 8.3 shows photographs of the test-rig equipped for a defouling test run. The left-hand display shows the bell-mouth and the intake of the engine with a prototype of the new dry-ice based LHT-Cyclean wash unit placed in front. At the right-hand side the outlet of the bypass and the beginning of the HPC case can be seen. The LPC is located upstream the HPC and it is surrounded by the bypass.

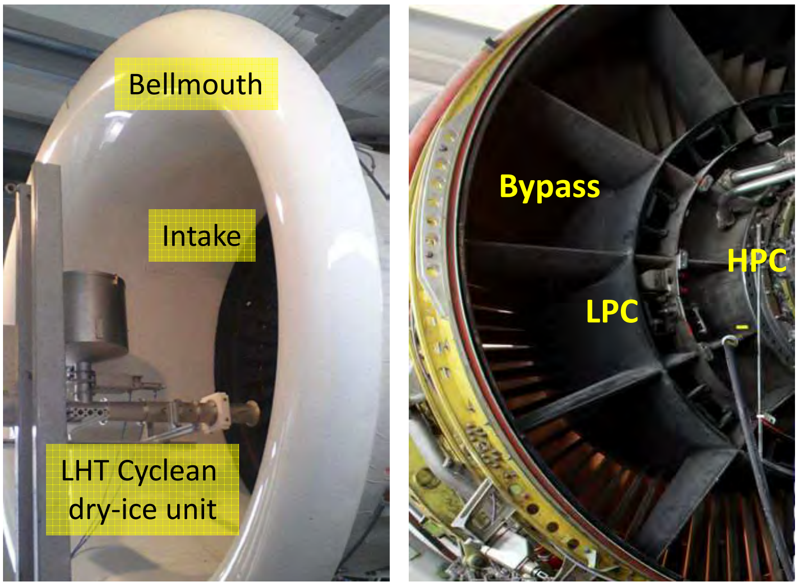

Figure 8.3.: Photographs of test engine GE CF6-50E2, front view with a prototype of the new Lufthansa Technik Cyclean unit installed (left) and rear view (right).

The HPC of the test-engine is accessible and the blading can be removed. The photograph of the opened HPC in Fig. 8.4, left, shows a number of stator and rotor blades before cleaning and the right-hand side image shows the rotor after cleaning of PTFE. It is possible to apply the artificial PTFE fouling in extensive experiments and this data is used to compare the numerical results to experimental results.

The blades are photographed before and after the defouling test outside the engine in a controlled lighting environment and post-processing of these pho-

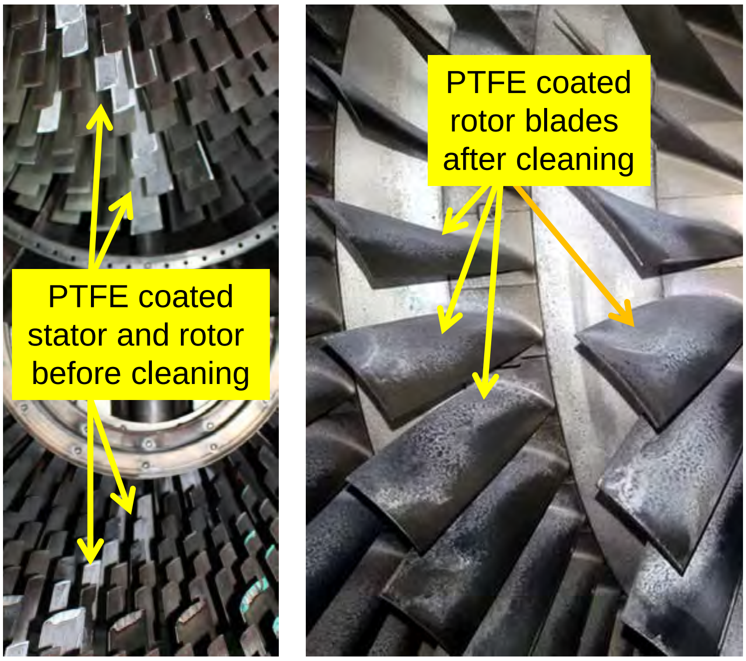

Figure 8.4.: Experiment: opened HPC case with some rotor and stator blades prepared with PTFE (left) and rotor blades after defouling (right).

tographs is carried out with a before-after comparison procedure, comparable to what is described in section 6.3.1. This procedure delivers the desired defouling statistics. Figure 8.5 shows a typical result from post-processing and original images of the defouled surfaces are compared to the binary outcomes

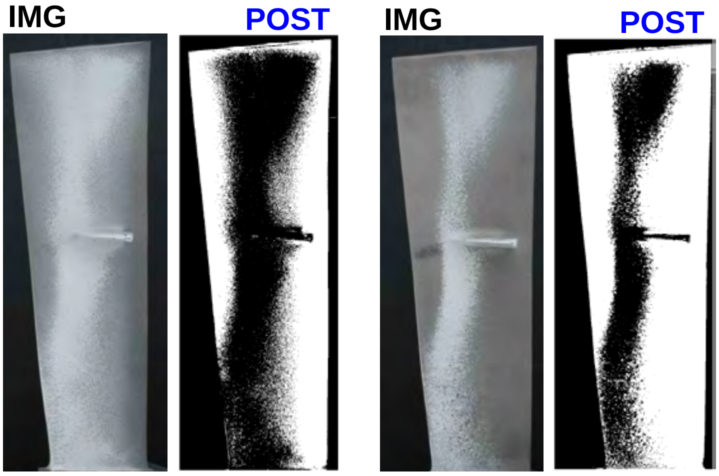

Figure 8.5.: Experiment: typical defouling results from stage 1 rotor blades, original images and post-processing results (note: these blades were not defouled with the Cyclean prototype simulated in this work).

from post-processing. It must be noted that possible curvature of the blading is not accounted for in the post-processing.

8.2 Modelling details and run-up study

This part of the study was supported by: MUCKENHAUPT, D. [IX] *and by* ROSSMEISSL, D. [XI] *and their work was supervised by the author.*

The engine must be simulated with pure air flow in the dry-crank mode before the actual defouling simulations can be carried out. The simulation model is designed assuming periodic symmetry and a stream channel is selected which consists of single airfoils for each row of the engine. There is no grid independence study applied but the simulations are made on a scalable mesh with O-grid meshing of the airfoils and resolved boundary layers. Approximately 100,000 grid-points are used per airfoil passage. The meshing of the engine was carried out by Lufthansa Technik and the ICEM mesher was used. A typical mesh of an airfoil passage is presented in section E.2 in the Appendix.

The stationary and rotational domains are linked by stage interfaces and the mixing plane approach is used to handle the conservation equations (details can be found for example in [9]). The final numerical set-up is shown in Fig. 8.6 and the boundary conditions applied are indicated.

The simulation strategy for the dry-crank mode consists of two steps and the most important set-up details are summarized in section E.2 in the Appendix. In the first step, the set-up is initialized with a numerically stable setting with first order discretization schemes and strong under-relaxation (referred to as step 1). In a second step the numerical damping is lowered and higher order discretization schemes are applied (referred to as step 2). The second step turned out to deliver fluctuating results and these indicate a transient flow state. In order to limit the complexity of the later particle simulations, the steady state approach was assumed to be adequate for this work. However, special attention is paid to the above fluctuations in the discussion of the results below.

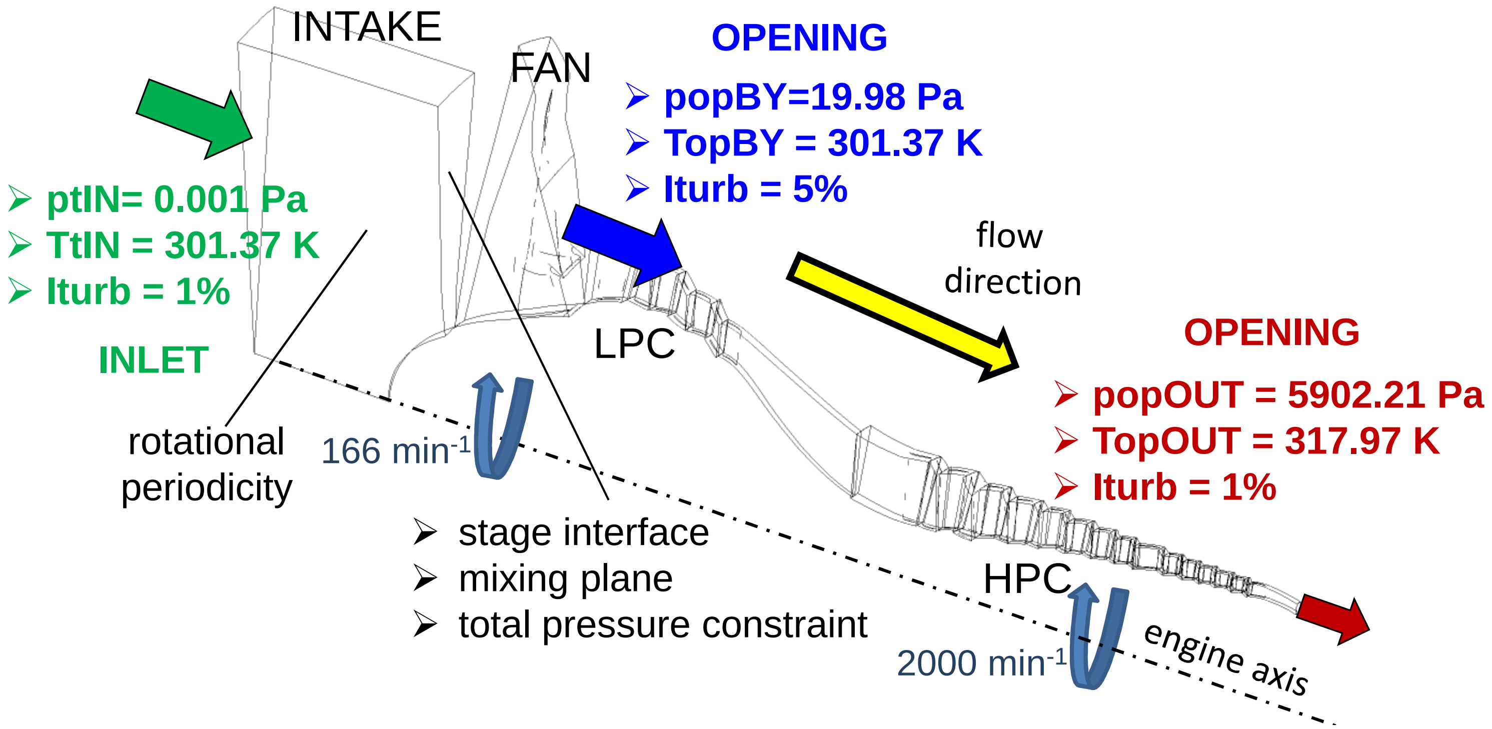

Figure 8.6.: Numerical set-up for CF6-50E2 simulations: boundary conditions and most important modelling assumptions indicated.

8.2.1 Results from the low-pressure compressor section

The numerical results from the LPC area are discussed in this section and the computational pressure and velocity field in stationary frame are presented in Fig. 8.7 in the meridional plane view (i.e. the mid-channel flow between two airfoils is presented). The upper display shows the pressure field and a slight pressure rise can be detected through the LPC. In the lower display, the velocity field shows two separation regions - one at the tip of the fan blades and another one at the OGVs of the LPC. Furthermore, there is a stagnation point visible at the tip of the spinner (note: this is a rotating wall) and a stagnation region is detected at the axis of the stream channel which links the LPC and the HPC (note: this is a non-rotating wall). The predicted velocities are in a range up to18 m/s.

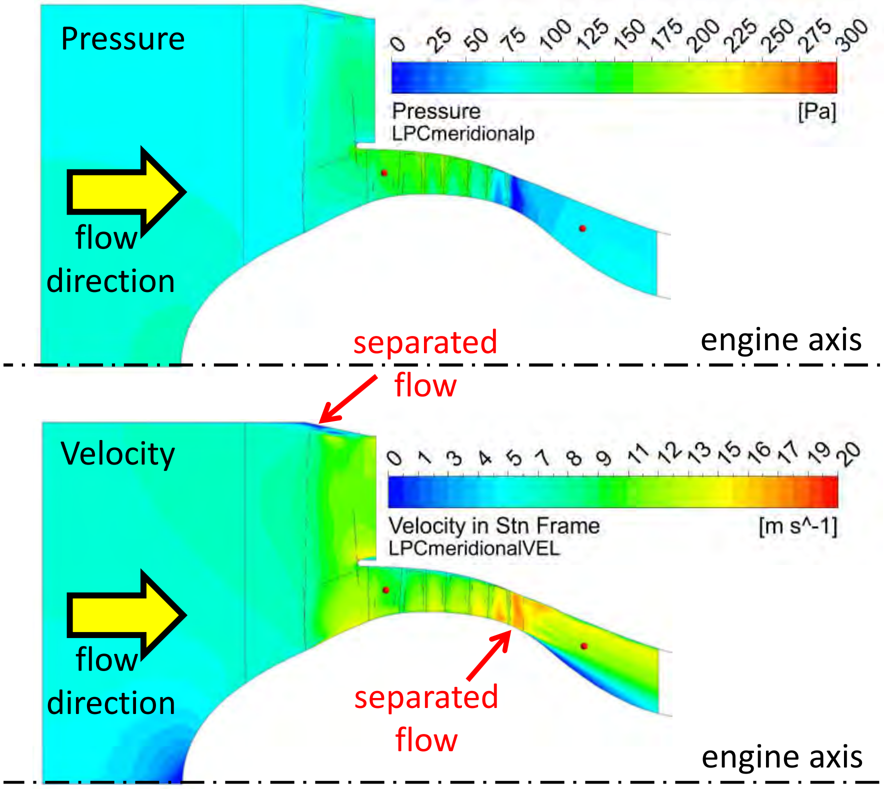

Figure 8.7.: Numerical results of the LPC: contours of static pressure (upper) and velocity in stationary frame (lower) in meridional plane view.

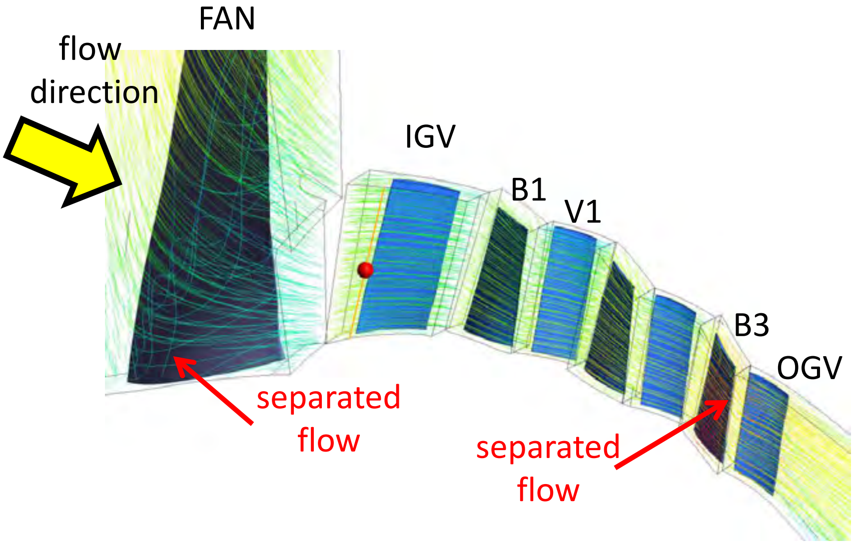

Figure 8.8.: Detailed num. results of the LPC: streamlines (frame dependent representation, i.e. velocity vectors in actual frame).

A deeper insight into the flow development in the LPC is given in Fig. 8.8 where the streamlines throughout the region of interest for LPC defouling simulations are plotted. Disturbances in the streamline formation are predicted at the suction side of the fan blades and at the pressure and suction side of the OGVs. These uneven streamlines at the fan stage influence the main flow field but those at the OGV stage rapidly become uniform downstream. It is concluded, based on these numerical results, that there is an almost undisturbed air flow through the LPC in the dry-crank mode. There is almost no compression effect detected. Furthermore it is found that the numerical fluctuations do not affect the solution of the flow field in the LPC.

8.2.2 Results from the high-pressure compressor section

Comparable results from the same simulations are discussed for the HPC in Fig. 8.9 to 8.11. Pressure, velocity and turbulent kinetic energy are shown in the meridional plane through the HPC in Fig. 8.9. There is a significant pressure rise in the HPC compared to the LPC of up to 10,000 Pa and this is visible from the upper display. A clearly separated flow region is predicted in the velocity and in the turbulence field and it develops at the IGVs and settles at

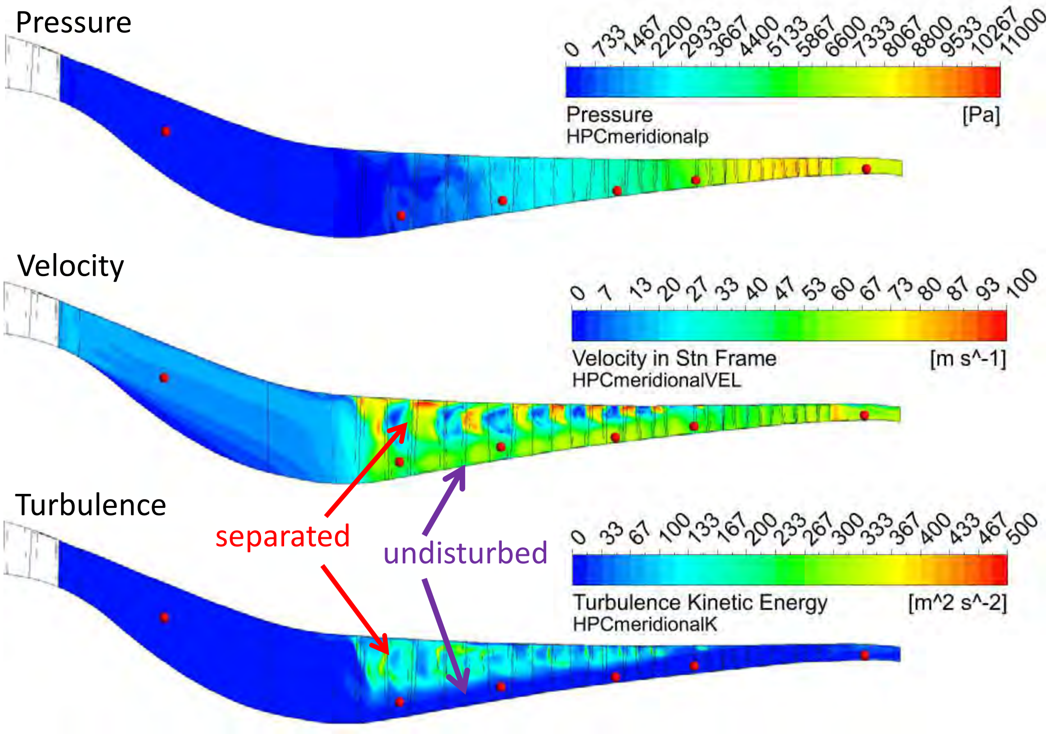

Figure 8.9.: Numerical results of the HPC: contours of static pressure (upper), velocity in stationary frame (mid) and turbulence kinetic energy (lower) in meridional plane view.

the outer part of the HPC. This separation region can be distinguished from the undisturbed region by the disordered velocity contours at the outer part of the engine compared to their regular appearance at the inner part. In the region with the disordered velocity field, high amounts of turbulence kinetic energy are predicted by the applied turbulence model. The predicted disturbance vanishes at the 8th stage of the engine.

Figure 8.10 shows the streamline situation at the inlet into the HPC in detail. There are strong vortices detected and these originate at the root of the IGV and at the tip and root of the first blade. The suction side flow of the first blade is predicted to be almost totally separated. Further downstream the vortex field tends to concentrate in the outer region of the engine. This concentration starts at the first vane row and an undisturbed flow channel establishes at the inner radius of the HPC. The measurement position HPC-1 (indicated by the red sphere in Fig. 8.10) is placed in the middle of this undisturbed flow channel.

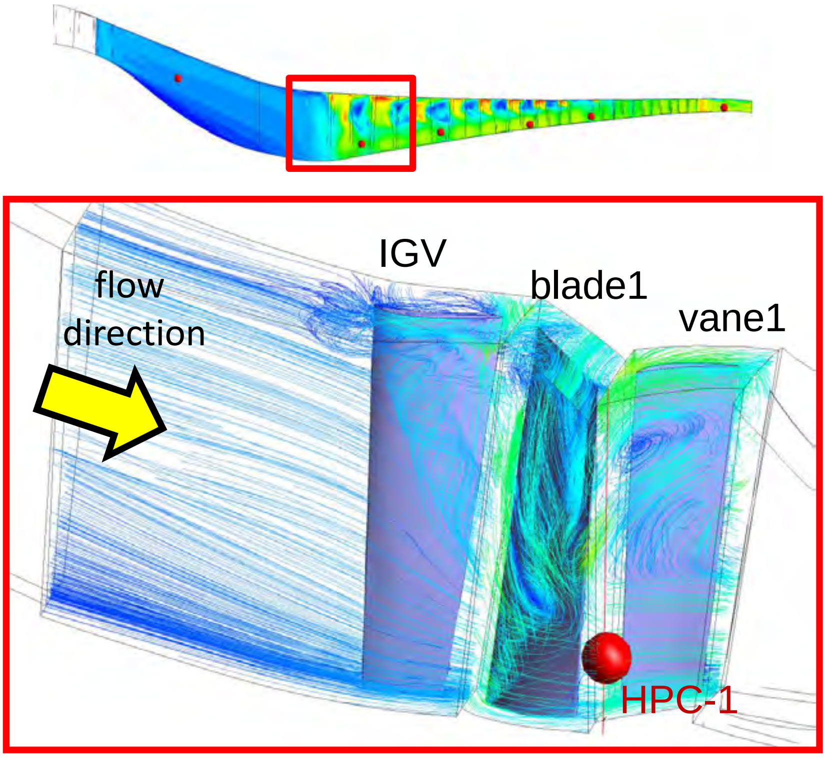

Figure 8.10.: Detailed num. results of the HPC: streamlines at the inlet (frame dependent representation, i.e. velocity vectors in actual frame).

The results presented in Fig. 8.9 indicate that this vortex region disappears at stage 8 where the flow starts to be undisturbed over the whole channel height until it reaches the outlet of the HPC.

The whole separated flow region is shown with streamlines in Fig. 8.11. It must be noted that these results are not strictly steady state and, depending on the number of iterations calculated, the vortex field appears different in the post-processing. Therefore two possible streamline stills are shown in the figure (i.e. at various instants of the numerical convergence process). The corresponding positions of the probes for the mean value comparison, which is discussed below, are indicated in the display.

Based on the examination of the above simulations it is decided to compare numerical to experimental data at various positions in the potentially undisturbed flow channel (i.e. as predicted by simulations) and this comparison study is presented in the next section below.

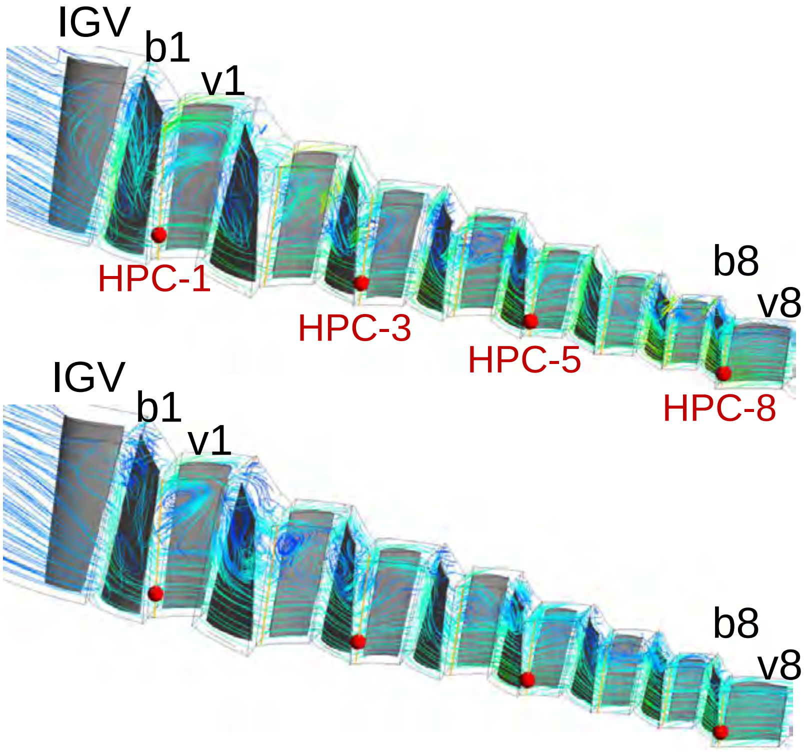

Figure 8.11.: Detailed num. results of the HPC: streamlines up to stage 8 (frame dependent representation, i.e. velocity vectors in actual frame).

8.2.3 Comparison of numerical to experimental flow field

Indicators for the predictive accuracy of the simulations presented above are given in Fig. 8.12 and 8.13 where these predictions are compared to experimental results. The left-hand display in Fig. 8.12 shows trends for static pressure and the right-hand display such for axial velocity values. The corresponding experimental velocities are recorded with the Prandtl probes turned in the axial direction for the measurement and the samples are taken in one single position which is approximately in the middle of the undisturbed flow channel.

These positions were approximated in preliminary experiments and comparison of the results to the predictions are shown in Fig. 8.12. Typical final results from simulations with both set-ups (i.e. step 1 and step 2) are displayed and the values are averaged over the channel height of the undisturbed flow. The ranges of possible numerical fluctuations from the step 2 simulations are highlighted by scatter bars whereas the results from step 1 simulations do

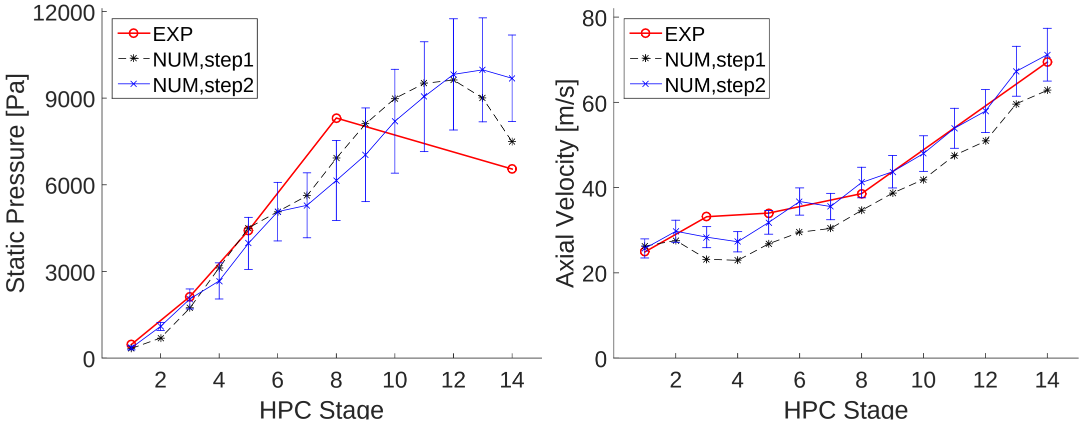

Figure 8.12.: Engine sim. - comparison of num. to exp. data in undisturbed flow channel; static pressure (left) and axial velocity (right).

not show fluctuations. The fluctuations indicate a non-converged numerical solution and transient phenomena which cannot be captured by means of he simulation strategy presented here. However, these effects remain neglected in this project and should be addressed in future work.

The results represent an adequate prediction of the global trends. Differences in the results may be caused by local effects in the probe measurements compared to the averaged numerical values and from the simplifications of the numerical approach. The mean values of both pressure and velocity trends are predicted with a mean accuracy of 16 % by the step 1 simulations, the pressure field is predicted with a lower mean accuracy of 22 % but the velocity field predictions are better with 7 % when using the step 2 set-up.

Experimental axial velocity profiles are shown in Fig. 8.13 for all measurement positions and these are compared to the above simulation results. The span variable shows the relative position along the span of the corresponding vane with 0 representing the hub (i.e. towards the engine axis) and 1 representing the tip (i.e. towards the engine casing). At the measurement positions HPC-1, -3 and -5 there is a clearly visible experimental indication for the flow separation region. In the case of HPC-1 and -3 counter-flow is measured in the experiments (i.e. with turned Prandtl probes). The qualitative velocity profiles in Fig. 8.12 are sufficiently well predicted and the global tends in Fig. 8.13 are in good agreement with experimental data.

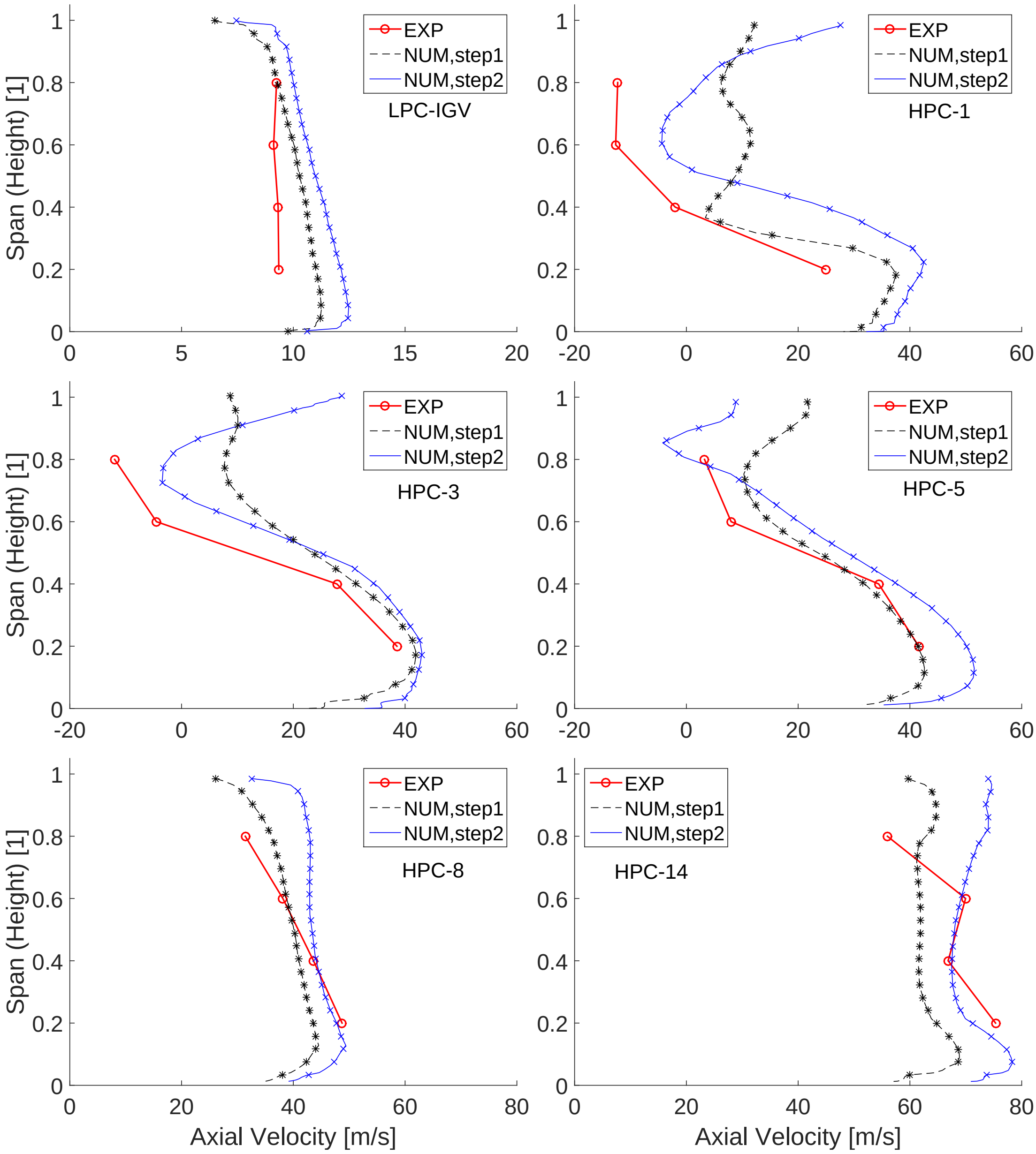

Figure 8.13.: Engine simulations - comparison of numerical to experimental velocity profiles at various measurement positions.

Based on the above discussion it is assumed that it is possible to simulate the dry-crank mode of the engine with a reasonable accuracy for the final defouling simulations presented in this work. Mean pressure and velocity values are predicted with mean accuracies in the range from 7 to 22 % and although the velocity profiles at various stages do not exactly match the measured data, the global trends are recognizable. There are no highly significant deviations encountered given the nature of the operational mode of the engine and the simple numerical approach taken.

The temperature field is not discussed in this work and therefore the temperature field predictions remain unconsidered in this place.

8.3 Application of dry-ice simulations

This part of the study was supported by: ENGEL, M. [X] *and his work was supervised by the author.*

Particular modifications of the numerical set-up are made for the simulations of the defouling procedure. The particle phase is introduced into the region of interest with a boundary patch at the intake of the stream channel model of the engine and this is shown in Fig. 8.14 and explained below.

Although the flow simulations are steady-state, the cleaning information generated is time-dependent. To account for a representative proportion of dry-ice particles in the simulation, the total mass of dry-ice particles used in the actual cleaning process m_{TOT} is scaled to the proportion of the engine considered (first term in parentheses in Eqn. (8.1) below) and to the actual period of time considered (second term in parentheses):

$$m_{SIM} = m_{TOT} \cdot \left(\frac{\alpha_{SIM}}{2\pi} \right) \cdot \left(\frac{N_{SIM}}{n_{LPC} \cdot t_{TOT}} \right) \tag{8.1}$$

and with this the number of simulated dispersed particles is adapted. The equation applies the actual angle of the proportion of the intake considered in the numerical model α_{SIM} and relates it to the whole engine (i.e. 2π). Furthermore, it relates the actual number of rotations considered in the simulation

N_{SIM} to the total number of rotations of the actual defouling process. The latter is obtained by multiplication of the rotational speed of the LPC n_{LPC} with the total process time of the cleaning t_{TOT}. If the whole cleaning cycle would be reproduced in a full engine model, then $m_{SIM} = m_{TOT}$.

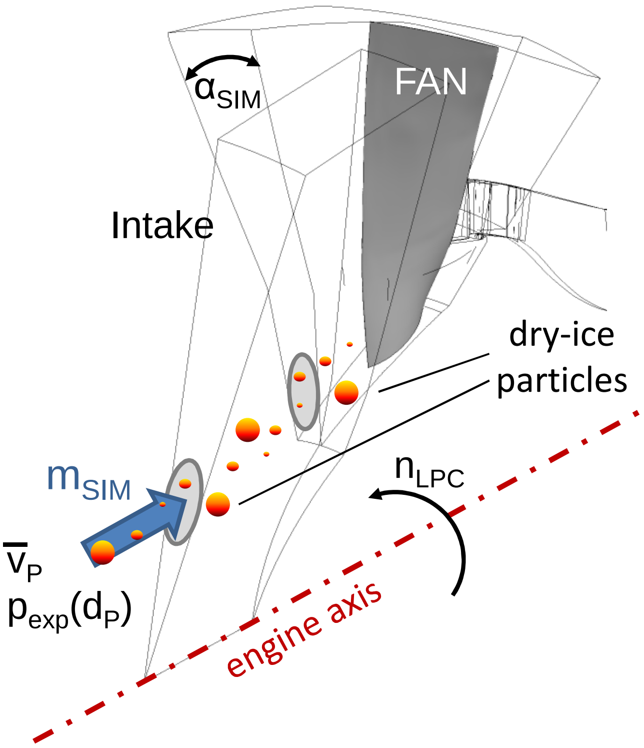

Figure 8.14.: Implementation of the particle phase into the numerical set-up.

The full set of particle boundary conditions if obtained by using the simplified experimental particle size distribution and the mean experimental particle velocity (corresponding experiments are described in section 4.3). The air flow from the injection system and the positioning of the system in the intake of the engine are neglected. To consider this situation, an expensive multiple domain approach (i.e. multiple blades per row) would be necessary and it is not possible to account for this with the symmetry assumption presented here.

The impact of the particle phase upon the air flow in the engine is also neglected in this study and this is done by applying CFX expert parameters to freeze the flow field. This underpinning flow field is calculated before the defouling simulations and this is described in section 8.2. However, it is possible to assess the impact of the particles upon the air flow with an appropriate numerical parameter set using the set-up presented above.

Regarding the influence of the symmetry assumption upon the defouling predictions, it is known from numerous defouling experiments with the test-rig that the rotors of the engine are cleaned equally around the circumference even if the particles are injected at discrete positions. A partial cleaning channel is initially formed in the stator rows and it increases circumferentially as the particles propagate through the compressor. It is assumed that the numerical approach presented here predicts the mean cleaning effect of the rotors and the maximum cleaning effect of the stators in the main cleaning flow. This assumption is discussed below when numerical to experimental results are compared.

The most important model parameters of the CFX implementation of the new particle breakup model must be calibrated before starting the final defouling simulations and this is described in detail in section E.3 in the Appendix.

For implementation reasons it was necessary to simulate the cleaning procedure in two discrete numerical domains for the LPC and for the HPC respectively. These are coupled with an interface at the passage from LPC to HPC and the particle sizes, velocities and their local distribution are set as boundary conditions for the HPC simulations. Hence a new set of particles is used for the HPC simulations. The information for this new set of particles is simplified at the interface and particle size classes are considered, a mean particle velocity is derived and the local particle distribution is generated with a weighted distribution.

8.3.1 Particle breakup simulations

The defouling simulations presented below comprise the assessment of the cleaning of artificially fouled test-engine compressor parts (fouled using PTFE) and the corresponding tracking of dry-ice particles. Periods of 1 %, 10 % and 100 % of the total actual process time are considered by modifying the total mass introduced into the system according to Eqn. (8.1).

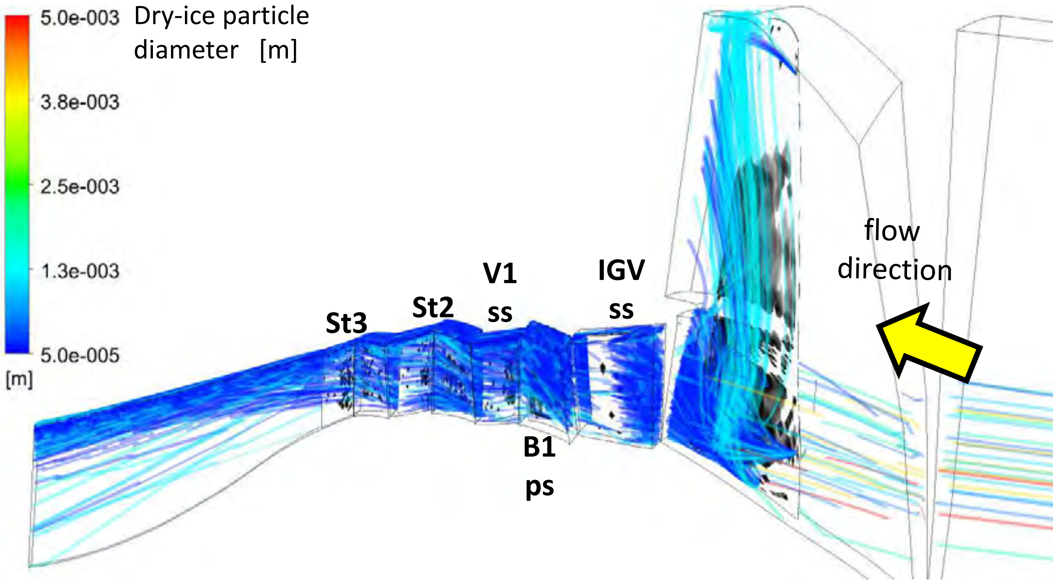

Figure 8.15.: Numerical particle tracks from 1 % process time (only a reduced number is shown): LPC, rotor pressure sides (ps), stator suction sides (ss).

The Figures 8.15 and 8.16 show typical particle tracks in the LPC for the simulation of 1 % of the process time. Particle breakup occurrences can be seen up to

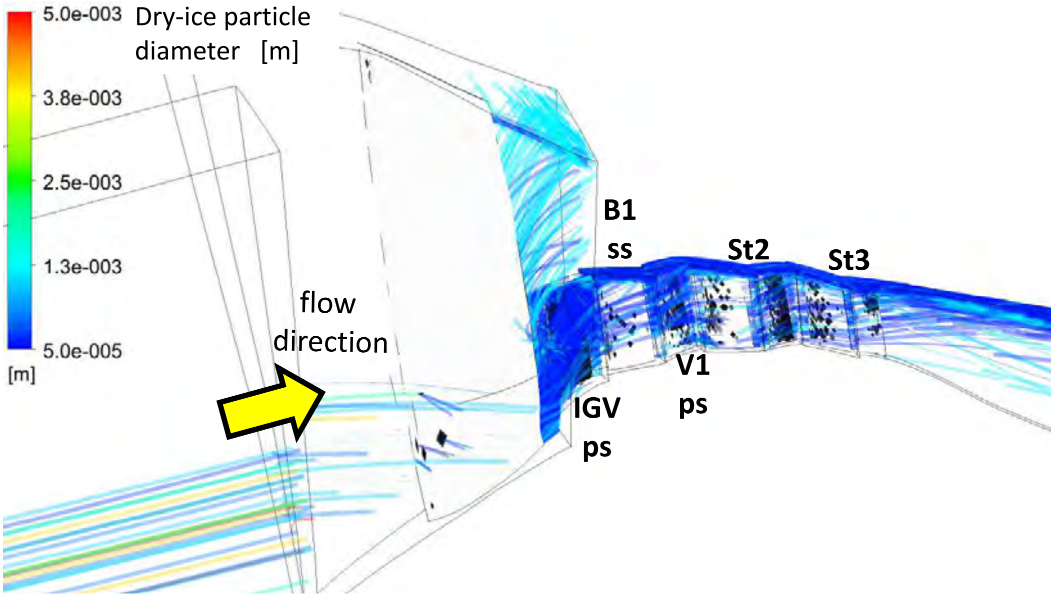

Figure 8.16.: Numerical particle tracks from 1 % process time (only a reduced number is shown): LPC, rotor suction sides (ss), stator pressure sides (ps).

the third stage of the LPC but the predominant disintegration of large primary particles into smaller secondary fragments happens in the fan stage where the particles come into contact with a rotating airfoil for the first time.

The particle phase is dominated by small particles downstream of the fan. A number of large particles is ejected via the fan through the bypass and this phenomenon was also encountered in the experiment. Only a small number of particles is found on the suction side of the fan blade and in general a lower number of particles flows over the suction sides of the blades compared to the pressure sides.

Furthermore, the particles tend to concentrate at the outer radius of the machine when exiting the LPC. However some, mostly large, particles counteract this general behaviour. This phenomenon can be attributed either to the stochastic secondary particle velocities resulting from the breakup process or to the vortex which builds up at the OGV and which may influence these particle tracks at the exit.

The same particle tracking state is analysed for the HPC and this is displayed in Fig. 8.17 and 8.18. Most of the particle breakup, induced by the higher rotational velocity of the HPC compared to the LPC, can be seen in the first

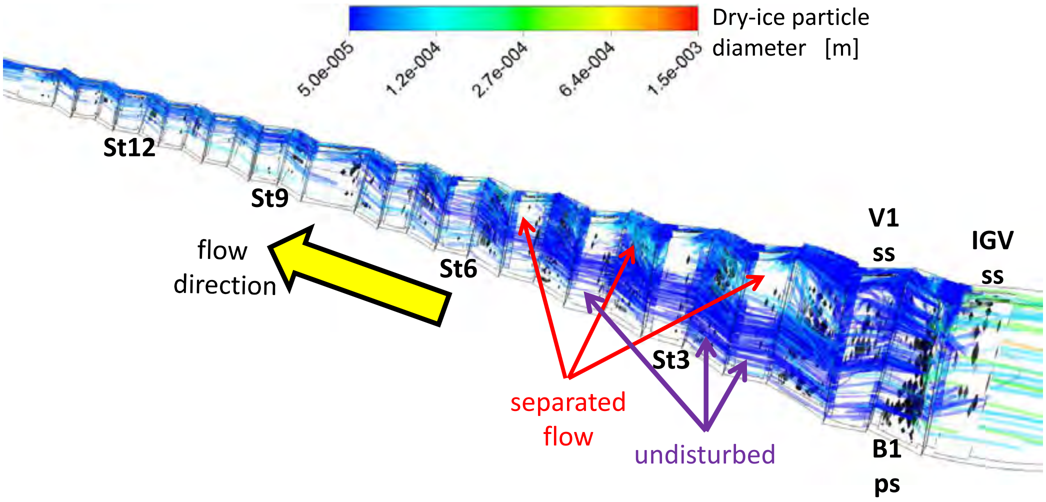

Figure 8.17.: Numerical particle tracks from 1 % process time (only a reduced number is shown): HPC, rotor pressure sides (ps), stator suction sides (ss).

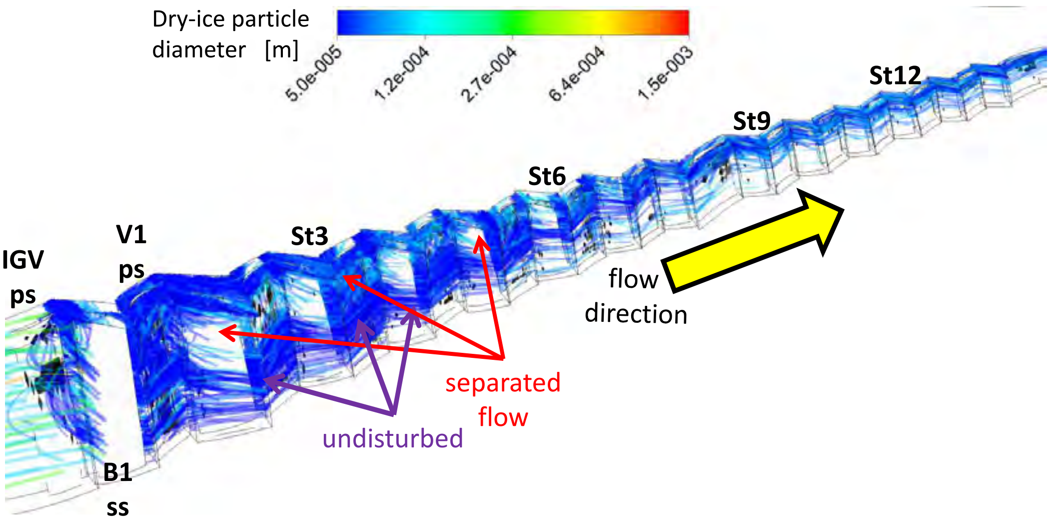

Figure 8.18.: Numerical particle tracks from 1 % process time (only a reduced number is shown): HPC, rotor suction sides (ss), stator pressure sides (ps).

stages of the HPC and the flow is dominated by small particles downstream of the IGVs. Almost no particles hit the suction side of the first blade and this can be attributed to the strong vortex predicted at the inlet of the HPC which is discussed in section 8.2.

The separated outer flow region and the undisturbed inner flow channel at front HPC stages are also recognizable in the particle tracks. There are just a few particles at the suction sides of the blading in the vortex region and the tracks at the corresponding pressure sides are chaotic. In contrast, ordered particle tracks can be seen in the region of the undisturbed flow and the particle tracks tend to concentrate at the outer radius of the engine if these are downstream of the vortex region (i.e. behind stage 6). Before this position these tracks mainly concentrate at the outer radius of the undisturbed flow region.

General findings

Simulation results indicate that some particles pass through the entire compressor since small particles are found to exit the HPC. Mass balances and particle counts show that approximately 5 % of the injected particle mass enter the HPC but the number of the particles is an order of magnitude higher at this position compared to the number of particles injected into the engine. The mean particle size predicted at the inlet into the HPC is only 10 % of the mean particle size injected into the engine.

Furthermore, there is only 0.05 % of the total mass found to exit the HPC in the particle size classes considered. The number of the particles at the exit of the HPC, however, is another order of magnitude higher compared to the injection properties and the mean particle size at the exit of the HPC is approximately 60 % of the particle size at the inlet of the HPC.

Comparison of numerical to experimental particle properties

These computational particle tracking results are compared to experimental data where possible and the experimental data is acquired in HSC experiments at two discrete positions of the HPC (details can be found in section 8.1). The comparison of the results is presented in Fig. 8.19. The left-hand side diagram shows cumulative probability trends for the particle size distributions at the injection position (LPC in), at the inlet of the HPC (HPC in) and at the outlet of the HPC (HPC out) and the right-hand side diagram contains such trends for the particle velocity distributions.

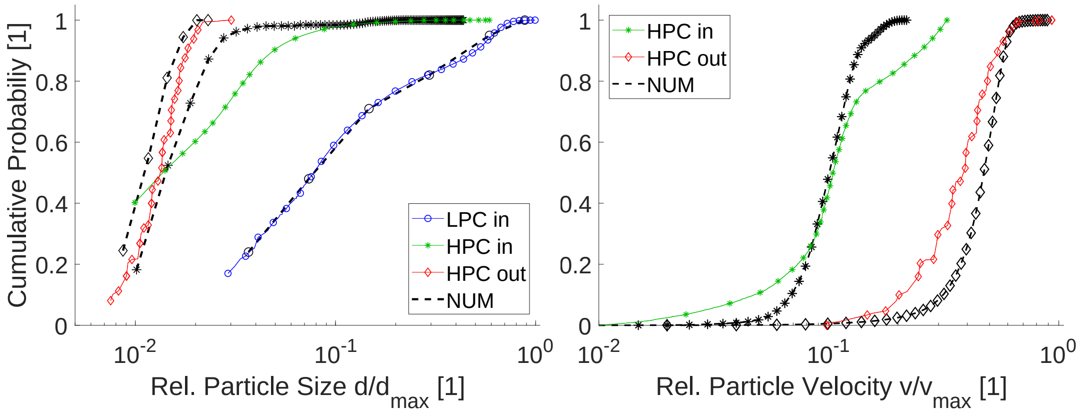

Figure 8.19.: Defouling simulations - local comparison of numerical to experimental data, particle sizes (left) and particle velocity (right).

The experimental trends from the injection position and from the inlet position of the HPC consist of more than 100,000 particles each but these from the outlet of the HPC consist of only approximately 550 because the quality of the recordings from the higher stage was not sufficient to visualize more of the very small and fast particles. These particle classes considered in the post-processing of the numerical results are equal to those from the experiment and the smallest particles considered have a diameter of approximately 40 μm. The experimental data is subdivided into classes at the injection position in preparation of the simulation and the derived distribution, which is used as boundary condition to the particle tracking, is shown in the diagram.

Good overall agreement of the numerical and experimental distributions can be seen for all trends despite the particle sizes at the inlet into the HPC. In the latter case the simulation predicts significantly more smaller particles compared to the experiment. The particle sizes at the outlet of the HPC are slightly underpredicted but the trend is in very good agreement with experimental data.

The deviation of the particle size distributions at the inlet of the HPC can be attributed to factors related to the experimental measurement such as local aggregation of larger particles in the field of view of the HSC and influences of the location of the experimental control volume close to the inner radius of the channel whereas the numerical data is taken from the whole channel.

Furthermore the model uncertainties revealed in section 7.3.1, which require additional investigations into the breakup boundaries of dry-ice and the application of a further random variable, may influence the predicted particle size distribution at this position.

The numerical velocity distributions presented are both in good agreement with the experimental trends. The experimental velocity data from the inlet position into the HPC appears to be bi-modal but this second mode is not predicted to the same extent. A probable cause for this difference could be cross-flowing particles (i.e. induced by collision with the first rotor) which are considered in the experimental trends. This effect may be underpredicted in the simulation due to the limited number of secondary particles considered. The velocities at the outlet of the HPC are slightly overpredicted.

From examination of these graphs it can be concluded that the experimental ranges of particle sizes and velocities are well predicted. A comparison of simulated to experimental mean values is given in Tab. 8.2 and based on these numbers it is concluded that the model predicts the actual behaviour with a reasonable accuracy for the desired defouling simulation. The mean deviations of the variables considered range from 10 % to 23 %.

	HPC in	HPC out
Particle Size	22.41 %	9.71 %
Particle Velocity	14.71 %	21.08 %

Table 8.2.: Overview of mean value deviations of numerical to experimental results for particle variables.

8.3.2 Defouling erosion simulations

In the final step of this work the PTFE defouling erosion predictions in the test engine are discussed and, where possible, compared to experimental data. The upper display in Fig. 8.20 shows the defouled areas on the blading of the LPC for 10 % of the Cyclean process time and the lower display the corresponding results for 100 % of the process time. The pressure sides are largely defouled after 10 % of the cleaning process at both the stator and the rotor blades. However, there is a significant difference in the defouling of the suction sides between these times and there is significantly less defouling visible after 10 % of the process compared to the 100 % results.

Although total cleaning is rapidly achieved for the pressure sides of LPC components, cleaning of suction sides, and particularly the fan suction side, is less effective. This is evident from both experiment and simulation. Based on the above results, it can be concluded that the entire pressure sides and a proportion of the suction sides are cleaned by the main particle flow, whereas total cleaning of suction sides is reliant on deflected particles. Prediction of this cleaning effect therefore requires prediction of secondary particle tracks and particle breakup.

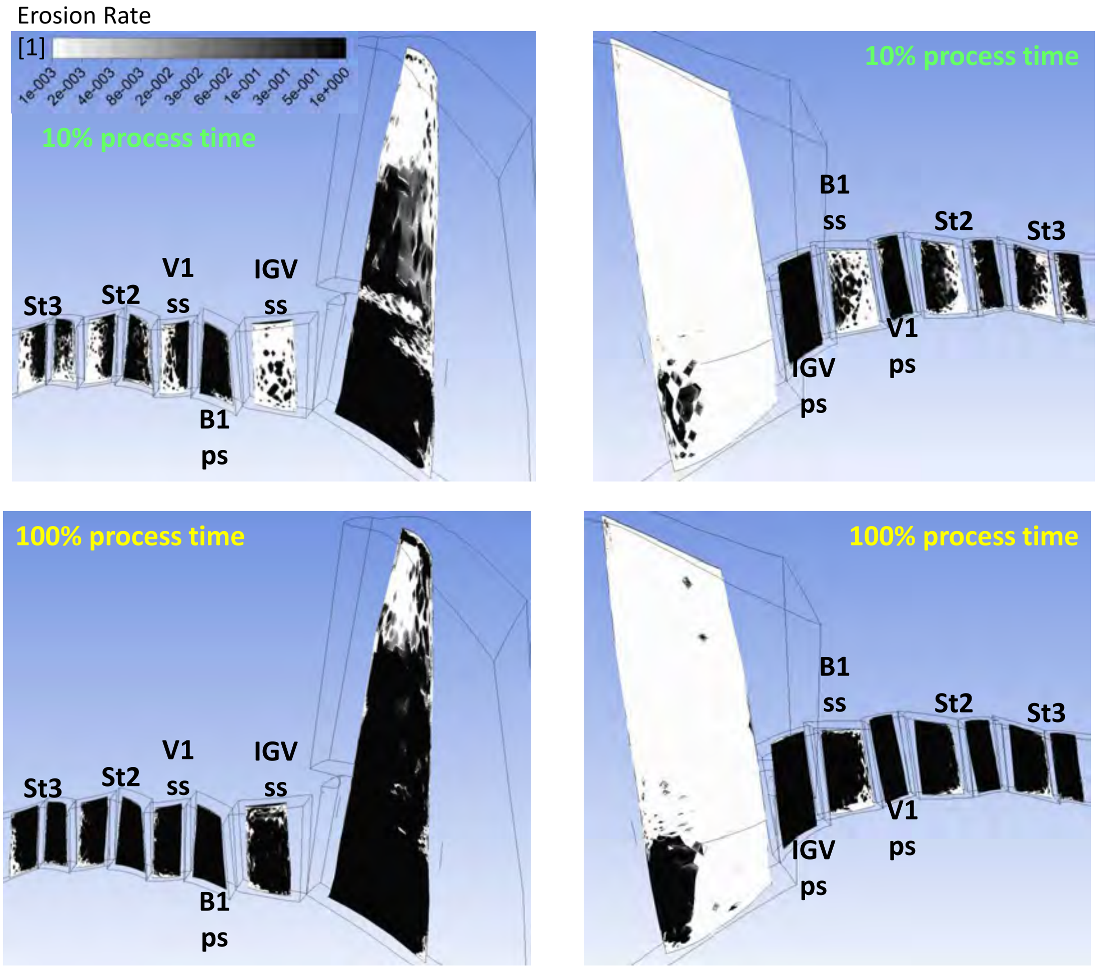

Figure 8.20.: Numerical defouling results: LPC, both sides, 10 % process time (upper display) and 100 % process time (lower display).

The breakup process significantly increases the number of particles in the engine and this significantly changes the particle trajectories thereby increasing the probability of particles impacting suction sides. This flow of secondary particles is less effective in the cleaning process and therefore requires a longer time to achieve cleaning.

Corresponding results from the HPC are displayed in Fig. 8.21 and 8.22 and these are discussed below. The more efficient (i.e. earlier) cleaning of the pressure sides can also be observed in the HPC simulations if the results are compared to these from the LPC. It can also be seen that cleaning of the pressure sides is more effective (i.e. more rapid) where the flow is disordered (i.e. stages 1-6) compared to later stages.

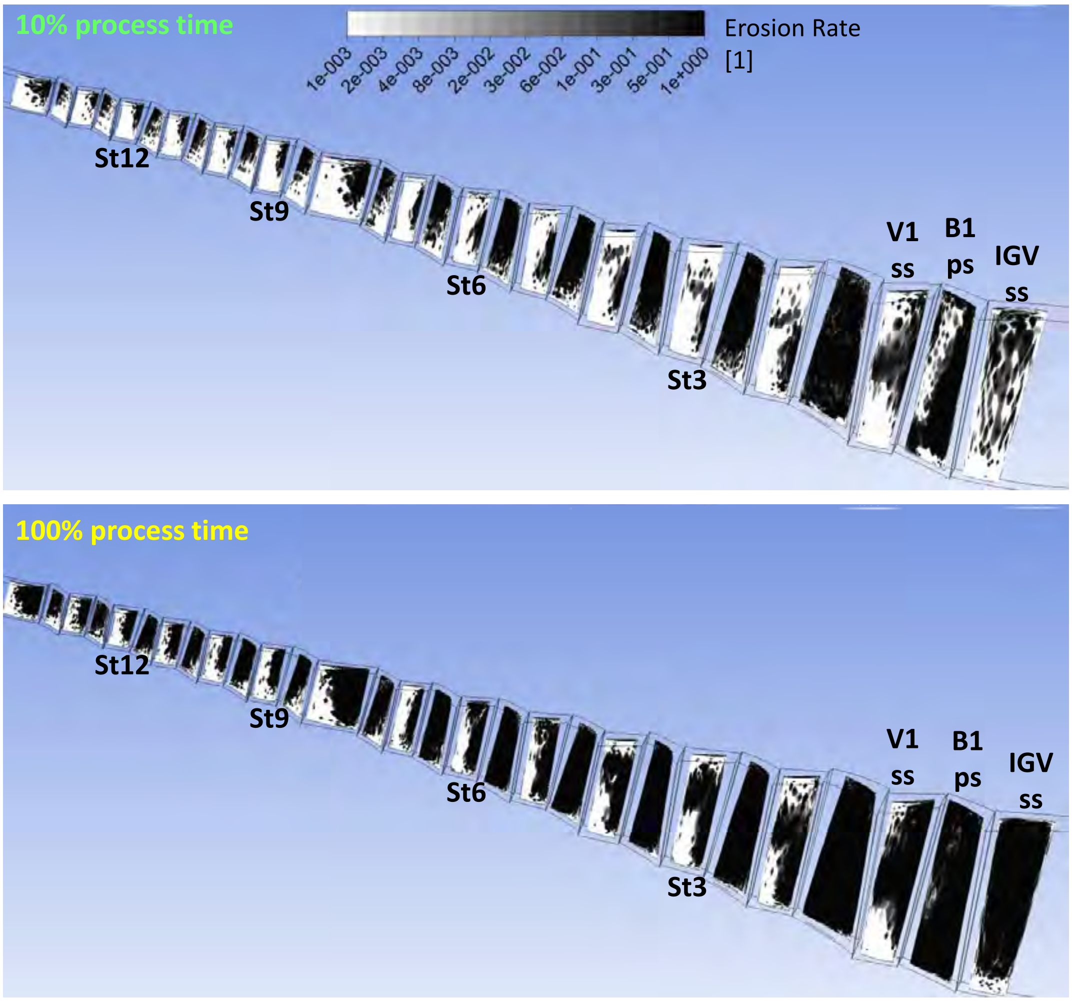

Figure 8.21.: Numerical defouling results: HPC, stator suction sides (ss) and rotor pressure sides (ps), 10 % process time (upper display) and 100 % process time (lower display).

The cleaning of the suction sides is limited to characteristic patterns and approximately 40 % to 60 % of the surfaces. The cleaning pattern at the suction sides of the front stages, where the outer flow is separated, appears to be different from this at the blading of rear stages.

The characteristic defouling pattern of these suction sides of the rotors shifts from inner radii at the front-most stages to the middle of the channel at stages 6 to 8 and then further up to the outer radii at stages 9 and higher. Furthermore, there is additional defouling recognized on both the suction sides of the rotors and of the stators in the separated outer flow region and this can be attributed to the chaotic particle behaviour in this region. No particle tracks are seen to

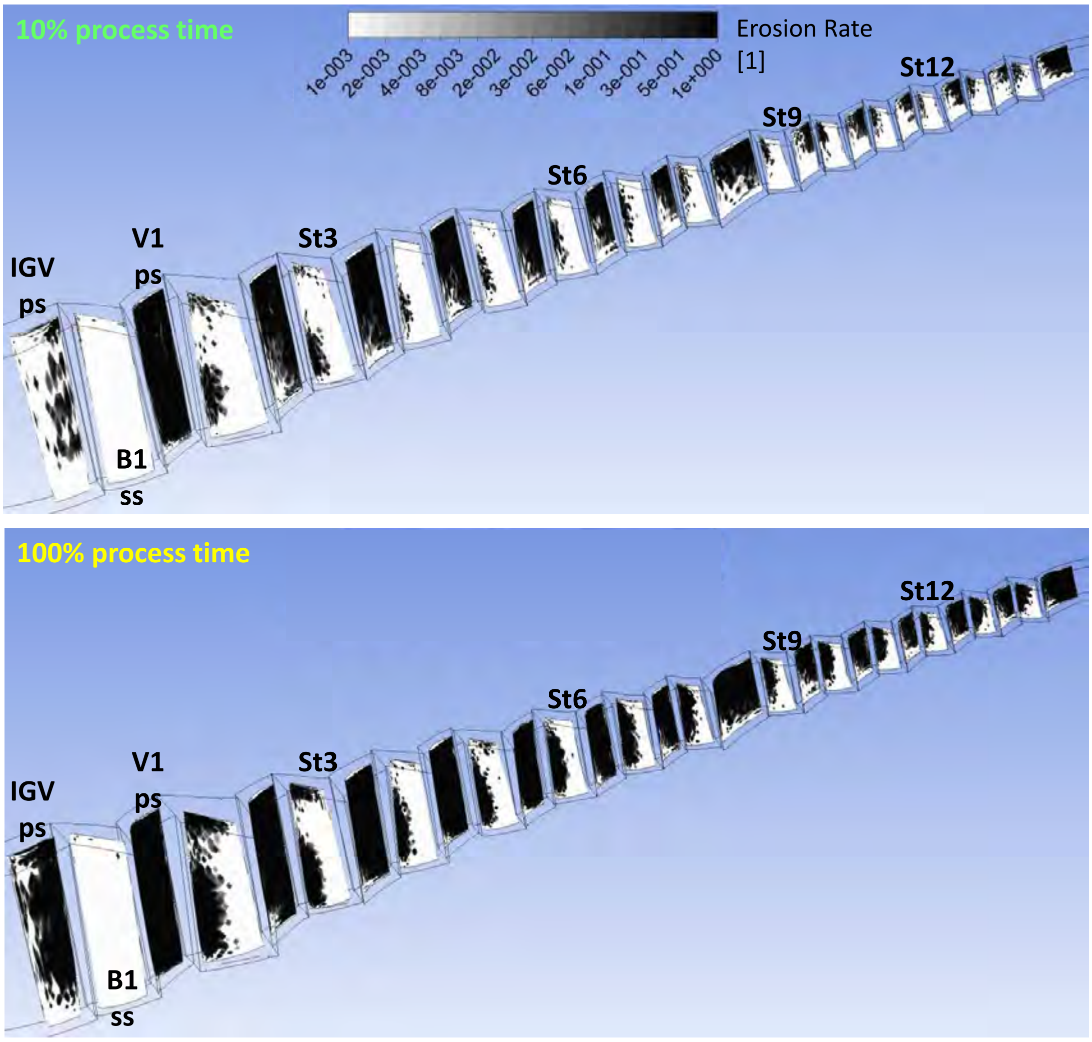

Figure 8.22.: Numerical defouling results: HPC, stator pressure sides and rotor suction sides, 10 % process time (upper display) and 100 % process time (lower display).

impact the suction side of blade 1 because these particles are redirected by the strong flow separation predicted at this position. Hence, there is no defouling visible in the numerical results at this surface.

Qualitative comparison of numerical to experimental results

A qualitative comparison of numerical to experimental results is given in Fig. 8.23 and 8.24. Typical erosion patterns from an extensive experiment are selected and compared to corresponding patterns from the simulation at the stages 3, 6, 9 and 12 at the suction sides. Very good agreement of the

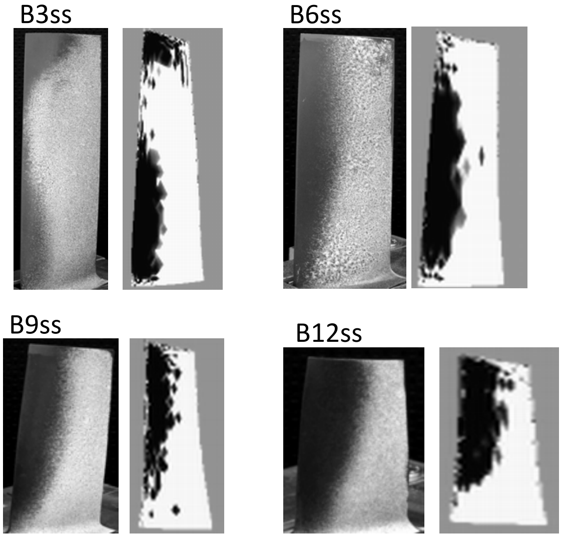

Figure 8.23.: Numerical defouling patterns compared to experimental: HPC, ROTOR suction sides, stages 3, 6, 9 and 12.

cleaning patterns on the rotor can be seen for all stages considered and this is displayed in Fig. 8.23. In particular, those characteristics which are potentially influenced by the separation flow region, such as the divided cleaning area at stage 3 and the shift of the maximum cleaning towards outer radii of the engine for rear stages, are precisely predicted.

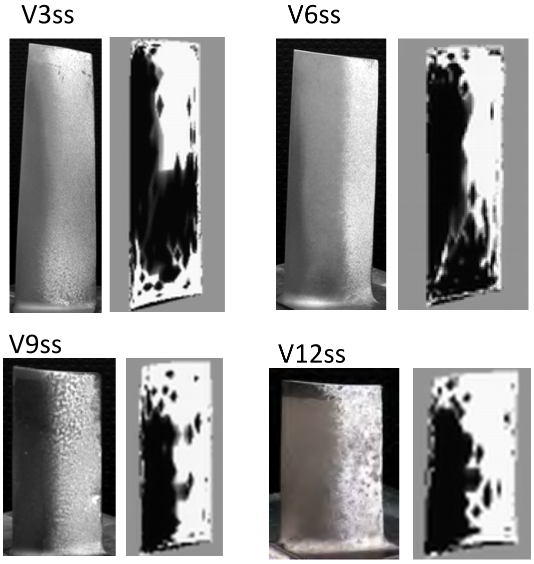

Figure 8.24.: Numerical defouling patterns compared to experimental: HPC, STATOR suction sides, stages 3, 6, 9 and 12.

Figure 8.24 shows the same comparison for the corresponding stator blades. The stator blades shown are taken from the stator region which displays the maximum cleaning effect. The cleaning patterns are generally comparable but the maximum cleaning region at the outer radii of the vanes at front HPC stages is overpredicted by the numerical simulations. It is possible that this is because the simulations overpredict the effect of separated flow on stochastic particle distribution. Nevertheless it can be concluded that the predicted erosion patterns at the rotors are in good agreement and those at the stators are in reasonable agreement with experimental data.

Quantitative comparison of numerical to experimental results

Finally, the simulated defouling values are compared to experimental values and this is shown in Fig. 8.25 and 8.26. Figure 8.25 shows mean value trends for the experiment with the largest sample size and three comparable experiments with the same parameters but lower sample sizes. In the case of the large scale experiment, which is highlighted in the diagram by the thick coloured trend line, a total of 336 rotor blades and 1260 stator blades were investigated. In these additional experiments a total of 70 rotor blades and 75 stator blades were considered.

The left-hand diagram in Fig. 8.25 shows the trends for the pressure sides of the rotor blading and the right-hand side those for the suction sides. The global experimental trends are clearly met by the numerical results. The cleaning prediction is very good at the pressure sides until stage 7. After this stage the numerical defouling data decreases significantly at stage 8 but this significant decrease can be found only in particular experimental data and it starts at rear stages such as 10 and 11.

Prediction of the suction side cleaning is very good in the front part of the engine up to stage 9 and the numerical results show underprediction at rear stages. There is more scatter in the experimental results for the suction sides compared to the pressure sides and there is one experimental dataset which deviates from the others over several stages. Although the completely unaffected

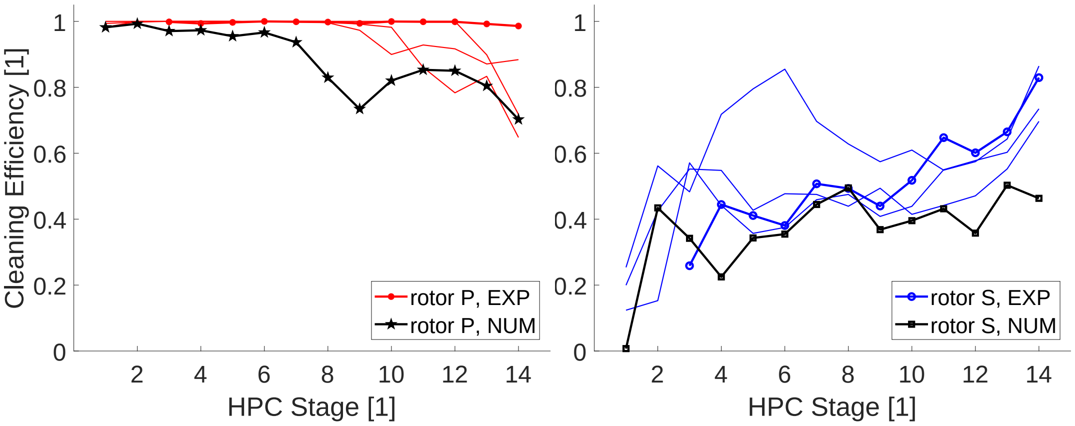

Figure 8.25.: Mean cleaning efficiency of rotor blading: numerical results compared to experimental data, pressure sides (left) and suction sides (right).

fouling on the suction side of the first numerical blade is not confirmed by the experimental data, the defouling predicted here is low compared to that of the remaining stages. The underpredictive character of the numerical results at stages higher than 7 can be attributed to significantly lower numbers of model particles in the simulation compared to the actual situation.

The same comparison is discussed for the stator blading in Fig. 8.26. Only the large scale experiment is considered here because the predictions are only valid for the mean particle path and it was clearly identifiable only with this experiment. The experimentally maximally cleaned stator blades can be compared to corresponding data from the numerical simulation. However, the mean experimental values of the stator cleaning (i.e. the overall result derived from all stator blades expeimentally investigated) are also presented in the diagrams.

The maximum cleaning efficiency of the pressure sides is well predicted and, in addition, the predicted decrease of the values shows reasonable agreement with the experimental data. The comparison of the suction sides in the right-hand diagram shows that the significant differences of the experimental data in the first stages of the compressor are not predicted by the simulation. However, the maximum value predictions are in good agreement with the experimental data at the rear stages of the HPC.

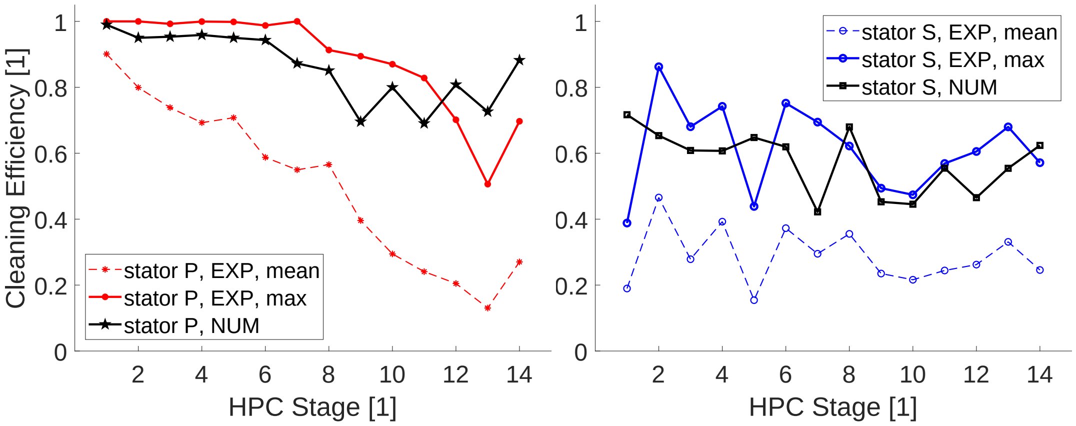

Figure 8.26.: Maximum cleaning efficiency of stator blading (i.e. only representing stator blades being located in the mean particle flow): numerical results compared to experimental data, pressure sides (left) and suction sides (right); NOTE: mean experimental values are also presented (i.e. the overall result derived from all blades investigated) but these results are not predicted by the simulations.

It must be noted that the mean values recognized in the experiment are significantly lower but there was only a single blasting machine considered in the experiment of the cleaning process. The finalized Cyclean process uses four such machines increasing the probability that the actual cleaning efficiency will be closer to the predicted maximum.

Based on the results presented here it can be concluded that the new erosion model has been successfully applied in an engine defouling simulation in conjunction with the new particle breakup model for dry-ice. The defouling values predicted are in good agreement with experimental data. The main cleaning patterns as well as the overall trends of the cleaning process are predicted with a reasonable accuracy with deviations in the range from 11 to 21 % and this is summarized in Tab. 8.3.

In general, the pressure side predictions are closer to the experimental data compared to the suction sides. This may be attributed to the model uncertainty reported in section 7.3.2. It has been revealed that potential improvement to the defouling erosion model presented can be achieved by the consideration of scatter in the defouling functions with an additional random parameter. It was shown that this model uncertainty mainly affects angular impacts and the probability for angular impacts is higher at the suction sides compared to the pressure sides, which may explain the more significant deviations.

	Pressure side	Suction side
Rotor	11.20 %	20.87 %
Stator	11.02 %	18.81 %

Table 8.3.: Overview of mean value deviations of numerical to experimental results for defouling efficiency.

8.3.3 Summary of the application case study

A steady state simulation approach has been presented for air-flow predictions of a dry-cranked aircraft engine and it was successfully compared to experimental data from the compressor to prove its validity for the later defouling simulations. The deviations encountered for the pressure and the velocity field range from 10 % to 23 % and these are acceptable given the computational efficiency achieved with this method and taking into account the unstable nature of this operational mode of the engine (i.e. it is turned at 20 % of the nominal speed of the high pressure shaft).

Based on these air-flow predictions the final PTFE defouling simulations have been carried out using the Ansys CFX implementation of the new particle breakup and defouling erosion models presented in this work. The predictions of particle properties and defouling of the blading have been compared to experimental data and good overall agreement was reported. The deviations encountered in this work range from 10 % to 22 %. They are either explainable via experimental issues such as local effects in the particle tacking or by model uncertainties, such as the hard boundaries applied for the onset of particle breakup and defouling erosion (see section 7.3).

Further experimental and numerical work is necessary to achieve a more detailed insight into an appropriate simulation strategy for these defouling scenarios. Local effects, such as the positioning of the Cyclean injection system in the intake of the engine, possible influences of the air-flow from the injection system upon the particle tracks or the impact of the particles upon the continuous air flow inside the engine etc. remained unconsidered in the approach presented here.

A detailed sensitivity analysis of the calibration procedure for the model parameters of the Ansys CFX implementation of the breakup model is also necessary. However, these additional topics require the handling of very large amounts of data because transient simulations of a larger proportion of the engine (i.e. at least 90° symmetry with consideration of one Cyclean injection system) and more particle tracks, in particular secondary particles, must be considered.

However, it is possible to use the simulation strategy and the models presented in this work to help understand the cleaning process and to carry out numerical parameter studies of the Cyclean system. Possible parameters for such studies range from various types of fouling to system parameters of the cleaning system such as the particle mass flux, size distribution, velocity or injection position and direction.

9 Summary and Outlook

This chapter gives a detailed summary of the work, it highlights its main results and these are discussed in detail and it gives an outlook dealing with the planned future work based on the findings presented here. Each of the research topics addressed in this work is discussed separately and finally in conjunction with each other when discussing the application case study.

9.1 Dry-ice injection system modelling

Summary

An experimental and numerical investigation was presented dealing with solid particle acceleration in a range of nozzle geometries typically used in dry-ice based aircraft defouling applications. The main goal of this part of the study was to advance the state of the art of dry-ice blasting simulations by an all encompassing validation study in which experimental and numerical particle tracks from a wide range of dry-ice blasting nozzles were compared and the predictive capabilities of the numerical toolbox used were quantified.

For this reason a transparent convergent-divergent dry-ice blasting nozzle was presented. It was operated in various flow regimes and experimentally investigated with a HSC. Correlations of particle velocities were derived for a range of POM particles of various sizes accelerated at a range of representative operating pressures. Velocity was found to be a function of particle size and nozzle pressure and decreasing scattering of the velocity was found for increasing nozzle pressure. The correlations presented can be used to validate numerical simulations of dilutely particle laden flows.

Furthermore, a HSC experiment was presented to investigate variously laden dry-ice flows from all types of nozzles considered. A sizing and tracking algorithm was introduced to derive particle size and velocity information from these recordings. Velocity was found to be a function of particle diameters, but only for large dry-ice particles, and of the nozzle/pressure combination applied. For the smaller particle sizes, a large velocity scattering was encountered. A comparison of the POM particle velocities with the velocities of large dry-ice particles for dilutely laden dry-ice flows revealed a good overall agreement of the trends. This agreement could not be confirmed for densely laden dry-ice flows.

The numerical set-up of the nozzle simulations presented was validated against published data for pure air flows and comparable results were achieved. The particle tracks from the transparent nozzle were used to validate the Lagrangian particle tracking implementations of Ansys CFX. It was found that the predictive capabilities of the implemented tools decrease with increasing operating pressure in conjunction with the flow regimes and geometries considered. Best results were achieved with a 2-way coupling formulation and consideration of drag and pressure gradient forces in the particles ODE of motion. A maximum underprediction of approximately 15 % was found for the mean particle velocities at the exit of the nozzle in the case of the highest nozzle pressure considered.

Finally, numerical parameter studies of all the above nozzles were carried out. Comparison of the predicted particle velocities at the exit of the nozzles to these experimentally investigated revealed a good overall agreement for the subsonic and the sonic nozzle but the results for the supersonic nozzle being operated at 8 bar revealed non-satisfactory deviations as high as 35 %. Therefore it was necessary to improve the predictive capabilities of the numerical toolbox for supersonic nozzles and high operating pressures and a new drag-coefficient formulation was developed by means of re-engineered experimental particle tracks from the validation experiments with the transparent nozzle. The following discussion of this data lead to a Mach-number related drag-coefficient formulation which improved the predictions of the particle tracks. The deviations could be decreased from approximately 20 % to 10 % for the dilutely laden flows and from 35 % to 23 % for the densely laden flow.

This part of the study advanced the state of the art of dry-ice blasting simulations by a number of validation experiments and by the assessment of the predictive capabilities of the Ansys CFX toolbox for such simulations as was intended. The experimental particle tracks from the transparent nozzle and the particle size and velocity information from all types of dry-ice blasting nozzles considered can be used for further validation studies.

The study presented is the first one to deal with all possible types of flow regimes in dry-ice blasting (i.e. subsonic, sonic and supersonic flows) and it presents numerical and experimental data for each of these cases. The statistical significance of the experimental data was assured by large databases consisting of as much as 40,000 single dry-ice particle information for each parameter. The accuracy of the particle tracking was found to be +/- 5.0 % and this of the particle sizing was found to be +/- 6.5 %. These uncertainties could be attributed to inhomogeneous illumination of the objects in the recordings and transitional inaccuracies resulting from the threshold valuing and centroid matching approaches taken.

The Lagrangian particle tracking toolbox was found to be applicable for dry-ice blasting simulations of subsonic and sonic flow regimes in conjunction with all particle loadings considered, i.e. all deviations encountered were lower than 10 %. However, the deviations encountered in the case of the supersonic nozzle being operated at high nozzle-pressure were unsatisfactory and this was attributed to the drag-coefficient formulation applied. An experimental procedure delivered a modified drag-coefficient formulation and this significantly decreased the deviations. Based on this it was concluded that the drag-coefficient for supersonic dry-ice blasting nozzles is a function of the flow Mach number rather than of the particle Reynolds number. Additional work is necessary to prove and generalize these findings (see below).

A number of additional findings were reported and these advance the knowledge of dry-ice blasting systems. In this context it was shown that there is a significant agreement between dry-ice velocities from dilutely-laden flows and single POM particle velocities in a range of particle sizes. It is therefore suggested to use POM particles for experimental engineering and development approaches before using dry-ice, which clearly facilitates the experimental procedure and the post-processing.

Furthermore it was shown that the particle velocities are dependent on the particle size for large dry-ice particles. This dependency vanishes for small particles and it was shown that the large velocity scattering of these small particles can be captured by presenting the results in CDF diagrams. The scattering was attributed to the particle breakup process and possible particle-particle interaction inside the nozzles. It could not be precisely predicted with the methods discussed here because they do not account for particle breakup and particle-particle interaction phenomena inside the nozzles. However, it was shown that the predictions are correct for the maximum particle velocities encountered. The simulations can be improved by usage of the newly developed particle breakup model and additional consideration of particle-particle interaction models.

Outlook

Future work is necessary to investigate more deeply the physical situations described in section 4.5, where the improvement of the particle tracking tools was presented. The correlation which was found for the drag coefficient in convergent-divergent supersonic nozzles must be confirmed for a wide range of nozzle geometries, pressure settings and particle sizes to evaluate if it is widely usable.

Additional experimental and numerical work is desirable to investigate flow details such as pressure-field modifications, vortex-shedding and shock-cell as well as expansion- and compression wave structures and their interaction with particles for various situations where particles are located in convergent and divergent sections of supersonic nozzles and where these may modify the flow pattern. After this, findings could be generalized to situations where particles are moving throughout the nozzles. Future work on these simulations can also encompass further development of numerical methods such as turbulence model modifications due to particle presence in the flow or further development of the immersed boundary method (see for example [211]) to account for volumetric particles in such simulations.

The generalization of the findings and the confirmation of their validity for other nozzle geometries and pressure settings as well as a deeper investigation into the particle size dependency is currently being investigated in another research project by the author. Furthermore, the interaction between the particles and the continuous flow field is experimentally investigated in an aeroacoustic test-rig. A possible coupling of the particle breakup model with the nozzle simulations is also investigated in this context.

It is planned to publish the main outcomes from these current studies at the International Conference of Multiphase Flow 2019 in Rio de Janeiro, Brazil.

9.2 Particle breakup modelling

Summary

A new particle breakup model for dry-ice particles has been theoretically and experimentally derived from a basic mass and energy balance, and it is believed to be the first of its type for Lagrangian dry-ice particles.

A sensitivity analysis was presented which was related to the application case of commercial aircraft compressor defouling and it was used to simplify the basic model assumptions. A theoretical approach was presented in the context of this analysis to assess the internal bond energy of dry-ice.

Furthermore, a basic experiment was introduced utilizing two HSCs to produce the statistical database for later computations with the above particle breakup model. With this, an extensive database of dry-ice particle breakup scenarios was generated, comprising the investigation of a total of 4,200 single dry-ice particle impacts. The data and the final model show a significant dependence of secondary particle number, size and velocity, principally on primary particle velocity and size, and to a lesser extent on impact angle and negligible, if any, dependence was found of all variables on the target temperature.

The above findings indicated a change in the breakup mechanism at low impact velocities and, therefore, an additional experimental study was conducted to describe the onset of breakup as a function of particle impact diameter and velocity. The final formulation of this boundary function was adapted from literature and compared to experimental data for water ice particles.

Computational implementation of the model was found to reproduce the experimental findings. Some variations were present in both the Matlab and Ansys CFX implementations, but overall the model was able to reproduce the number of secondary particles to within +/- 3 % and mean diameters and velocities to +/- 2 %.

Discussion

The state of the art of dry-ice blasting simulations has been successfully advanced by the introduction of a dry-ice particle breakup model for Lagrangian particle tracking, which did not exist before this work. The model presented is implicitly mass and energy conservative and it was shown that is also satisfies momentum conservation. It can therefore be used for simple particle breakup predictions, in which only the secondary particle properties are of interest, but it can also be used for advanced simulation purposes in terms of the balancing of mass, momentum and energy.

The structure of the model advances the state of the art of general particle breakup modelling in Lagrangian particle tracking because it can be used in large scale applications and, if the statistical database is modified, it can be used for different materials. In advance of comparable existing models, such as the Eulerian example presented by CHAPELLE et al. [32, 33, 34], the model presented here allows more detailed single particle based evaluation of flow conditions in engineering applications because single particles can be tracked and balanced.

It was shown that the model was able to reproduce the number of secondary particles to within +/- 3 % and that of the mean diameters and the mean velocities to within +/- 2 % compared to the underpinning experimental data. These deviations could be attributed to the rounding and conservation enforcement procedures applied in the computations. The advantage of a fully conservative formulation of the model eliminates the disadvantage of these deviations and these were therefore decided to be acceptable. The particle tracking accuracy of the experimental data was +/- 5.0 % and this of the particle sizing was +/- 6.5 % (for details see above).

The model is underpinned with an experimental database and the basic experiment is comparable to what was reported by VARGAS et al. [200] in 2015 for water ice particles in one of the latest experimental investigations of water ice breakup. The experiment presented here was developed independently but in parallel to the above publication (see ZITZMANN [IV]) and a similar approach is taken. The database developed comprises 4,200 single particle impacts whereas comparable experiments dealing with water ice breakup such as these by VARGAS et al. [200] or HAUK [78] comprise significantly lower numbers of specimens. In addition, no such experimental work dealing with dry-ice is known to date an therefore it advances the state of the art in the field of dry-ice investigations.

It was found using a sensitivity analysis that sublimation plays an important role in the overall energy balance, which confirms the findings reported by HABERLAND [72], REDEKER [156] and KRIEG [103]. The latter represent the state of the art in this field of research. However, as an additional advance in this field, it was shown that breakup energy plays an important role at low impact velocities and that erosion energy is not negligible in general terms if a defouling process is considered.

In addition to the above findings the study incorporated the derivation of the material's Young's modulus and applied Hertzian contact theory in a molecular scale bond model to account for the dry-ice particle breakup energy. The theoretical Young's modulus was compared to experimental values reported elsewhere for dry-ice and to such for water-ice and good overall agreement was found. The procedure presented can therefore be concluded to be valid for the derivation of Young's moduli for ice particles. The values presented for the Young's modulus and for the internal bond energy of dry-ice are an advance of the state of the art of dry-ice investigations.

Finally the onset of breakup of the dry-ice particles was described by an experimentally underpinned function which was originally reported for water ice particles by HAUK [78]. It was found that this method applies also for dry-ice particles and that the onset of breakup can be described in a similar way for both materials. The dry-ice experiments revealed a mixed breakup zone where particle breakup occurs in a number of cases only. This mixed breakup-zone was not reported for water ice. The discussion of the onset of breakup of dry-ice particles is also an advance of the state of the art in the field of dry-ice research.

Outlook

The particle breakup model presented can be enhanced by conducting additional experiments to improve certain theoretical assumptions. Therefore, an additional validation study on the energy balance should be applied and the model performance could be compared to single particle simulations using for example DEM or SPH methods. In particular the sublimation energy and the breakup energy proportions should be validated, because these are based on fully theoretical approaches at the moment.

Furthermore, a more precise database could further enhance the model capabilities in general. One such specification could be achieved for example by conducting high precision experiments on the dust-phase. The database of the model could be changed to account for another material such as water ice and it can be used, for example, in the wide context of hail-strike investigations which are a current safety topic in aeronautical research (see for example HAUK et al. [77, 78]).

It is not planned to further improve the particle breakup model at the moment but the main outcomes from this study are planned to be published in the International Journal of Multiphase Flow 2018. The model will be used in dry-ice blasting investigations by Lufthansa Technik and Hochschule Darmstadt and attempts are planned to use the model in the context of hail-strike investigation projects in future.

9.3 Defouling erosion modelling

Summary

It was intended to advance the state of the art of dry-ice based defouling simulations by the introduction of a new defouling erosion model in this part of the study. Such a model was successfully presented and the theoretical formulation of this model was based on a number of assumptions derived from an extensive literature review. The model applies an energy based formulation which was underpinned with an experimental database. It accounts for the area defouled, for the energy consumed during the defouling process and for the shape of the indentation produced by single particle impacts upon variously fouled walls.

Four types of fouling materials typically found in commercial aircraft engine compressors (i.e. original fouling) and those typically used in defouling experiments at the test-rig (i.e. indicator coating) were considered. This selection was based on a number of investigations of fouling materials in cooperation with Lufthansa Technik. The set-up used to derive the database of the particle breakup model (see above) was slightly modified to conduct the experiments for the erosion model. It was used to determine energy dissipation of particles made from non-disintegrative reference material impacting variously fouled targets and to measure the shape and size of indentations from single particle impacts upon these targets.

A total of 2,000 single particles has been investigated and representative results from these experiments show good agreement between the defouling energy assessment and the defouled areas measured. It was found that the defouling process is a function of particle velocity, density and diameter. This defouling process was correlated with logarithmic functions for all cases considered (i.e.

all particle and fouling material combinations). It was shown that the coefficient of determination of these correlations decreases with increasing natural scatter (i.e. artificial vs. original fouling and reference vs. dry-ice particles). However, a significant correlation strength was reported for all except one case. Comparable defouling behaviour was reported for both of the artificial fouling materials and for both of the original fouling materials investigated.

The theoretical model formulation and the statistical database were developed into a computational Matlab model and into an Ansys CFX implementation of this model and a range of computed results was discussed. These results highlight the actual defouling capabilities of dry-ice and the relation between the defouling energy and the areas defouled. It was shown that the impact energy consumed for defouling is highly dependent on the particle impact velocity and diameter. This proportion of energy is assumed to be negligible in the total energy balance of the impacting particles underpinning the particle breakup model even if there are ranges of variables in which the defouling energy proportion can be as high as 30 % of the particle impact energy.

Finally it was shown in a brief verification study that the model predicts the underpinning database with most significant deviations of 0.72 % in the case of defouling energy.

Discussion

The presentation of the new defouling erosion model for dry-ice based defouling of amorphous and heterogeneous fouling materials, which are typically found in axial aircraft compressors, represents an advance in the state of the art of defouling erosion modelling. No such model was available for these material pairings before this publication.

A large experimental database with defouling data was presented and a statistical analysis of the significance of the derived correlations was given. It was shown that the defouling action is, in all cases considered, a logarithmic function of the particle impact velocity and a linear function of its diameter and these findings represent an advance in the state of the art of defouling investigations.

The experimental procedure presented and the structure of the new model allow a straightforward extension of the material pairings considered in the model and hence the model can be straightforwardly extended to various application cases. Furthermore, the model can be linked with the particle breakup model because its formulation is energy based. An overall energy assessment of impacting dry-ice particles is possible by means of this link and this is an advance in the state of the art of particle flow simulations.

These most significant deviations of 0.72 % in the case of defouling energy were attributed to rounding procedures and addition of uncertainties of indentation size predictions and these are decided to be negligible. The particle tracking accuracy was +/- 5.0 % and the accuracy of the particle and indentation sizing procedure was +/- 6.5 % (for details see above).

Numerous publications were reviewed and some of the main findings have been linked together in the framework of the model development. These following publications represent the state of the art of various fields of research. The idea of erosion-related energy assessment has been presented by various authors [90, 91, 92, 101, 102, 145, 147, 148] and the "dynamic indentation testing" (DI) experiment presented was designed based on general ideas adapted from [91, 92, 184, 194]. Furthermore, non-disintegrating reference material (POM) was used to determine dissipation energy of defouling action and this idea is based on findings from [18, 42, 63, 64]. The dissipation energy values were assumed to be specific to the fouling material and valid for indentations of various particle materials and this assumption was based on findings such as reported for example in [88, 89, 101, 102] for crystalline materials. The link of all these findings to a new model assumption represents an advance in the state of the art in defouling erosion modelling. The basic model idea can be used in experimental and numerical based future work.

Outlook

The defouling erosion model presented can be enhanced by additional evaluation of the scattering of the experimental defouling data. This can be done based on the statistical database presented here and it is planned to be done by the author in the near future. If additional experiments should be conducted to the overall energy balance of dry-ice particles impacting solid walls, fouled surfaces can be considered and in this case the influence of the defouling energy upon the total energy balance must be investigated, which is possible with the model presented.

Furthermore, four typical coatings which are relevant to commercial aircraft defouling processes were investigated in this study. It is possible to enlarge this statistical database to numerous coating and particle materials in the future using the basic experiment presented. Some additional experiments with dry-ice and water-ice particles in conjunction with various additional fouling materials are currently investigated at Hochschule Darmstadt by the author. It is also planned to enlarge the model to further defouling effects such as thermal and chemical and this is currently addressed in another research project at Hochschule Darmstadt in collaboration with Lufthansa Technik.

A publication of the improved model (i.e. improvement by additional evaluation of the scattering) in conjunction with an extensive experimental database is planned in the Wear Journal in 2018 or 2019 (i.e. depending on the progress of the improvements and the enlargement of the database).

9.4 Validation case study

Summary

A validation case study for the new particle breakup and erosion models was presented and for this reason a new wind-tunnel experiment was designed in which a dilutely laden particle flow situation was observed by means of HSCs. Initially, pure air flow simulations as well as single particle tracking simulations with POM particles were compared to experiments. The mean deviations between predicted and experimental data range from 3 % to 12 % for the flow pressure profiles and from 1 % to 16 % for the flow velocity profiles. Furthermore, these deviations for the particle impact and rebound characteristics range from 1 % to 5 % for the velocities and from 5 % to 12 % for the impact angle.

The actual validation of the particle breakup model was described in detail in section 7.3 and four different parameter settings have been considered in the experiment. The mean deviations achieved were 27 % for the number of secondary particles and 10 % for the secondary particle diameters. Furthermore, the significant experimental scattering of the variables was reproduced all cases considered.

The validation of the defouling erosion model was also presented in section 7.3 and the model was validated using two artificial fouling materials and the four above parameter settings. The results indicate that the predictive capabilities decrease with increasing impact angle (i.e. a change of the impact direction from normal to tangential measured to the target surface). The mean deviations range from 13 % to 44 % and the significant experimental scattering was reproduced well in 50 % of the cases considered.

Discussion

The mean deviations encountered in the particle breakup validation were decided to be acceptable given the large scattering of the experimental and numerical data, the deviations caused by the particle tracking simulations (i.e. 1 % to 5 % for the velocities and 5 % to 12 % for the impact angle) in conjunction with their impact upon the particle breakup statistics underpinning the model and the post-processing accuracy of the model database and of the experimental validation data (i.e. +/- 6.5 % for particle sizes and +/- 5.0 % for particle velocities).

There was a large scattering of the variables encountered in the particle breakup validation study and this scattering of the secondary particle variables was attributed to the stochastic process of dry-ice breakup. It is mainly influenced by the original structure of the particles and this structure is mainly influenced by the production process, the transportation of the particles and by their maturity. Even if the production variables were constant throughout the whole project and the maturity of the dry-ice particles used was 1 to 3 days in all cases these influences cannot be completely ruled out. However, the scattering is a key characteristic of the real breakup process; it was also observed in the basic experiment and it was shown that the model reproduces the scattering range to a satisfactory extent.

In total, the mean particle diameter predictions (i.e. mean deviations of +/- 10 %) are more precise than these of partially comparable models such as this reported by CHAPELLE et al. [32] (i.e. +/- 15 %) which is an advance in particle breakup modelling for engineering purposes. The mean numbers of secondary particles are less precisely predicted compared to the diameters (i.e. mean deviations of +/- 27 %) and this was attributed, additionally to the material structure alterations discussed above, to various computational conservation and rounding procedures applied in the model.

However, it was shown that the predicted number of secondary particles was highly influenced by the impact velocity and angle and that small deviations in these predicted impact characteristics can cause significant deviations in the predicted number of secondary particles, in particular in the range of impact velocities and angles where the mixed breakup mode is indicated (for details see above). These most significant deviations of the predicted numbers of secondary particles were found in those variable ranges.

A possible improvement of the model was addressed based on these findings and additional investigations were proposed to elaborate the boundaries of the mixed breakup zone of dry-ice and to introduce additional random variables to account for the stochastic nature of this zone. Such an additional study would further improve the scattering predictions and it would mainly improve the predicted number of secondary particles.

Furthermore, the results from the validation study showed that the general defouling behaviour, which indicates the differences between the fouling materials considered, was well predicted. These major differences were better predicted for steep target angles compared to those for the low target angles. However, also the predictions for low target angles were found to be within the range of experimental scatter.

This scatter was predicted to a satisfactory extent for PTFE but the model underpredicts the scatter for SALT defouling. In the case of SALT almost no scatter was identified in the predictions and at low nominal air velocity and low target angle the model failed to predict defouling. The particle breakup model was shown to be valid in conjunction with the defouling erosion model because secondary particle indentations were correctly predicted. These secondary particle indentations were found to cause the scatter in case of PTFE defouling.

A possible improvement to the model was identified based on the above findings and it can be achieved by consideration of experimental scatter (i.e. scatter measured in the basic experiment) in the defouling functions. This may improve the range of the scatter predicted as well as the prediction of the onset of erosion, which is a solid bound at the moment and causes the large deviations encountered for low target angles, in particular in the case of the SALT layers.

In total, the mean values were predicted with an accuracy of 15 % for steep target angles and 40 % for low target angles. These deviations are caused by the particle tracking uncertainties (i.e. 1 % to 5 % for the velocities and 5 % to 12 % for the impact angle) in conjunction with their impact upon the statistics underpinning both the particle breakup and the defouling erosion model and the post-processing accuracy of the model database and of the experimental validation data (i.e. +/- 6.5 % for particle and indentation sizes and +/- 5.0 % for particle velocities).

The uncertainties are increased in case of the low impact angles by the range of impact velocities and angles where the mixed breakup mode and the onset of erosion are indicated (i.e. where steep gradients are encountered in the model functions). These most significant deviations of the predicted defouling were found in those variable ranges and the uncertainty modulation is comparable to what was reported above when discussing the deviations of the predicted numbers of secondary particles.

Outlook

The validation experiment can be used for additional validation studies with artificially or originally fouled targets as well as for validation purposes in case of database extensions of the model. It would be useful to carry out more measurements to enlarge the existing validation database presented to add statistical significance to the findings and to extend the range of the validation parameters (i.e. the particle impact characteristics for both models).

The results from the validation study presented will be considered for improvement of the defouling erosion model and in the publications planned for both models (see above).

9.5 Application case study

Summary

The final application of the new models in an aircraft compressor defouling simulation was presented and it was intended to use all above findings in this final part of the study to advance the state of the art of application based defouling simulations.

The numerical set-up presented consists of a stream-channel approximation of the engine and it applies rotational periodicity and coarse meshing. However, good agreement between the predicted and the experimental flow field was achieved and mean pressure and velocity values were predicted with mean accuracies in the range from 7 % to 22 %. Although the velocity profiles at various stages do not exactly match the measured data, the global trends were recognizable.

The injection of the particles was simplified in the simulation and a method was presented to use measured particle injection properties in a valid boundary condition for steady state simulations.

Comparison of the predicted particle tracks to these measured revealed a predictive capability of the breakup model in conjunction with the simulation set-up presented which ranges from 10 % to 22 % for the particle sizes and velocities at discrete positions. The global trends of the particle size and velocity distributions were accurately predicted by the simulations except that the predicted trend of the particle size distribution at the inlet into the HPC did not match the experiment.

The final defouling simulations were compared to a range of defouling experiments in which artificial PTFE fouling was used. A global surface comparison of the defouled blading showed good agreement between the predictions and the experiment. There was a region identified in the front stages of the HPC where some mismatches were encountered. Furthermore, mean deviations between the defouling predictions and the experiments were evaluated and these range from 11 % to 21 %.

Discussion

The new models were successfully used in the final application case study and the engine defouling predictions presented are believed to be the first of their type. However, the main findings from the injection system investigations were not used for the final simulations presented here, because a periodical stream channel symmetry of the engine was applied which did not permit modelling of the localization of the injection due to the position of the injection nozzles.

To account for this at least a 90° symmetry approach must be taken; this approach was part of the research project and such simulations were conducted by Lufthansa Technik. The models were applied successfully in these simulations. However, only a very short period of time (i.e. 70 ms) and only the intake and the LPC section of the test engine could be simulated due to memory issues during the solution process and during the post-processing of the simulations. No comparison of these predictions to experimental data could be made.

The flow field simulations presented here were compared to experimental results and the mean deviations within 7 % to 22 % for the flow field predictions are satisfactory given the symmetry assumption, the coarse meshing, the steady-state set-up and the mixing-plane approach taken to link subsequent airfoil passages to each other. Furthermore the potentially unstable operational state of the engine must be taken into account (i.e. the engine is dry-cranked during the cleaning process and it turns at 20 % of the nominal rotational speed) and measurement uncertainties were quantified with 4.0 % for pressure and 2.5 % for velocities. In particular the numerical set-up can be improved to achieve higher accuracies in future work.

The deviations of the predicted particle sizes and tracks range from 10 % to 22 % and this was mainly attributed to the deviations in the prediction of the flow field (as discussed above), to the measurement uncertainties in the particle sizing (i.e. 6.5 %) and tracking (i.e. 5.0 %) and to possible local effects in the measurements in the engine such as aggregation of larger particles in the field of view of the HSC and influences of the location of the experimental control volume close to the inner radius of the channel.

A significant discrepancy in the predicted particle sizes and tracks was discovered at the inlet into the HPC and this discrepancy was assumed to be also dependent on the mixed breakup zone formulation in the actual breakup model implementation (i.e. a hard lower boundary is applied) and it can be improved by the additional work addressed above.

In total, the simulation results represent a significant advance in the state of the art of particle tracking simulations in dry-cranked engines. This work is the first one which systematically compares experimental and numerical flow-field and particle tracking data and which clearly predicts dry-ice particle breakup in an engine cleaning application (in comparison to GILJOHANN et al. [61]) with an quantified and satisfactory precision for engineering purposes.

The application of the defouling erosion model and the comparison of the predictions to the experimental data revealed that the cleaning patterns are generally comparable. The maximum cleaning region at the outer radii of the vanes at front HPC stages is overpredicted by the numerical simulations. It is possible that this is because the simulations overpredict the effect of separated flow on stochastic particle distribution. In contrast, those patterns which were potentially influenced by the separated flow, such as locally divided cleaning areas and local shifts of the maximum cleaning towards outer radii of the engine at rear stages, were precisely predicted.

In general, the pressure side predictions are closer to the experimental data compared to the suction sides. This may be attributed to the model uncertainty reported above, which revealed that potential improvement to the defouling predictions can be achieved by the consideration of scattering in the defouling functions. It was shown that this model uncertainty mainly affects angular impacts and the probability for angular impacts is higher at the suction sides compared to the pressure sides, which may explain the more significant deviations. Furthermore, there is more scattering in the experimental results for the suction sides compared to the pressure sides.

The completely unaffected fouling on the suction side of the first numerical blade is not confirmed by the experimental data and this was attributed to an imprecise prediction of the flow field in this place and to the lack of scattering values in the model functions. The underpredictive character of the numerical results at stages higher than 7 was attributed to significantly lower numbers of model particles in the simulation compared to the actual situation. The main cleaning patterns as well as the overall trends of the cleaning process are predicted with a reasonable accuracy for engineering purposes with deviations in the range from 11 % to 21 %

Based on these results it can be concluded that the new erosion model has been successfully applied for the first time in an engine defouling simulation in conjunction with the new particle breakup model for dry-ice. The defouling values predicted are in good agreement with experimental data (i.e. for engineering purposes) and this result is a clear advance of the state of the art in engine defouling simulations and investigations in general (compare for example to MUND and PILLIDIS [130], ENGDAR et al. [52] or GILJOHANN et al. [61]).

Outlook

Some of the goals of this part of the study, such as the application of the main findings from the injection system investigations in the engine cleaning simulations, the simulation of a larger proportion of the engine (i.e. 90° symmetry) and the application of original fouling material could not be achieved due to a number of implementation issues with the Ansys CFX model. It was therefore decided to investigate the predictions of PTFE (i.e. indicator coating) defouling in detail with the first stable simulation set-up and to compare these results to corresponding experimental data, where possible.

Finally it was successfully shown that it is possible to predict the actual dry-ice based cleaning process of commercial aircraft engines with the models and simulation set-ups presented, even if a number of assumptions must be made to achieve an efficient procedure.

Future work should encompass the definition of a calibration procedure of the novel particle breakup model and a sensitivity analysis of the model parameters of the CFX implementation. Furthermore, an extensive parameter study of dry-ice based cleaning of various engine types and fouling materials can be carried out by means of the findings presented here. Further simulations of the test engine are planned by the author at Hochschule Darmstadt using original fouling. These should also be compared to experiments where possible.

Furthermore it is planned to investigate a 90° symmetry volume of the test-engine in conjunction with the development of big-data methods to overcome the memory exceptions during the simulation and in the post-processing and to be finally able to handle this large sized models and to evaluate with it achieved results. This research project is planned to be a cooperation between Dublin Institute of Technology and Hochschule Darmstadt and it is planned to start it in 2018.

The outcomes presented in this work and the additional simulations with original fouling addressed above are planned to be published in a paper at the ASME Turbo Expo 2019 in Phoenix, Arizona, USA.

Bibliography

[1] Shannon Ackert. Engine maintenance concepts for financiers. *Aircraft Monitor*, 2:1–43, 2011.

[2] K. G. Adamopoulos and H. J. Petropakis. Simulation of distribution of discrete inert particles in two phase supersonic mixing. *Journal of Food Engineering*, 42:59–66, 1999.

[3] Ronald J. Adrian. Particle-imaging techniques for experimental fluid mechanics. *Annual Review of Fluid Mechanics*, 23:261–204, 1991.

[4] R. Agbadede, P. Pilidis, U.L. Igie, and I. Allison. Experimental and theoretical investigation of the influence of liquid droplet size on effectiveness of online compressor cleaning for industrial gas turbines. *Journal of the Energy Institute*, 88:414–424, 2015.

[5] Nicola Aldi, Mirko Morini, Michele Pinellia, Pier Ruggero Spina, Alessio Sumana, and Mauro Venturinia. Numerical analysis of the effects of surface roughness localization on the performance of an axial compressor stage. *Proceedings of the 68th Conference of the Italian Thermal Machines Engineering Association, Bologna, Italy*, 45:1057–1066, 2013.

[6] Sergej Aman, Juergen Tomas, and Haim Kalman. Breakage probabilityofirregularlyshapedparticles. *Chemical Engineering Science*, 65:1503–1512, 2010.

[7] E.W. Andrews and K.-S. Kim. Threshold conditions for dynamic fragmentation of ceramic particles. *Mechanics of Materials*, 29:161–180, 1998.

[8] E.W. Andrews and K.-S. Kim. Threshold conditions for dynamic fragmentation of glass particles. *Mechanics of Materials*, 31:689–703, 1999.

[9] AnsysINC. Ansys cfx-solver theory guide. Southpointe, Canonsburg, PA, 2013.

[10] S. Antonyuk, M. Khanal, J. Tomas, S. Heinrich, and L. Moerl. Impact breakage of spherical granules: Experimental study and dem simulation. *Chemical Engineering and Processing*, 45:838 – 856, 2006.

[11] S. Antonyuk, S. Palis, and S. Heinrich. Breakage behaviour of agglomerates and crystals by static loading and impact. *Powder Technology*, 206: 88–98, 2011.

[12] Sergiy Antonyuk, Stefan Heinrich, Juergen Tomas, Niels G. Deen, Maureen S. van Buijtenen, and J. A. M. Kuipers. Energy absorption during compression and impact of dry elastic-plastic spherical granules. *Granular Matter*, 12:15–47, 2010.

[13] M. F. Ashby and D. R. H. Jones. *Engineering Materials I*. Butterworth Heinemann, 1996.

[14] S. C. Back, G. V. Hobson, S. J. Song, and K. T. Millsaps. Effects of reynolds number and surface roughness magnitude and location on compressor cascade performance. *Journal of Turbomachinery*, 134:1–6, 2012.

[15] A. B. Bailey and J. Hiatt. Free-flight measurements of sphere drag at subsonic, transonic supersonic, and hyper sonic speeds for continuum, transition, and near-free-molecular flow conditions. Technical report, Arnold Engineering Development Center, Air Force Station, Tennessee, 1971.

[16] A. B. Bailey and J. Hiatt. Sphere drag coefficients for a broad range of mach and reynolds numbers. *AIAA Journal*, 10:1436–1440, 1972.

[17] K. Bammert and G. U. Woelk. The influence of the blading surface roughness on the aerodynamic behavior and characteristic of an axial compressor. *Journal of Engineering for Gas Turbines and Power*, 102:283–287, 1980.

[18] Guy Barnocky and Robert H. Davis. Elastohydrodynamic collision and rebound of spheres: experimental verification. *Physics of Fluids*, 31:1324 – 1329, 1988.

[19] N. A. Barton. Erosion in elbows in hydrocarbon production systems: Review document. Technical report, TUEV Netherlands for Health and Safety Executive, 2003. Research Report 115.

[20] A. B. Basset. *Treatise on hydrodynamics*. Deighton, Bell and Co., Cambridge, 1888.

[21] Y. Ben-Ami, A. Uzi, and A. Levy. Modelling the particles impingement angle to produce maximum erosion. *Powder Technology*, 301:1032–1043, 2016.

[22] J. Boussinesq. *Theorie analytique de la chaleur (in French)*. L'Ecole Polytechnique, Paris, 1903.

[23] Michael R. Brady, Samuel G. Rabenb, and Pavlos P. Vlachos. Methods for digital particle image sizing (dpis): Comparisons and improvements. *Flow Measurement and Instrumentation*, 20:207–219, 2009.

[24] Willy J. G. Braeunling. *Aeroengines (in German)*. Springer Vieweg, 2009.

[25] José Roberto Tavares Branco, Robert Gansert, Sanjay Sampath, Christopher C. Berndt, and Herbert Herman. Solid particle erosion of plasma sprayed ceramic coatings. *Materials Research*, 7:147–153, 2004.

[26] I.N. Bronstein, K.A. Semendyayev, G. Musiol, and H. Muehlig. *Handbook of Mathematics*. Verlag Harri Deutsch, 2005.

[27] Klaus Brun, Marybeth Nored, and Rainer Kurz. Analysis of solid particle surface impact behavior in turbomachines to assess blade erosion and fouling. *Proceedings of the 41st Turbomachinery Symposium, Houston, USA*, 1:1–12, 2012.

[28] Klaus Brun, Terrence A. Grimley, William C. Foiles, and Rainer Kurz. Experimental evaluation of the effectiveness of online water-washing in gas turbine compressors. *Proceedings of the 42nd Turbomachinery Symposium, Houston, USA*, 1:1–18, 2013.

[29] William D. Callister. *Fundamentals of Materials Science and Engineering*. John Wiley & Sons, Inc., 2001.

[30] H. A. Carmona, F. K. Wittel, F. Kun, and H. J. Herrmann. Fragmentation processes in impact of spheres. *Physical Review Letters*, 93:1–11, 2004.

[31] F. Cernuschi, C. Guardamagna, S. Capelli, L. Lorenzoni, D. E. Mack, and A. Moscatelli. Solid particle erosion of standard and advanced thermal barrier coatings. *Wear*, 348 - 349:43 – 51, 2016.

[32] Pierre Chapelle, Hadi Abou-chakra, Nicholas Christakis, Ian Bridle, Mayur Patel, J. Baxter, Ugur Tuezuen, and Mark Cross. Numerical predictions of particle degradation in industrial-scale pneumatic conveyors. *Powder Technology*, 143-144:321–330, 2004.

[33] Pierre Chapelle, Hadi Abou-chakra, Nicholas Christakis, Mayur Patel, Azlina Abu-nahar, Ugur Tuezuen, and Mark Cross. Computational model for prediction of particle degradation during dilute-phase pneumatic conveying: the use of a laboratory-scale degradation tester for the determination of degradation propensity. *Advanced Powder Technology*, 15: 13–29, 2004.

[34] Pierre Chapelle, Nicholas Christakis, Hadi Abou-chakra, Ian Bridle, M. S. A. Bradley, Mayur Patel, and Mark Cross. Computational model for prediction of particle degradation during dilute-phase pneumatic conveying: modeling of dilute-phase pneumatic conveying. *Advanced Powder Technology*, 15:31–49, 2004.

[35] A. C. Charters and R. N. Thomas. The aerodynamic performance of small spheres from subsonic to high supersonic velocities. *Journal of the Aeronautical Sciences*, 12:469–476, 1945.

[36] Michael K. Cheezum, William F. Walker, and William H. Guilford. Quantitative comparison of algorithms for tracking single fluorescent particles. *Biophysical Journal*, 81:2378–2388, 2001.

[37] Q. Chen and D. Y. Li. Computer simulation of solid particle erosion. *Wear*, 254:203 – 210, 2003.

[38] Shao-Wen Chen, Hui Shi, Chen Zhang, Song-Tao Wang, and Zhong-Qi Wang. Study on numerical simulation of fouling in compressor rotor. *International Journal of Turbo Jet-Engines*, 29:179–188, 2012.

[39] X. Chen, B. M. McLaury, and S. A. Shirzai. Numerical and experimental investigation of the relative erosion severity between plugged tees and

elbows in dilute gas/solid two-phase flow. *Wear*, 261:715 – 729, 2006.

[40] C. T. Crowe. Drag coefficient of particles in a rocket nozzle. *AIAA Journal*, 5:1021–1022, 1967.

[41] J.H. Currier, E.M. Schulson, and W.F.St. Lawrence. A study on the tensile strength of ice as a function of grain size. Technical report, US Army Corps of Engineers: Cold Regions Research & Engineering Laboratory, 1983.

[42] Robert H. Davis, Dean A. Rager, and Brian T. Good. Elastohydrodynamic rebound of spheres from coated surfaces. *Journal of Fluid Mechanics*, 468:107 – 119, 2002.

[43] John A. Dean. *Langes Handbook of Chemistry*. R. R. Donnelley & Sons Company, 1999.

[44] I. S. Diakunchak. Performance deterioration in industrial gas turbines. *International Gas Turbine and Aeroengine Congress and Exposition, Orlando,USA*, 4:1–8, 1991.

[45] B. Djurovic, E. Jean, M. Papini, P. Tangestanian, and J. K. Spelt. Coating removal from fiber-composites and aluminum using starch media blasting. *Wear*, 224:22 – 37, 1999.

[46] Shujuan Dong, Bo Song, Bernard Hansz, Hanlin Liao, and Christian Coddet. Improvement of adhesion of plasma-sprayed al2o3 coatings by using dry-ice blasting. *Materials Letters*, 66:289–291, 2012.

[47] Shujuan Dong, Bo Song, Bernard Hansz, Hanlin Liao, and Christian Coddet. Improvement in the microstructure and property of plasma sprayed metallic, alloy and ceramic coatings by pre-/during-treatment of dry-ice blasting. *Surface & Coatings Technology*, 220:199–203, 2013.

[48] S.J. Dong, B. Song, B. Hansz, H. L. Liao, and C. Coddet. Modelling of dry ice blasting and its application in thermal spray. *Materials Research Innovations*, 16:61–66, 2012.

[49] A. El-Zahaby, M. Hamed, Z. Omara, and A. Eldesoukey. Study of the configuration and performance of air-air ejectors based on cfd simulation. *Journal of Aeronautics and Aerospace Engineering*, 6:1–9, 2017.

[50] Said Elghobashi. On predicting particle-laden turbulent flows. *Applied Scientific Research*, 52:309–329, 1994.

[51] Said Elghobashi. An updated classification map of particle-laden turbulent flows. *Proceedings of the IUTAM Symposium on Computational Multiphase Flow*, 1:3–10, 2006.

[52] Ulf Engdar, Magnus Genrup, Raik C. Orbay, and Jens Klingmann. Investigation of the two-phase flow field of the gtx100 compressor inlet during off-line washing. *Proceedings of GT2004: ASME Turbo Expo, Vienna, Austria*, 1:1–10, 2004.

[53] Bernd Epple, Reinhard Leithner, Wladimir Linzer, and Heimo Walter. *Numerical Simulation of Power Plants and Firing Systems*. Springer, 2012.

[54] J.M. Fan, H.Z. Li, J. Wang, and C.Y. Wang. A study of the flow characteristics in micro-abrasive jets. *Experimental Thermal and Fluid Science*, 35: 1097–1106, 2011.

[55] F. Filser and L.J. Gauckler. *Material Science I*. ETH Zuerich, 2007.

[56] Iain Finnie. Erosion of surfaces by solic particles. *Wear*, 3:87 – 103, 1960.

[57] H. Foell. Electronical scriptum: Material sciences i and ii, 2005. URL `http://www.tf.uni-kiel.de/matwis/amat/mw1_ge/`.

[58] Felix Foerster and Bernhard Weigand. Characterization of a heterodyne lita setup for simultaneous flow velocity and speed of sound measurements. *19th AIAA International Space Planes and Hypersonic Systems and Technologies Conference,* , Atlanta:pp. 1–11, 2014.

[59] Robert W. Foster. Carbon dioxide (dry-ice) blasting. *Good Painting Practice: SSPC Painting Manual*, 1:161–167, 2005.

[60] GeneralElectric. Cf6-50 em gek 50481. H.W.51, Hamburg, 2014.

[61] S. Giljohann, K. Bräutigam, S. Kuhn, S. Annasiri, and G. Russ. Investigations into the on-wing cleaning of commercial jet engines with co2 dry-ice blasting. *Deutscher Luft- und Raumfahrtkongress*, 1:1–9, 2012.

[62] S. Godbout, L. Chenard, and A. Marquis. Instantaneous young's modulus of ice from liquid manure. *Canadian Agricultural Engineering*, 42:95–100, 2000.

[63] P. Gondret, E. Hallouin, M. Lance, and L. Petit. Experiments on the motion of a solid sphere toward a wall: from viscous dissipation to elastohydrodynamic bouncing. *Physics of Fluids*, 11:2803 – 2805, 1999.

[64] P. Gondret, M. Lance, and L. Petit. Bouncing motion of spherical particles in fluids. *PHYSICS OF FLUIDS*, 14:643 – 652, 2002.

[65] G. Gouesbet and A. Berlemont. Eulerian and lagrangian approaches for predicting the behaviour of discrete particles in turbulent flows. *Progress in Energy and Combustion Science*, 25:133–159, 1999.

[66] G. Grant and W. Tabakoff. Erosion prediction in turbomachinery resulting from environmental solid particles. *Journal of Aircraft*, 12:471 – 478, 1975.

[67] G. Grant and W. Tabakoff. Erosion prediction in turbomachinery resulting from environmental solid particles. *Journal of Aircraft*, 12:471 – 478, 1975.

[68] Ch. Gruener. *Coupling of the Single-Particle- and the Two-Continua-Approach for the Simulation of Gas-Solid Multiphase Flows (in German)*. PhD thesis, University Dortmund, Faculty of Biological and Chemical Engineering, 2004.

[69] Pierrick Guegan, Ramzi Othman, Daniel Lebreton, Franck Pasco, Philippe Villedieu, Jacques Meyssonnier, and Sylvie Wintenberger. Experimental investigation of the kinematics of post-impact ice fragments. *International Journal of Impact Engineering*, 38:786–795, 2011.

[70] Pierrick Guegan, Ramzi Othman, Daniel Lebreton, Franck Pasco, Philippe Villedieu, Jacques Meyssonnier, and Sylvie Wintenberger. Critical impact velocity for ice fragmentation. *Journal of Mechanical Engineering Science*, 226:1–11, 2012.

[71] N. Guel-Oezcan-Taskin, Gustavo Padron, and Adam Voelkel. Effect of particle type on the mechanisms of break up of nanoscale particle clusters. *Chemical Engineering Research and Design*, 87:468–473, 2009.

[72] J. Haberland. *Reinigen und Entschichten mit Trockeneisstrahlen - Grundlegende Untersuchungen des CO2-Strahlwekzeuges und der Verfahrensweise (in german)*. PhD thesis, University Bremen, 1999.

[73] G. Hagemann, M. Frey, and W. Koschel. Appearance of restricted shock separation in rocket nozzles. *Journal of Propulsion and Power*, 18:577–587, 2002.

[74] Ali Hassanpour, Joseph Antony, and Mojtaba Ghadiri. Influence of interface energy of primary particles on the deformation and breakage behaviour of agglomerates sheared in a powder bed. *Chemical Engineering Science*, 63:5593–5599, 2008.

[75] A. Hatzes, F. Bridges, and D. Lin. Collisional properties of ice spheres at low impact velocities. *Monthly Notices of the Royal Astronomical Societ*, 231:1091–1115, 1988.

[76] G. L. Haub and W. E. Hauhe. Field evaluation of on-line compressor cleaning in heavy duty industrial gas turbines. *The Gas Turbine and Aeroengine Congress and Exposition*, 90-GT-107:1–12, 1990.

[77] T. Hauk, E. Bonaccurso, I. V. Roisman, and C. Tropea. Ice crystal impact onto a dry solid wall: Particle fragmentation. *Proceedings of the Royal Society A*, 471:11–25, 2015.

[78] Tobias Hauk. *Investigation of the Impact and Melting Process of Ice Particles*. PhD thesis, Technical University Darmstadt, 2016.

[79] Annika Hell, Eduard Rosenko, Bernhard Weigand, and Stefan Schlamp. Experimental and numerical study of axisymmetric supersonic mixing free jets. *16th AIAA/DLR/DGLR International Space Planes and Hypersonic Systems and Technologies*, , Bremen:pp. 1–11, 2009.

[80] Annika Hell, Eduard Rosenko, Bernhard Weigand, and Stefan Schlamp. Study of axisymmetric subsonic and supersonic free jets. *3rd European*

Conference for Aeronautics and Space Sciences (ECASS), , Versailles:pp. 1–10, 2009.

[81] C. B. Henderson. Drag coefficients of spheres in continuum and rarefied flows. *AIAA Journal*, 14:707–708, 1976.

[82] Frank Hering, Michael Merle, and Dietmar Wierzimok. A robust technique for tracking particles over long image sequences. *Proceedings of ISPRS Intercommission Workshop: From Pixels to Sequences*, 30:1–5, 1995.

[83] Michiya Higa, Masahiko Arakawa, and Norikazu Maeno. Measurements of restitution coefficients of ice at low temperatures. *Planetary Space Science*, 44:917–925, 1996.

[84] Michiya Higa, Masahiko Arakawa, and Norikazu Maeno. Size dependence of restitution coefficients of ice in relation to collision strength. *Icarus*, 133:310–320, 1998.

[85] Kai Hiltunen, Ari Jaesberg, Sirpa Kallio, Hannu Karema, Markku Kataja, Antti Koponen, Mikko Manninen, and Veikko Taivassalo. *Multiphase Flow Dynamics: Theory and Numerics*. VTT PUBLICATIONS, Helsinki, 2009.

[86] A. J. Hodges. The drag coefficient of very high velocity spheres. *Journal of the Aeronautical Sciences*, 24:755–758, 1957.

[87] R. LeB. Hooke and M. Mellor. Mechanical properties of polycrystalline ice: an assessment of current knowledge and priorities for research. *Cold Regions Science and Technology*, 3:263–275, 1980.

[88] Irina Hussainova and Klaus-Peter Schade. Correlation between solid particle erosion of cermets and particle impact dynamics. *Tribology International*, 41:323 – 330, 2008.

[89] Irina Hussainova, Klaus-Peter Schade, and Sergei Tisler. Dynamic coefficients in impact mechanics. *Proceedings of Estonian Academic and Scientific Engineering*, 12:26 – 39, 2006.

[90] I. M. Hutchings and R. E. Winter. The erosion of ductile metals by spherical particles. *Journal of Applied Physics*, 8:8 – 17, 1975.

[91] I. M. Hutchings, R. E. Winter, and J. E. Field. Solid particle erosion of metals: the removal of surface material by spherical projectiles. *Proceedings of the Royal Society of London. Series A, Mathematical and Physical Sciences*, 348:379 – 392, 1976.

[92] I.M. Hutchings. Further studies of the oblique impact of a hard sphere against a ductile solid. *International Journal of Mechanical Sciences*, 23: 639 – 646, 1981.

[93] Kolumban Hutter. *Fluiddynamics and Thermodynamics - An Introduction (in German)*. Springer Verlag, 2003.

[94] K. L. Johnson. *Contact Mechanics*. Cambridge University Press, 1985.

[95] Seung Chai Jung, Donguk Suh, and Woong Sup Yoon. Molecular dynamics simulation on theenergy exchanges and adhesion probability of a nano-sized particle colliding with a weakly attractive static surface. *Journal of Aerosol Science*, 41:745–759, 2010.

[96] K.D. Kafui and C. Thornton. Numerical simulations of impact breakage of a spherical crystalline agglomerate. *Powder Technology*, 109:113–132, 2000.

[97] E. D. Kane. Sphere drag data at supersonic speeds and low reynolds numbers. *Journal of the Aeronautical Sciences*, 18:259–270, 1951.

[98] B. Karpuschewski, T. Emmer, K. Schmidt, and M. Petzel. Cryogenic wet-ice blasting - process conditions and possibilities. *CIRP Annals - Manufacturing Technology*, 62:319–322, 2013.

[99] Jae Hyung Kim, Hyung Goun Joob, and Kang Yong Lee. Simulation of solid particle erosion in wc-ni coated wall using cfd. *Journal of Materials Processing Technology*, 224:240 – 245, 2015.

[100] Michael Kleiber. *Process Engineering: Addressing the Gap between Studies and Chemical Engineering*. De Gruyter, 2008.

[101] I. Kleis and I. Hussainova. Investigation of particle - wall impact process. *Wear*, 233 - 235:168 – 173, 1999.

[102] Ilmar Kleis and Priit Kulu. *Solid Particle Erosion*. Springer, 2008.

[103] M. C. Krieg. *Analyse der Effekte beim Trockeneisstrahlen (in german)*. PhD thesis, Technical University Berlin, 2008.

[104] Rainer Kurz and Klaus Brun. Degradation in gas turbine systems. *International Gas Turbine & Aeroengine Congress & Exhibition, Munich, Germany*, 1:59–65, 2000.

[105] Rainer Kurz and Klaus Brun. Fouling mechanisms in axial compressors. *Journal of Engineering for Gas Turbines and Power*, 134:1–9, 2012.

[106] Santiago Laín and Martin Sommerfeld. Numerical calculation of pneumatic conveying in horizontal channels and pipes: Detailed analysis of conveying behaviour. *International Journal of Multiphase Flow*, 39:105–120, 2012.

[107] B. E. Launder and D. B. Spalding. The numerical computation of turbulent flows. *Computer Methods in Applied Mechanics and Engineering*, 3: 269 – 289, 1974.

[108] D. Y. Li, K. Elalem, M. J. Anderson, and S. Chiovelli. A microscale dynamical model for wear simulation. *Wear*, 225-229:380 – 386, 1999.

[109] Ming-Zheng Li, Wei-Wei Liu, Xiao-Chuan Qing, Yue Yu, Li-Hong Liu, Zi-Jue Tang, Hai-Jiang Wang, Ya-Zhou Dong, and Hong-Chao Zhang. Feasibility study of a new approach to removal of paint coatings in remanufacturing. *Journal of Materials Processing Technology*, 234:102 – 112, 2016.

[110] Yi-Hung Liu, Graham Calvert, Colin Hare, Mojtaba Ghadiri, and Shuji Matsusaka. Size measurement of dry ice particles produced from liquid carbon dioxide. *Journal of Aerosol Science*, 48:1–9, 2012.

[111] Ellen K. Longmire and John K. Eaton. Structure of a particle-laden round jet. *Journal of Fluid Mechanics*, 236:217–257, 1992.

[112] Lufthansa-Technik-AG. Homepage called in april 2017, April 2017. URL `https://www.lufthansa-technik.com/`.

[113] Homer T. Mantis. Review of the properties of snow and ice. Technical report, University of Minnesota, USA, 1951.

[114] Javier Martín-Aragón and Manuel Valdés. A method to determine the economic cost of fouling of gas turbine compressors. *Applied Thermal Engineering*, pages 1–6, 2013.

[115] M. R. Maxey and J. J. Riley. Equation of motion for a small rigid sphere in a nonuniform flow. *Physics of Fluids*, 26:883–889, 1983.

[116] C. B. Meher-Homji. Compressor and hot section fouling in gas tunbines - causes and effects. *Proceedings from the 9th Annual Industrial Energy Technology Conference, Houston, USA*, 1:261–269, 1987.

[117] C. B. Meher-Homji and A. Bromley. Gas turbine axial compressor fouling and washing. *Proceedings of tnhe 33rd turbomachinery symposium*, 1: 163–192, 2004.

[118] Cyrus B. Meher-Homji, Mustapha A. Chaker, and Hatim M. Motiwala. Gas turbine performance deterioration. *Proceedings of the 30th turbomachinery symposium, College Station, USA*, 1:139–175, 2001.

[119] Malcolm Mellor and David M. Cole. Deformation and failure of ice under constant stress or constant strain-rate. *Cold Regions Science and Technology*, 5:201–219, 1982.

[120] F. R. Menter. Improved two equation k-o turbulence models for aerodynamic flows. *NASA TM*, 103975:1–31, 1992.

[121] F. R. Menter. Zonal two equation k-o turbulence models for aerodynamic flows. *24th Fluid Dynamics Conference American Institute of Aeronautics and Astronautics, Orlando, Florida*, pages 1–21, 1993.

[122] F. R. Menter. Two-equation eddy-viscosity turbulence models for engineering applications. *AIAA-Journal*, 32:1598–1605, 1994.

[123] Matthew J. Metzger and Benjamin J. Glasser. Numerical investigation of the breakage of bonded agglomerates during impact. *Powder Technology*, 217:304–314, 2012.

[124] H. Miaosheng, Q. Lizi, and L. Yu. Numerical investigation of flow separation behavior in an over-expanded annular conical aerospike nozzle. *Chinese Journal of Aeronautics*, 28:983–1002, 2015.

[125] B.K. Mishra and C. Thornton. Impact breakage of particle agglomerates. *International Journal of Mineral Processing*, 61:225–239, 2001.

[126] R. Moreno-Atanasio and M. Ghadiri. Mechanistic analysis and computer simulation of impact breakage of agglomerates: Effect of surface energy. *Chemical Engineering Science*, 61:2476–2481, 2006.

[127] Mirko Morini, Michele Pinelli, Pier Ruggero Spina, and Mauro Venturini. Computational fluid dynamics simulation of fouling on axial compressor stages. *Journal of Engineering for Gas Turbines and Power*, 132:1–10, 2010.

[128] Mirko Morini, Michele Pinelli, Pier Ruggero Spina, and Mauro Venturini. Numerical analysis of the effects of nonuniform surface roughness on compressor stage performance. *Journal of Engineering for Gas Turbines and Power*, 133:1–8, 2011.

[129] F. A. Morrison. Data correlation for drag coefficients of spheres, 2016.

[130] F. C. Mund and P. Pilidis. Online compressor washing: a numerical survey of influencing parameters. *Proceedings of the Institution of Mechanical Engineers - Journal of Power and Energy*, 213:13–23, 2005.

[131] Friederike C. Mund and Pericles Pilidis. Gas turbine compressor washing: Historical developments, trends and main design parameters for online systems. *Journal of Engineering for Gas Turbines and Power*, 128:344–353, 2006.

[132] Muhammad Naeem. Impacts of low-pressure (lp) compressors deterioration upon an aero-engines high-pressure (hp) turbine blades life. *The Aeronautical Journal*, 110:227–238, 2006.

[133] Muhammad Naeem. Impacts of low-pressure (lp) compressors fouling of a turbofan upon operational-effectiveness of a military aircraft. *Applied Energy*, 85:243–270, 2008.

[134] Muhammad Naeem. Impacts of low-pressure (lp) compressors deterioration of a turbofan engine upon fuel-usage of a military aircraft. *The Aeronautical Journal*, 112:33–45, 2008.

[135] T. Nagata, T. Nonomurai, S. Takahashi, Y. Mizuno, and K. Fukuda. Direct numerical simulation of flow around a rotating sphere at high mach and low reynolds number condition for supersonic gas-particle flow analysis. *Proceedings of the 9th International Conference on Multiphase Flow, Firenze, Italy*, pages 1–6, 2016.

[136] Y. I. Oka, H. Olmogi, T. Hosokawa, and M. Matsumura. The impact angle dependence of erosion damage caused by solid particle impact. *Wear*, 203-204:573–579, 1997.

[137] Y. I. Oka, K. Okamura, and T. Yoshida. Practical estimation of erosion damage caused by solid particle impact, part 1: Effects of impact parameters on a predictive equation. *Wear*, 259:95 – 101, 2005.

[138] Y. I. Oka, K. Okamura, and T. Yoshida. Practical estimation of erosion damage caused by solid particle impact, part 2: Mechanical properties of materials directly associated with erosion damage. *Wear*, 259:102 – 109, 2005.

[139] Jos Oosting, Klaas Boonstra, Annemarie de Haan, Dick van der Vecht, Jean-Pierre Stalder, and Urs Eicher. On line compressor washing on large frame 9-fa gas turbines erosion on r0 compressor blade leading edge field performance with a novel on line wash system. *Proceedings of GT2007: ASME Turbo Expo, Montreal, Canada*, 1:1–10, 2007.

[140] P. J. ORourke and A. A. Amsden. The tab method for numerical calculations of spray droplet breakup, 1987.

[141] C. W. Oseen. *Hydrodynamik (in German)*. Akademische Verlagsgesellschaft mbH, Leipzig, 1927.

[142] N. Otsu. A threshold selection method from gray-level histograms. *IEEE Transactions on Systems, Man and Cybernetics*, 9:62–66, 1979.

[143] H. Pan and P. M. Render. Impact characteristics of hailstones simulating ingestion by turbofan aeroengines. *JOURNAL OF PROPULSION AND POWER*, 12:457–462, 1996.

[144] N. R. Panchapakesan and J. L. Lumley. Turbulence measurements in axisymmetric jets of air and helium. part 1. air jet. *Journal of Fluid Mechanics*, 246:197–223, 1993.

[145] M. Papini and J .K. Spelt. Organic coating removal by particle impact. *Wear*, 213:185 – 199, 1997.

[146] M. Papini and J. K. Spelt. The plowing erosion of organic coatings by spherical particles. *Wear*, 222:38 – 48, 1998.

[147] M. Papini and J. K. Spelt. Indentation-induced buckling of organic coatings part i: theory and analysis. *International Journal of Mechanical Sciences*, 40:1043–1059, 1998.

[148] M. Papini and J. K. Spelt. Indentation-induced buckling of organic coatings part ii: measurements with impacting particles. *International Journal of Mechanical Sciences*, 40:1061–1068, 1998.

[149] G. J. Parker and P. Lee. Studies of the deposition of sub-micron particles on turbine blades. *Proceedings of the Institution of Mechanical Engineers*, 186:519–526, 1972.

[150] Alexander V. Potapov and Charles S. Campbell. The two mechanisms of particle impact breakage and the velocity effect. *Powder Technology*, 93: 13–21, 1997.

[151] Alexander V. Potapov and Charles S. Campbell. Parametric dependence of particle breakage mechanisms. *Powder Technology*, 120:164–174, 2001.

[152] K. Pougatch, M. Salcudean, E. Chan, and B. Knapper. Modelling of compressible gas-liquid flow in a convergent-divergent nozzle. *Chemical Engineering Science*, 63:4176–4188, 2008.

[153] Konstantin Pougatch, Martha Salcudean, and Jennifer McMillan. Nozzle design influence on particle attrition by a supersonic steam jet. *Powder Technology*, 209:35–45, 2011.

[154] Pratt-&-Whitney. Homepage called in april 2017, April 2017. URL `http://www.ecopowerenginewash.com/`.

[155] M. Raffel, C. E. Willert, S. Wereley, and J. Kompenhans. *Particle Image Velocimetry*. Springer, 1998.

[156] C. Redeker. *Erosion and removal by dry-ice blasting (in german)*. PhD thesis, University Hannover, 2003.

[157] C. Redeker, F.-W. Bach, and T. Copitzky. Examination of the dry ice removal process for thermal sprayed coatings by particle image velocimetry. *Thermal Spray: Advancing the Science and Applying the Technology*, 1:1279–1284, 2003.

[158] P. M. Render and H. Pan. Experimental studies into hail impact characteristics. *JOURNAL OF PROPULSION AND POWER*, 11:1224–1230, 1995.

[159] Hans Rick. *Gasturbines and Aeroengines (in German)*. Springer Vieweg, 2013.

[160] Yevgeny Rozenblat, Evgeny Grant, Avi Levy, Haim Kalman, and Juergen Tomas. Selection and breakage functions of particles under impact loads. *Chemical EngineeringScience*, 71:56–66, 2012.

[161] A. Rudek. Erosion prediction in pumps and turbines. Technical report, TU Darmstadt, 2013. Seminar report S128.

[162] Alexander Russell, Peter Mueller, and Juergen Tomas. Quasi-static diametrical compression of characteristic elastic-plastic granules - energetic aspects at contact. *Chemical Engineering Science*, 114:70–84, 2014.

[163] Amsini Sadiki. *Gasdynamics*. Technical University Darmstadt, Dept. of Energy and Power Plant Technology, 2013.

[164] A. Samimi, R. Moreno, and M. Ghadiri. Analysis of impact damage of agglomerates: effect of impact angle. *Powder Technology*, 143-144:97–109, 2004.

[165] Michael Schaefer. *Computational Engineering - Introduction to Numerical Methods*. Springer, 2006.

[166] A. Schaffler. Experimental and analytical investigation of the effects of reynolds number and blade surface roughness on multistage axial flow compressors. *Journal of Engineering for Gas Turbines and Power*, 102: 5–12, 1980.

[167] Hermann Schlichting and Klaus Gersten. *Boundary Layer Theory (in German)*. Springer, 2005.

[168] E. Schulson. The fracture of ice. *Journal de Physique Colloques*, 48: 201–220, 1987.

[169] J.N. Scott. Axial compressor deterioration by measuring air intake depression. *Proceedings of the 3rd symposium on gas turbine operations and maintenance, National Research Council of Canada*, 1, 1979.

[170] M. Sezgin and B. Sankur. Survey over image thresholding techniques and quantitative performance evaluation. *Journal of Electronic Imaging*, 13:146–165, 2004.

[171] K. Shimizu, T. Noguchi, H. Seitoh, M. Okadab, and Y. Matsubara. Fem analysis of erosive wear. *Wear*, 250:779–784, 2001.

[172] P. H. Shipway and I. M. Hutchings. Fracture of brittle spheres under compression and impact loading. ii. results for lead-glass and sapphire spheres. *Philosophical Magazine A*, 67:1405–1421, 1993.

[173] P. H. Shipway, J. P. D. Bromley, and D. P. Weston. Removal of coatings from polymer substrates by solid particle blasting to enhance reuse or recycling. *We*, 263:309 – 317, 2007.

[174] Christopher B. Solnordal, Chong Y. Wong, Amir Zamberi, Maharon Jadid, and Zurita Johar. Determination of erosion rate characteristic for particles with size distributions in the low stokes number range. *Wear*, 305:205 – 215, 2013.

[175] M. Sommerfeld and N. Huber. Experimental analysis and modelling of particle-wall collisions. *International Journal of Multiphase Flow*, 25: 1457–1489, 1999.

[176] G. Spur, E. Uhlmann, and F. Elbing. Dry-ice blasting for cleaning: process, optimization and application. *Wear*, 233-235:402–411, 1999.

[177] Joseph Spurk and Nuri Aksel. *Fluid Mechanics*. Springer Verlag, 2008.

[178] K. Sreejith, M.P. Dhrishit, M. Deepu, and T. Jayachandran. Numerical analysis of flow separation in rocket nozzles. *Fluid Mechanics and Fluid Power - Contemporary Research*, 1:1233–1242, 2017.

[179] Peter Stephan, Holger Martin, Stephan Kabelac, Dieter Mewes, Karlheinz Schaber, and Matthias Kind. *VDI Heat Atlas*. Springer, VDI e.V., 2010.

[180] Scott Stratford. Dry ice blasting for paint stripping and surface preparation. *Metal Finishing*, 98:493–499, 2000.

[181] J. Subero, Z. Ning, M. Ghadiri, and C. Thornton. Effect of interface energy on the impact strength of agglomerates. *Powder Technology*, 105: 66–73, 1999.

[182] Charlotte Subero-Couroyer, Mojtaba Ghadiri, Nathalie Brunard, and Frederic Kolenda. Analysis of catalyst particle strength by impact testing: The effect of manufacturing process parameters on the particle strength. *Powder Technology*, 160:67–80, 2005.

[183] Kenneth L. Suder, Rodrick V. Chima, Anthony J. Strazisar, and William B. Roberts. The effect of adding roughness and thickness to a transonic axial compressor rotor. *Proceedings of the 39th International Gas Turbine and Aeroengine Congress and Exposition, The Hague, The Netherlands*, 1: 1–20, 1994.

[184] G. Sundararajan and P. G. Shewmon. The oblique impact of a hard ball against ductile, semi-infinite target materials - experiment and analysis. *International Journal of Impact Engineering*, 6:3 – 22, 1987.

[185] G. Sundararajan and Y. Tirupataiah. The localization of plastic flow under dynamic indentation conditions: I. experimental results. *Acta Materialia*, 54:565–575, 2006.

[186] E. Syverud and L. E. Bakken. Online water wash tests of ge j85-13. *Proceedings of GT2005 - ASME TurboExpo, Reno-Tahoe, USA*, 1:1–9, 2005.

[187] E. Syverud and L.E. Bakken. The impact of surface roughness on axial compressor performance deterioration. *Proceedings of GT2006 - ASME TurboExpo, Barcelona, Spain*, 1:491–501, 2006.

[188] Elisabet Syverud. *Axial Compressor Performance Deterioration and Recovery through Online Washing*. PhD thesis, Norwegian University of Science and Technology, Trondheim, Norway, 2007.

[189] Elisabeth Syverud, Olaf Brekke, and Lars E. Bakken. Axial commpressor deterioration caused by saltwater ingestion. *Proceedings of GT2005 - ASNME TurboExpo, Reno-Tahoe, USA*, 1:1–11, 2005.

[190] F.X. Tanner. Liquid jet atomization and droplet breakup modeling of non-evaporating diesel fuel sprays. *SAE International Journal of Engines*, 106: 127–140, 1998.

[191] C. M. Tchen. *Mean value and correlation problems connected with the motion of small particles suspended in a turbulent fluid*. PhD thesis, TU Delft, Civil Engineering and Geosciences, Hydraulic Engineering, 1947.

[192] C. Thornton, K. Yin, and M.J. Adams. Numerical simulation of the impact fracture and fragmentation of agglomerates. *Journal of Applied Physics*, 29:424–435, 1996.

[193] C. Thornton, M.T. Ciomocos, and M.J. Adams. Numerical simulations of agglomerate impact breakage. *Powder Technology*, 105:74–82, 1999.

[194] Y. Tirupataiah and G. Sundararajan. A dynamic indentation technique for the characterization of the high strain rate plastic flow behaviour of ductile metals and alloys. *Journal of Mechanics and Physics of Solids*, 39: 243 – 271, 1991.

[195] Z.B. Tong, R.Y. Yang, A.B. Yu, S. Adi, and H.K. Chan. Numerical modelling of the breakage of loose agglomerates of fine particles. *Powder Technology*, 196:213–221, 2009.

[196] J. Tuhkuri. Analysis of ice fragmentation process from measured particle size distributions of crushed ice. *Cold Regions Science and Technology*, 23: 69–82, 1994.

[197] E. Uhlmann, M. Kretzschmar, F. Elbing, and V. Mihotovic. Deburring with co2 snow blasting. *Burrs - Analysis, Control and Removal*, 8:181–187, 2010.

[198] Eckhart Uhlmann, Robert Hollan, and Adil El Mernissi. Dry ice blasting - energy-efficiency and new fields of application. *Engineering Against Fracture: Proceedings of the 1st Conference*, 1:399–409, 2009.

[199] Markus Varga, Christoph Goniva, Karl Adam, and Ewald Badisch. Combined experimental and numerical approach for wear prediction in feed pipes. *Tribology International*, 65:200–206, 2013.

[200] Mario Vargas, Charles Ruggeri, Peter Struk, Mike Pereira, Duane Revilock, and Richard Kreeger. Ice particle impacts on a flat plate. *SAE Technical Paper*, 2099:1–23, 2015.

[201] German Vidaurre and John Hallett. Particle impact and breakup in aircraft measurement. *Journal Of Atmospheric And Oceanic Technology*, 26: 972–983, 2008.

[202] J. Tomas W. Schubert, M. Khanal. Impact crushing of particle-particle compounds - experiment and simulation. *International Journal of Mineral Processing*, 75:41–52, 2005.

[203] Stephen Wall, Walter John, Hwa-Chi Wang, and Simon L. Goren. Measurements of kinetic energy loss for particles impacting surfaces. *Aerosol Science and Technology*, 12:926 – 946, 1990.

[204] Wei wei Liu, Bin Zhang, Yan zeng Li, Yan ming He, and Hong chao Zhang. An environmentally friendly approach for contaminants removalusing supercritical co2 for remanufacturing industry. *Applied Surface Science*, 292:142–148, 2014.

[205] D.P. Weston, P.H. Shipway, and S.J. Harris. Coating removal from an industrial polypropylene blend by cryogenic blasting: the development of substrate damage. *Wear*, 258:392–401, 2005.

[206] D. C. Wilcox. Multiscale model for turbulent flows. *AIAA-Journal*, 26: 1311–1320, 1988.

[207] Chong Y. Wong, Christopher Solnordal, Anthony Swallow, and Jie Wu. Experimental and computational modelling of solid particle erosion in a pipe annular cavity. *We*, 303:109–129, 2013.

[208] X. Yang, X. Shen, J. Long, and H. Chen. An improved median-based otsu image thresholding algorithm. *AASRI Procedia*, 3:468–473, 2012.

[209] Shuo Yin, Meng Zhang, Zhiwei Guo, Hanlin Liao, and Xiaofang Wang. Numerical investigations on the effect of total pressure and nozzle divergent length on the flow character and particle impact velocity in cold spraying. *Surface & Coatings Technology*, 232:290–297, 2013.

[210] Y.Tirupataiah, B.Venkataraman, and G.Sundararajan. The nature of the elastic rebound of a hard ball impacting on ductile, metallic target materials. *Materials Science & Engineering, A: Structural Materials: Properties, Microstructure and Processing*, 124:133–140, 1990.

[211] L. Yujuan, L. Kun, J. Tai, and F. Jianren. Comparative studies of shock interaction with static and moving cylinders through immersed boundary method. *Proceedings of the 9th International Conference on Multiphase Flow, Firenze, Italy*, pages 1–6, 2016.

[212] Hongwei Zhang and Xiaohui Dong. Finite element analysis of multiple solid particles erosion in cermet coating. *Surface and Coatings Technology*, 262:184 – 190, 2015.

[213] S. Zhang, K. Dam-Johansen, S. Nørkjær, P. L. Bernad Jr, and S. Kiila. Erosion of wind turbine blade coatings - design and analysis of jet-based laboratory equipment for performance evaluation. *Progress in Organic Coatings*, 78:103–115, 2015.

[214] Y. Zhang, B. S. McLaury, S. A. Shirzai, and R. D. Russel. Simulations of particle-wall-turbulence interactions, particle motion and erosion with a commercial cfd code. *Proceedings of 2006 ASME Joint U.S. - European Fluids Engineering Summer Meeting, Miami Florida*, 2006.

[215] Y. Zhang, B. S. McLaury, S. A. Shirzai, and R. D. Russell. Simulations of particle-wall-turbulence interactions, particle motion and erosion in with a commercial cfd code. *Proceedings of FEDSM2006, 2006 ASME Joint U.S. - European Fluids Engineering Summer Meeting, Miami, Florida, USA*, 1:1 – 16, 2006.

[216] S. Zhen and G.J. Davies. Calculation of the lennard-jones n-m potential energy parameters for metals. *Physica Status Solidi*, 78:595–605, 1983.

[217] B. Zouari and M. Touratier. Simulation of organic coating removal by particle impact. *Wear*, 253:488 – 497, 2002.

A Appendix to Chapter 4: Dry-ice injection system modelling

A.1 Single particle post-processing

Given the nature of the observed dilute laden flow, the experimental approach can be classified as Particle Tracking Velocimetry (PTV) [3, 155]. Utilizing the above HSC system results in a multi-frame single-exposure (continuous illumination) methodology, following the nomenclature from [3]. The signal-to-noise ratio (SNR)

$$SNR = \frac{\mu_I}{\sigma_{BG}} \tag{A.1}$$

achieved is at a value of approximately 5.8 for the most critical case (smallest particle encountering strongest acceleration). This value is given by the mean signal intensity value μ_I divided by the standard deviation of the background intensities σ_{BG} after [155]. The post-processing of the sequences recorded utilizes of the intensity based "centre of mass" centroid matching approach [23, 36].

To ensure reliable post-processing, some image preparation must be done before the actual tracking. First, a background separation procedure is executed to isolate particle information from background and surrounding information (i.e. the nozzle). The modified intensity matrix $I^{\star}_{ij}$ results from the original recording containing particles (superscripted $\{P\}$) and a representative background data recording without particles (superscripted $\{0\}$ and recorded at a moment $t_0 \neq t$).

$$I^{\star}_{ij}(t) = I^{\{P\}}_{ij}(t) - I^{\{0\}}_{ij}(t_0)\,. \tag{A.2}$$

After this, the intensity matrix of the corresponding frame undergoes a threshold valuing procedure according to Eqn. (A.3). It sets particle intensities to 1 and background intensities to 0. The appropriate threshold value $trv^{\star}$ is estimated as the lowest intensity value definitely belonging to a POM particle. It is determined by means of an a priori calibration. The resulting binary intensity matrix $I_{ij}^{\star\star}$ contains only particle information.

$$I_{ij}^{\star\star}(t) = \begin{cases} 1 & ...if\ I_{ij}^{\star}(t) \geq trv^{\star} \\ 0 & ...if\ I_{ij}^{\star}(t) < trv^{\star} \end{cases} \tag{A.3}$$

Now, the above mentioned centre of mass (here the centre of intensity) based centroid matching approach is used to calculate the distance of a POM particles centroid between two recorded frames as follows:

$$\zeta_{dir}(t) = \frac{\sum_{i=1}^{n}\sum_{j=1}^{m}\left[x_i \cdot I_{ij}^{\star\star}(t)\right]}{\sum_{i=1}^{n}\sum_{j=1}^{m}\left[I_{ij}^{\star\star}(t)\right]} \tag{A.4}$$

The estimation of the size-weighted particle position information $\zeta_{dir}(t)$ (example: $dir{=}x$ for the axial direction) at discrete times (here in single frames) with Eqn. (A.4) allows calculation of particle displacement between two consecutive frames Δx by Eqn. (A.5). This approach is prone to biased or unsteady intensity information, even if it is reported to be applicable for asymmetric particles in [36].

$$\Delta x = \zeta_x(t_2) - \zeta_x(t_1) \tag{A.5}$$

By means of the spatial and temporal discretization of the HSC, the mean absolute velocity between two recorded frames can be derived (in 2D). The aforementioned critical case (smallest particle travelling at highest velocity) leads to around 16 frames containing single particles travelling along the nozzle length L. The critical mean axial displacement is found to be approximately 10 mm.

Over this maximum distance, the resulting velocity information (even if defined as local) is averaged.

Another uncertainty may result from the threshold evaluation technique presented in Eqn. (A.3). To account for this, a threshold value based particle sizing study was done, which revealed a maximum difference between given particle diameters and post-processed ones of +/-6.5%. This value is assumed to be the maximum possible displacement error introduced by post-processing due to misinterpreted particle size. It should be noted that this possible error is in the range of the production inaccuracy of the POM particles used, which is given as +/-5.0%.

A.2 Details of the experimental validation study

Table A.1 contains all experimentally derived correlation constants from Eqn. (4.1) in Section 4.1.2, which describes the particle velocities inside the validation nozzle as a function of the nozzle length.

	$C_2^{\{s\}}$ [m/s]			$C_1^{\{s\}}$ [m/s]			$K_{err}^{\{s\}}$ [1]		
	(2bar)	4bar	6bar	(2bar)	4bar	6bar	(2bar)	4bar	6bar
1.5mm	16.239	24.879	33.611	72.831	103.520	129.060	0.14	0.13	0.09
2.0mm	13.810	21.740	29.956	67.260	94.824	116.160	0.15	0.09	0.08
2.5mm	11.322	20.220	25.727	60.532	87.981	103.270	0.16	0.09	0.08
3.0mm	12.096	20.057	23.572	61.200	83.977	100.025	0.17	0.10	0.09

Table A.1.: Empirical constants for the correlation from Eqn. (4.1) (2 bar case valid until x/L=0.6 relative nozzle length).

A.3 Details of the numerical set-up study

Further details of the numerical set-up used for the particle laden flow validation are given below. The spatial discretization of the relevant numerical volume is made by means of scalable block-meshing technique with respect to sufficient resolution of the boundary layers (a priori estimated first cell:

$y+ \leq 1$, at least 30 cells in boundary layer) as well as to regions where strong gradients are expected. The Ansys MESHER tool, versions 15.0 and 16.2, was utilized and meshing details are presented in Fig. A.1. Preliminary grid- and ambience-independence studies led to a total problem description consisting of approximately 7,500,000 grid-points. The ambient proportion considered is $150 \cdot D^{\{L\}}$ long and it has a radius of $50 \cdot D^{\{L\}}$(see Fig. 4.5 in Section 4.2.1 for details).

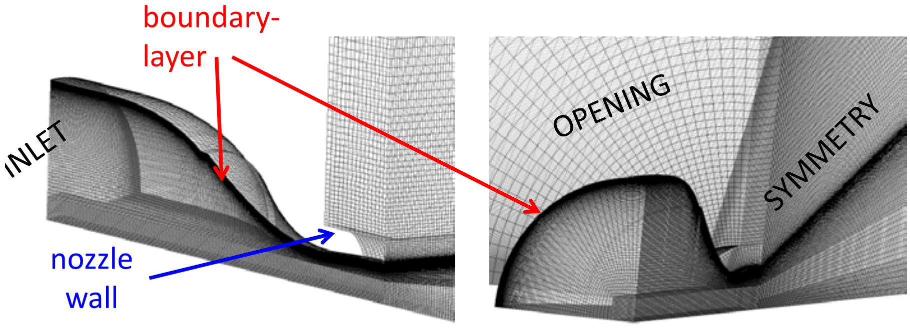

Figure A.1.: Details of a representative nozzle meshing.

Boundary conditions selected are nozzle gauge pressure and total temperature at the inlet as well as open boundaries at the outlets, allowing an entrainment of the surrounding air. Axial particle velocity (from experimental measurement) and random radial injection positions are selected as inlet conditions for the dispersed phase. Ambient pressure and temperature are: $p_{amb} = 101,480\,Pa$ and $T_{amb} = 15.70°C$ for all cases simulated with particles (according to experimental conditions to which the simulations are referred). In case of the literature based air flow validations corresponding ambient conditions are considered. The most important grid and set-up information is summarized in Tab. A.2.

An all encompassing data comparison from the validation study of the pure air flows is discussed in the following. The results presented in Section 4.2.1 approximately coincide and the same conclusions can be drawn for the Mach number profiles compared for the subsonic compressible test case in Fig. A.2 and for the supersonic test case in Fig. A.3 with data from the study presented in [79]. In both Figures A.2 and A.3 the right-hand graph shows the radial jet profiles at a downstream position x/D=1 and the right-hand graph these at

GRID	Scalable	Grid study	Critical element size $h/D^{\star}$	No. of layers in boundary layer	Total no. of grid points	Boundary layer first cell y+
	yes	yes	0.015	30	7,500,000	1

SET-UP	State	Turbulence	Pseudo Timestepping	Advection Schemes	Turbulence Numerics	Energy equation
step1	steady	$k-\varepsilon$	physical, adaptive	Upwind	1st order	isothermal
step2	steady	$k-\varepsilon$	physical, $\delta t < \frac{D^{\star}}{u^{\star}}$	High-Res	High-Res	total energy

Table A.2.: Most important grid and set-up information of the nozzle simulations.

x/D=10. The most significant deviation between the experimental data and both numerical solutions can be seen in Fig. A.3, right.

While the jet core prediction from the study presented here approximately coincides with the experimental data, the numerical solution from [79] clearly overpredicts the experimental outcomes in the core of the jet. Further away from the core the situation changes and the simulations presented here tend to overpredict the reported experimental Mach numbers while the simulated results from [79] are closer to the experiment, but still overpredicting. The

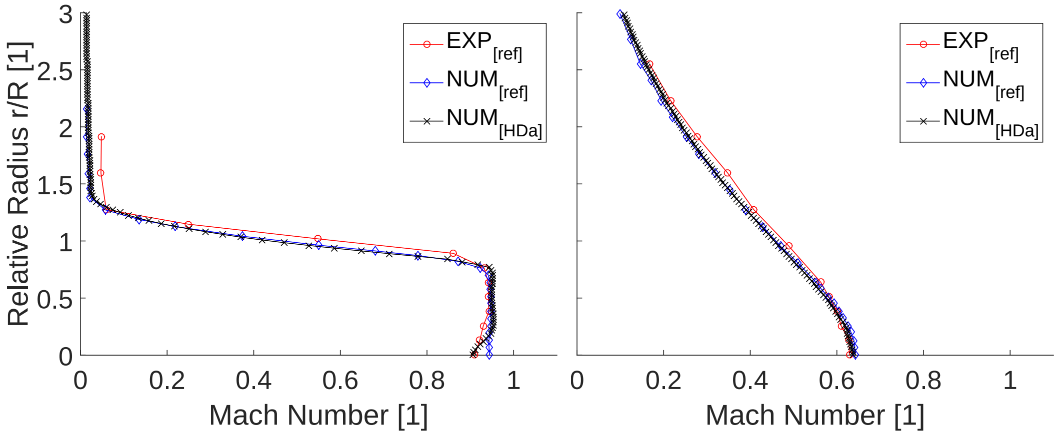

Figure A.2.: Compressible subsonic test case - comparison of Mach number profiles at x/D=1 (left) and x/D=10 (right); numerical data with numerical and experimental data from [79].

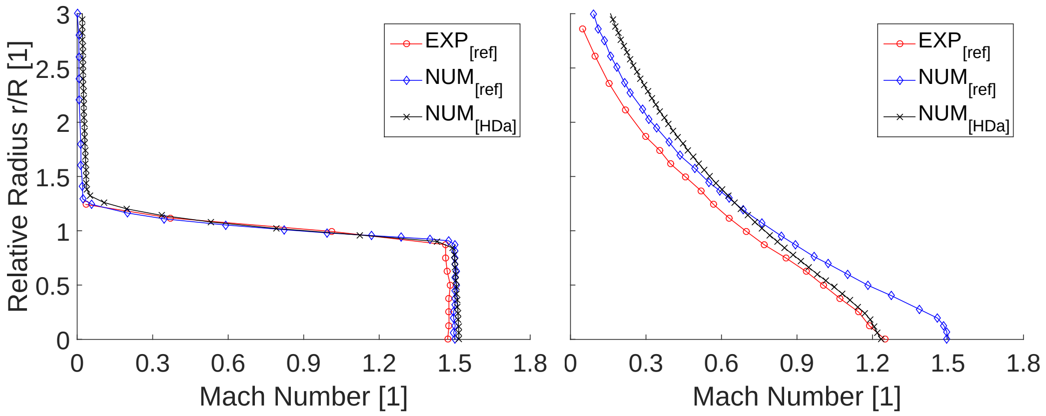

Figure A.3.: Supersonic test case - comparison of Mach number profiles at x/D=1 (left) and x/D=10 (right); numerical results vs. numerical and experimental data from [79].

remaining trends from Fig. A.2 and A.3 show good overall agreement between experiment and both simulations.

A numerical evaluation of all results from this validation study is given below. Its results are used to assess the quality of the simulation set-up presented here. The general formulation in Eqn. (A.6) is introduced to quantify mean deviations between experimental and numerical data.

$$\Lambda_\phi = \left[\frac{\int \left(\bar{\phi}_{exp} - \bar{\phi}_{num} \right)^2 d\zeta}{\int \bar{\phi}_{exp}^2 \, d\zeta} \right]^{\frac{1}{2}} \tag{A.6}$$

It describes the cumulative (any direction ζ) squared deviation Λ of any value ϕ between experimental and numerical data (indices exp and num) in relation to the cumulative and squared experimental data. Taking the square root of this reveals the average deviation ratio of experimental and numerical results. This value Λ is used for all comparison discussions in this work. It should be noted that due to the exponent in Eqn. (A.6) it does not account for the direction of the deviation.

Table A.3 contains deviations encountered between experimental data from [79, 144] and the validation simulations presented here. The variables considered with respect to Eqn. (A.6) are pressure ratio ($\phi = p/p_{amb}$) along the nozzle wall ($\zeta = x/L$) as well as Mach number profiles in the expanding jet ($\phi = Ma$ and $\zeta = r/R$) at various axial positions x/D downstream the nozzle outlet. The comparison study shows maximum deviations of 13 % in the case of supersonic flow and 9 % in the subsonic case. The deviations tend to increase for increasing axial position in the supersonic case and decrease in the subsonic case. Based on this final comparison, the above simulation set-up is stated to be valid when taking into account the deviations presented.

To ensure the validity of the set-up also for subsonic flows, the study from PANCHAPAKESAN and LUMLEY [144] was selected to be simulated and compared to published experimental results. In [144] the authors above used self-similarity effects of subsonic free jets to normalize their results and provided normalized axial and radial velocity profiles. The actual velocity is related to jets local top-hat velocity $u_S(x/D)$ and this relation is plotted as a function of the radius of the jet related to the absolute axial coordinate r/x at various axial position x/D downstream the nozzle outlet.

The comparison between the simulations made with the above set-up and experimental data from [144] shows good overall agreement for axial velocity profiles (Fig. A.4, left) and for (very slow) radial velocities (Fig. A.4, right). The axial profile overprediction at the edge of the jet is comparable to what was observed for the supersonic jet at particular downstream positions (Fig. A.3,

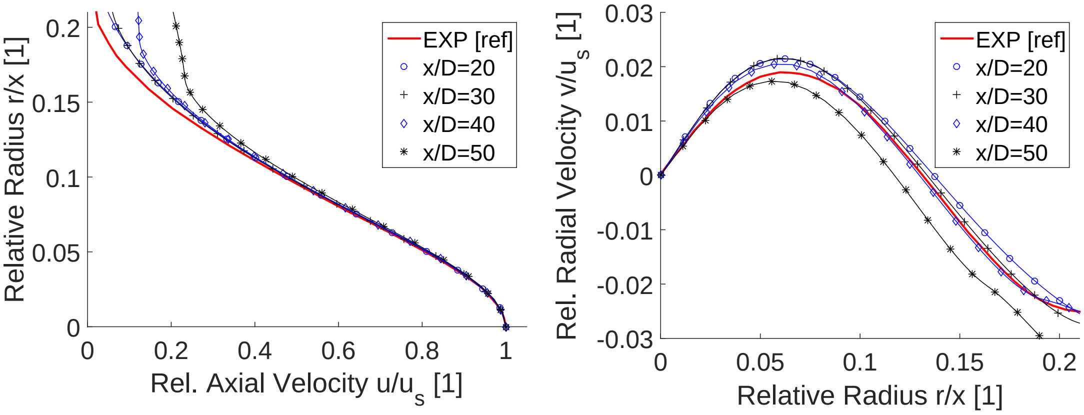

Figure A.4.: Incompressible subsonic test case - comparison of normalized velocity profiles (left - axial, right - radial) at various axial positions x/D; numerical data with experiment from [144].

right). This effect increases further away from the core. It can be seen also from the values in Tab. A.3, where the assessment of the subsonic case, calculated with Eqn. (A.6) and $\phi = u/u_S$ and $\zeta = r/x$, is listed in the last row.

All differences encountered here are acceptable in the context of this work. The main goal of the study is to simulate particle tracks throughout the nozzles until their ejection and the jet core predictions of the set-up presented are in good agreement with the measurements. The maximum average differences encountered are located further downstream of the nozzles and their values are approximately +/-13 %.

case	p/p_{amb}	Ma @ $x/D = 1$	Ma @ $x/D = 3$	Ma @ $x/D = 5$	Ma @ $x/D = 10$
supersonic	n.a.	4 %	7 %	10 %	13 %
subsonic, compressible	12 %	9 %	6 %	5 %	3 %

		u/u_S @ $x/D = 20$	u/u_S @ $x/D = 30$	u/u_S @ $x/D = 40$	u/u_S @ $x/D = 50$
subsonic, incompressible	n.a.	5 %	7 %	9 %	12 %

Table A.3.: Average deviation ratios of experimental [79, 144] and numerical results at various downstream positions x/D for air flow validation cases; values calculated with Eqn. (A.6) in %.

A.4 Detailed results of the validation study

The following discussion represents detailed outcomes from the simulations with 1-way and 2-way coupling particle tracking set-up. These are referred to as 1-wc and 2-wc in the plots. Also, the 2-way coupled solution was parametrized considering the contribution of the pressure gradient force, Eqn. (2.70), referred to as F_{dp} in the plots. It turns out to have a strong influence upon the resulting particle tracks. The second force contribution considered in the right-hand side of Eqn. (2.64) is the drag force according to Eqn. (2.66), which is referred to as F_{drag} in the plots. It is considered in all cases presented here.

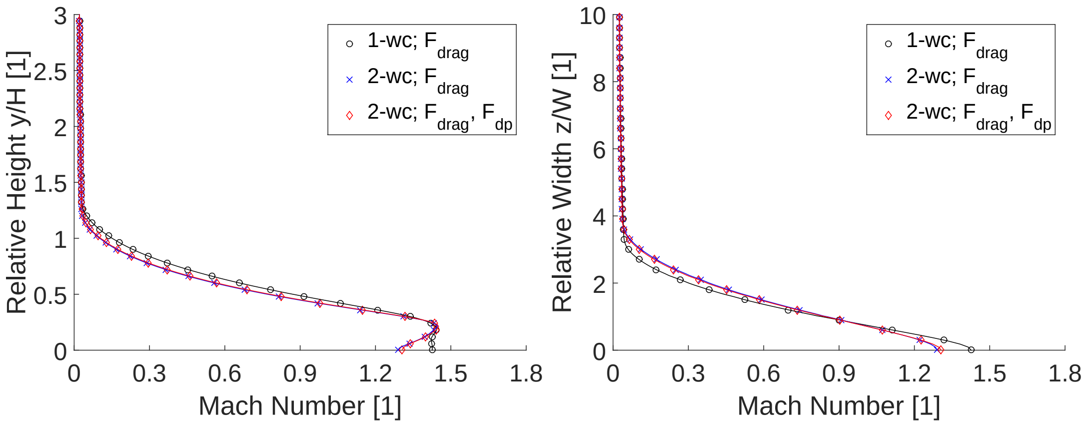

Figure A.5.: Mach number profiles of the particle laden flow for the height (left) and the width axis (right); various simulation set-ups; downstream location x/D=3.

From Fig. A.5, which shows a representative portion of the compared datasets, the influence of the coupling method and the composition of the particles ODE of motion on the emerging free jet can be seen. The Mach number profiles displayed change slightly due to particle-fluid interaction. Lower Mach number values can be found in the core of the jet and slightly higher Mach number values at its edges if 2-way coupling is selected. There is no significant effect detected from the pressure gradient force.

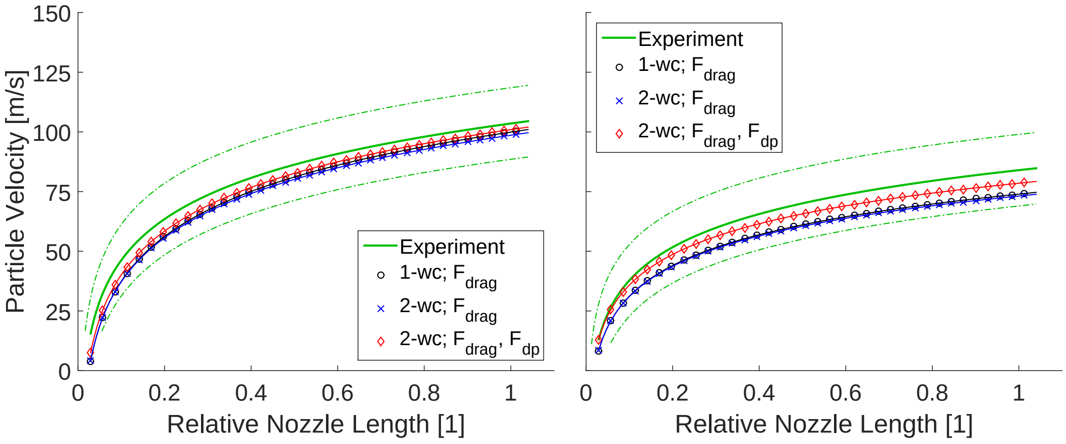

Figure A.6.: Influence of the coupling strategy and the pressure gradient force upon the particle tracks at 4 bar, 1.5 mm POM particles (left) and 3.0 mm POM particles (right); comparison of trend lines from simulation and experiment.

Figure A.6 reveals the effect of the pressure gradient force on the particle acceleration and its influence increases with increasing particle size. The left hand side of Fig. A.6 shows the correlated particle velocity trends from the experiments presented in Section 4.1.2 (with dash-dotted upper and lower bounds) compared to the three above simulation set-ups for the smallest 1.5 mm POM particles and 4 bar system pressure. The right-hand side of Fig. A.6 shows the same situation for the largest 3.0 mm POM particles. It turns out that the particle velocity trends from the simulations with consideration of the pressure gradient force are closer to the mean experimental outcomes then the other results. This effect is more significant for the larger particles compared to small particles.

All results achieved lie inside the experimental scattering boundaries. These are plotted as dash-dotted trends in Fig. A.6 above and below the mean experimental trends and thy are derived from the slowest and the fastest particles encountered in the experiments. Further investigation of the data revealed that the impact of the pressure gradient force increases with increasing system pressure. It is therefore concluded that the pressure gradient force is not negligible in general for the simulations related to this study.

Table A.4 contains an overview of the most important comparisons from the particle-laden flow study. These are evaluated by means of Eqn. (A.6) with $\phi = \left|\mathbf{v}_P\right|$ and $\zeta = x/L$, discussing only particle data. The discussion of the first column block (titled Methods @ 4 bar) reveals no significant difference between the 1-way coupled (1-wc) and the 2-way coupled (2-wc) solutions. But the contribution of the pressure gradient force has a significant effect upon the predictive capabilities of the simulations (see sub-column titled 2-wc, Fdp), almost bisecting the deviation between the numerical and the experimental outcomes, which can clearly be seen also in Fig. A.6, right.

The results presented in the second column block of Tab. A.4 (titled BEST: 2-wc & Fdp) show the comparison of mean numerical and experimental results. The numerical results are achieved with the best numerical set-up tested in this work (i.e. 2-way coupling and consideration of pressure gradient force). All mean

	Methods @ 4 bar			BEST: 2-wc & Fdp			NUM-EXP (scattering)		
Particles	1-wc	2-wc	2-wc,Fdp	(2 bar)	4 bar	6 bar	(2 bar)	4 bar	6 bar
1.5 mm	7 %	8 %	5 %	7 %	5 %	8 %	-7 %	-8 %	-1 %
2.0 mm	12 %	12 %	8 %	7 %	8 %	8 %	-8 %	-1 %	0 %
2.5 mm	13 %	13 %	8 %	7 %	8 %	6 %	-9 %	-1 %	-2 %
3.0 mm	13 %	14 %	7 %	6 %	7 %	9 %	-11 %	-3 %	0 %

Table A.4.: Comparison of experimental and numerical results of particle velocities according Eqn. (A.6) in % (2 bar until x/L=0.6).

deviations presented are lower than 10 % which is decided to be acceptable for the studies presented in what follows.

The last column block of Tab. A.4 contains an evaluation of the magnitude of the deviations of numerical values from experimental values in relation to the experimental variance. The latter is represented by K_{err} from Eqn. (4.1) and its values are listed in Tab. A.1 and 4.1. Negative numbers in the last column block of Tab. A.4 indicate numerical results inside the experimental scattering bounds. There are no positive figures, which means that the mean numerical predictions fit the experiment well with respect to its maximum scattering. This situation is also visible from Fig. A.6 (i.e. all simulated trends lie inside the experimental bounds).

A.5 Post-processing of dry-ice laden flows

This section describes the details of the post-processing method used to automatically detect, size and track dry-ice particles in particle laden jets with up to 800 particles per frame. The ambiguity problem of automatized particle association for particle tracking in these dry-ice flows is solved by utilizing an idea originally presented by HERING et al. [82], who used particle-size normalized grey value continuity in a modified streak-overlapping technique.

The HSC data recorded with the set-up presented in Section 4.3.1 is post-processed to derive desired physical values. All post-processing is done by means of Matlab 2014b procedures developed, tested and validated in this study. After classifying image noise by means of spectral analysis, the HSC recordings (here intensity matrices $\mathbf{I}$ at various instants of time t) are filtered in frequency domain utilizing an adjustable filter technique $f(\omega)$. Improved intensity matrices $\mathbf{I}^\star$ of certain frames t result:

$$\mathbf{I}_t^\star = \mathscr{F}^{-1}\left\{\mathscr{F}\left(\mathbf{I}_t\right)\cdot f(\omega)\right\} \tag{A.7}$$

This noise classification and filtering procedure is illustrated in Fig. A.7. It can optionally be selected and parametrized in the post-processing procedure, if necessary. Transformation of the original record (leftmost image in Fig. A.7, red frame) from spatial to frequency domain allows an insight into the noise pattern (second image, shifted and centred 2D amplitude spectrum in greyscale). Noise can be reduced by application of selective and bandpass filtering functions in frequency domain (third image, applied filtering functions). Afterwards the filtered image is re-transformed to spatial domain and the background noise is (in this example) removed (rightmost image, blue frame).

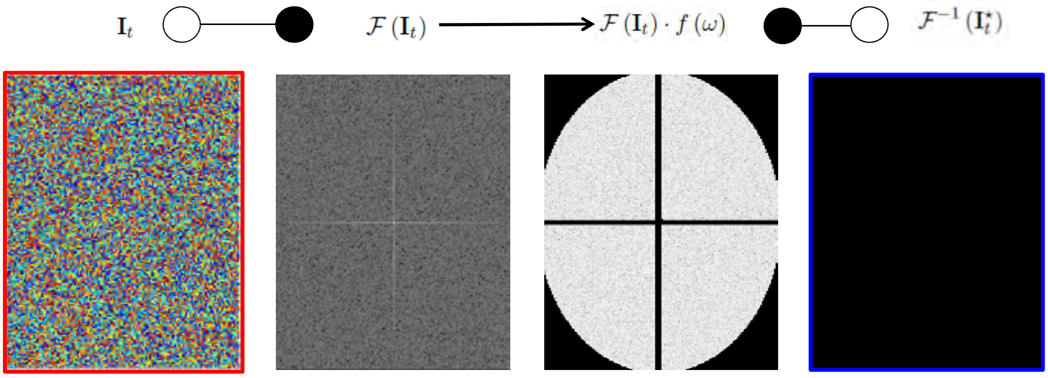

Figure A.7.: Example for noise filtering procedure acc. Eqn. (A.7).

The above filtered matrix $\mathbf{I}^{\star}$ is used for the threshold valuing procedure. Background and particle information is distinguished by means of the clustering method presented by OTSU [142]

$$\sigma^2_{I-II} = p_I(trv) \cdot (\mu_I(trv) - \mu_{tot})^2 + p_{II}(trv) \cdot (\mu_{II}(trv) - \mu_{tot})^2 \tag{A.8}$$

which estimates appropriate threshold values $trv^{\star}$ of bipolar intensity histograms calculating the maximum variance σ^2 between the histogram poles I and II

$$trv^{\star} = f\left(\max\left[\sigma^2_{I-II}\right]\right) \text{....with: } 1 \leq trv^{\star} \leq L. \tag{A.9}$$

These are described by their probability density functions p , their mean values μ and the mean value μ_{tot} of the total dataset in Eqn. (A.8). If background and foreground data are not clearly separable in the intensity histogram (i.e. the second pole of the intensity histogram is weak compared to the first pole), OTSUs method can fail to predict the correct $trv^{\star}$ [170, 208]. In this case, there is an option included in the post-processing to replace the above variance estimator, Eqn. (A.8), by a modified estimator proposed by YANG et al. [208]

$$\sigma^2_{I-II} = p_I(trv)\cdot\left(m_I(trv) - m_{tot}\right)^2 + p_{II}(trv)\cdot\left(m_{II}(trv) - m_{tot}\right)^2 \tag{A.10}$$

who utilized median values m instead of mean values of the original procedure. If this method also fails, the frame is removed from post-processing. Successful outcomes of this threshold valuing procedure lead to second modified matrices $\mathbf{I}^{\star\star}$ of certain frames t, Eqn. (A.11). These contain only particle intensity values. All background values are set to 0.

$$\mathbf{I}^{\star\star}_t(x,y) = \begin{cases} 0 & \text{...if}\,\mathbf{I}^{\star}_t < trv^{\star} \\ I^{\star}(x,y) & \text{...if}\,\mathbf{I}^{\star}_t \geq trv^{\star} \end{cases} \tag{A.11}$$

Furthermore, the aspect ratio

$$AR = \frac{b}{a} \overset{!}{\geq} AR^{MIN},\ \text{...}b \leq a \tag{A.12}$$

of all identified objects in a frame $\mathbf{I}^{\star\star}_t$ is taken into account to eliminate heavily blurred data from post-processing. If the quotient of minimum main length scale b to maximum main length scale a of a particle detected is smaller than a critical value (i.e. $AR^{MIN} = 0.25$), the particle is removed from sizing. This critical value is adjusted in an a-priori experiment with disintegrated dry-ice particles and it is maintained at a constant value for all post-processing considered.

An artificial test-image pair which was processed by the above procedure is presented in Fig. A.8. It was used for verification of the sizing function. The original image in the upper display of Fig. A.8 contains 60 individually shaped particles consisting of individually distributed pixel intensities. Six different particle sizes are placed on a noisy background. The greyscale image in the

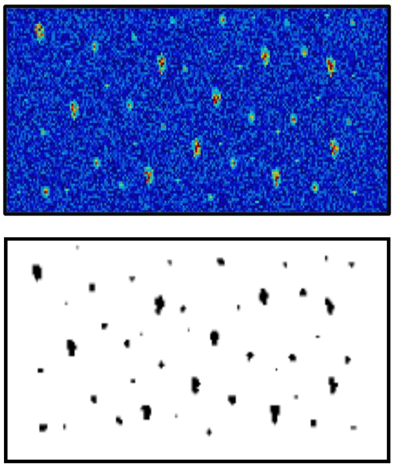

Figure A.8.: Example for particle detection in noisy image by means of Eqn. (A.7) to (A.12), original artificial image (upper) and post-processed image (lower).

lower display of Fig. A.8 results from application of the above filtering and threshold valuing technique.

To size the particles detected in frame t, the intensity matrix $\mathbf{I}^{\star\star}$ from Eqn. (A.11) is treated as a binary matrix, setting all intensity values above 0 to 1. This resulting binary matrix is subscripted S and referred to as $\mathbf{I}^{\star\star}_S$ in what follows. It is used to size detected particles according Eqn. (A.13). For that purpose, an integral over the bounding box area A_{bb} of each particle i in the image (for example bounding boxes of $i = 1...60$ particles in Fig. A.8) is solved. This leads to a size vector $\alpha_{P,i}$. It contains particle sizes (here pixel count) of all particles i found in any investigated frame at a certain instant of time t :

$$\alpha^{\{t\}}_{P,i} = \iint\limits_{A_{bb,i}} \mathbf{I}^{\star\star}_{S,t} dx dy. \tag{A.13}$$

These size values are used to obtain sphere-equivalent diameters $d_{P,i}$ of all particles i assuming their square areas $\alpha_{P,i}$ being square areas of ideal spheres:

$$d^{\{t\}}_{P,i} = \left(\frac{4}{\pi} \cdot \alpha^{\{t\}}_{P,i} \right)^{\frac{1}{2}}. \tag{A.14}$$

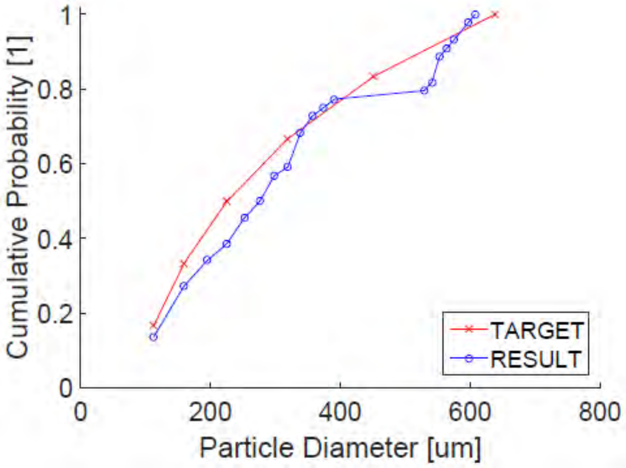

Figure A.9.: Physical values (i.e. cumulative particle size distribution) for the test frame from Fig. A.8, original target values and post-processed result values.

Conversion of the results from Eqn. (A.14) with corresponding spatial discretization values from the experiment leads to physical values (i.e. particle diameters in mm).

Adopting this procedure to size all particles from the above test-image leads to the particle size distribution displayed in Fig. A.9, where post-processed data is compared to original data. It can be seen that the exact information content of the image is altered by the above procedure, but the general trend of the particle size distribution is still governed. Single pixel information is lost due to the filtering and threshold valuing procedures applied. The remaining particles are slightly modified because they partially consist of intensity values comparable to background intensities.

However, a good approximation of the real result is achieved by classifying the detected particles into appropriate size-class bins. The size of these bins is dependent on the spatial discretization. An assessment experiment with POM particles of various sizes (i.e. particle diameters from 0.5 mm to 3.0 mm were considered) and shape (i.e. spherical particles and non-spherical granules were considered) revealed a predictive accuracy of +/-6.5 % in particle diameter, which is the maximum deviation encountered with the above procedure.

The same procedure as described in Eqn. (A.13) for sizing leads to the formulation of an energy vector $\varepsilon_{P,i}$ according to Eqn. (A.15), which is applied for particle tracking. It utilizes the intensity matrix $\mathbf{I}^{\star\star}$ instead of the binary matrix $\mathbf{I}_S^{\star\star}$. This leads to another vector $\varepsilon_{P,i}$ which contains summarized intensity values of each particle i in any frame at a certain instant of time t.

$$\varepsilon_{P,i}^{\{t\}} = \iint\limits_{A_{bb,i}} \mathbf{I}_t^{\star\star} dx dy \tag{A.15}$$

To obtain 2D velocity vectors of particles, a centroid matching approach between associated particles of two consecutive frames is chosen (see for example ADRIAN [3], BRADY et al. [23], CHEEZUM et al. [36]).

The ambiguity problem of automatized particle association in such densely laden dry-ice flows is solved by utilizing an idea originally presented by HERING et al. [82], who reported that a unique matching criterion for particle laden flows with up to 800 particles per frame-pair can be found if the particle size and its pixel energy (i.e. the grey value continuity) is taken into account resulting in the modified streak-overlapping technique.

In this work, the procedure utilizes a comparable criterion $e_{P,i}$ which incorporates particle pixel energy $\varepsilon_{P,i}$ from Eqn. (A.15) and its size $\alpha_{P,i}$, Eqn. (A.14):

$$e_{P,i}^{\{t\}} = \varepsilon_{P,i}^{\{t\}} \cdot \alpha_{P,i}^{\{t\}}. \tag{A.16}$$

The values e_P from two consecutive time steps $\{t\}$ and $\{t+1\}$ are compared in a residual formulation

$$C_i^{\{(t):(t+1)\}} = \max \left[1 - \frac{\left| e_{P,i}^{\{t\}} - e_{P,(1:n)}^{\{t+1\}} \right|}{\left| e_{P,i}^{\{t\}} + e_{P,(1:n)}^{\{t+1\}} \right|} \right] \overset{!}{\geq} C_i^{MIN} \tag{A.17}$$

which accounts for the e-value of certain particles i from the first frame $\{t\}$ and e-values from all particles $(1:n)$ found in the second frame $\{t+1\}$. Its purpose is to find minimal differences. This leads to an ambiguity matrix $\mathbf{C}$ containing all possible particle associations and their correlation probability (1 = ideal, 0 = no correlation). Moderately changing flow, ambient and illumination conditions as well as particle modifications (i.e. rotation) in two consecutive frames are considered by means of an acceptance limit (i.e. $C_i^{MIN} = 0.9$). Most probable particle pairs are then associated by means of Eqn. (A.17).

Next, physical plausibility of a possible match j is checked by means of a criterion comparable to Eqn. (A.17)

$$C_{ecc,j}^{\{(t):(t+1)\}} = \left[1 - \left(\frac{2 \cdot \min \left[ecc_{P,j}^{\{t\}}, ecc_{P,j}^{\{t+1\}} \right]}{ecc_{P,j}^{\{t\}} + ecc_{P,j}^{\{t+1\}}} \right) \right] \overset{!}{\geq} C_{ecc}^{MIN} \tag{A.18}$$

to quantify the agreement of the matched particles shape in both frames $\{t\}$ and $\{t+1\}$ by means of their elliptical eccentricity values. These are calculated as follows

$$ecc_{P,j} = \left(1 - \left(\frac{b}{a} \right)^2 \right)^{\frac{1}{2}} \tag{A.19}$$

with their main axis lengths. In Eqn. (A.18), a certain predefined deviation (i.e. $C_{ecc}^{MIN} = 0.75$) must be allowed, since the particles investigated (i.e. dry-ice) are non-spherical and they can change their appearance due to rotation or disintegration between two time-steps.

An a priori investigation of representative recordings leads to the evaluation of a second plausibility criterion which incorporates the flow angle γ and which allows only a maximum limit for valid matches (i.e. $\gamma^{MAX} = 5°$):

$$\gamma_{P,j}^{\{(t):(t+1)\}} \overset{!}{\leq} \gamma^{MAX} \tag{A.20}$$

All potential particle pairs from Eqn. (A.17) which do not match the plausibility criteria assessed by Eqn. (A.18) and (A.20) are removed from tracking. Only particles which match the above acceptance limits are considered.

The 2D velocity vectors of these remaining particle pairs j can be estimated automatically using centroid matching:

$$\mathbf{v}_{P,j} = \frac{\triangle \mathbf{x}_j}{\triangle t}. \tag{A.21}$$

A comparison study in which automatically generated particle tracks from the procedure presented above are compared to tracks where particle matching was done manually (i.e. the ambiguity criterion from Eqn. (A.17) was replaced by user defined particle-pair indication) revealed maximum deviations for automatically tracked velocities of +/-5%.

An example for tracking results from the post-processing of an actual dry-ice laden flow is presented in Fig. A.10 and its left-hand display shows two consecutive frames of the particle laden flow emerging nozzle #1 at 8 bar system pressure. The frames are overlaid (frame $\{t+1\}$ under semi-transparent frame $\{t\}$) and pixel colours indicate the corresponding intensity values. The frames contain a total of 30 single particles, from which 6 are automatically considered for tracking. The results from sizing and tracking are shown in Fig. A.10, right. All associated particle pairs are highlighted with coloured circles and boxes in both images.

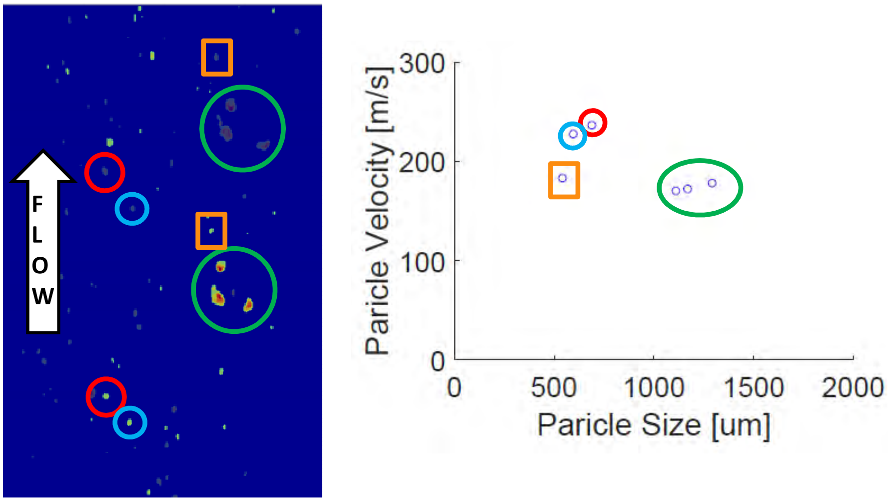

Figure A.10.: Example for particle tracking in a real dry-ice laden flow, consecutive frames overlaid (left) and physical result (right) with particle pairing indication.

A.6 Pre-processing of dry-ice simulations

Particle phase modelling

In the following a procedure is described which is used to link experimental particle data to numerical particle modelling and the numerical calibration procedure of the total number of model particles to be considered in the simulations is presented.

Experimental size distributions of dry-ice particles, $p_{exp}\left(d_P\right)$, are modelled in six representative particle size classes $c = 1...N$ (here $N = 6$) for numerical simulation

$$d_P^{\{c\}} = \left[125 \dots 4000\mu m\right] ...c = 1...6. \tag{A.22}$$

Their probability densities can be derived directly from experimental data

$$p\left(d_P^{\{c\}}\right) = \int\limits_{d_P^{\{c,start\}}}^{d_P^{\{c,end\}}} p_{exp}\, d\left\{d_P\right\} \tag{A.23}$$

considering the above numerical size classes as mean values of the corresponding numerical bins.

A link between this classified particle size distribution $p\left(d_P^{\{c\}}\right)$ and the numerical particle number-rate distribution $p\left(\dot{n}_c\right)$ has to be formulated for each particle size class c. The numerical number-rate describes the number of real particles represented by a single Lagrangian model particle in simulations per unit time. It is defined as follows:

$$\dot{n}_c = \frac{\dot{m}_c}{m_c} \tag{A.24}$$

where $\dot{m}_c$ is the mass flux of a certain particle size class and m_c is the mass of a particle from this class. Since experimental particle size distributions are known and can be classified with Eqn. (A.23) to numerical particle size classes, it is assumed that the final number rate distribution of all particle classes $p\left(\dot{n}_c\right)$ must be equal to the classified particle size distribution:

$$p\left(\dot{n}_c\right) \overset{!}{=} p\left(d_P^{\{c\}}\right) \tag{A.25}$$

Furthermore, in all simulations presented in Section 4.4.1, the number distribution of numerical model particles $p\left(n_P^{\{c\}}\right)$ is chosen to be uniform for all particle size classes N considered, i.e.:

$$p\left(n_P^{\{c\}}\right) = \frac{1}{N} \tag{A.26}$$

For Lagrangian particle tracking in Ansys CFX, mass- and number-rate distributions must be defined initially. Therefore particle mass distributions $p\left(m_P^{\{c\}}\right)$ for all particle size classes have to be calculated from the above classified experimental particle size distribution

$$p\left(m_P^{\{c\}}\right) = \frac{p\left(d_P^{\{c\}}\right) \cdot m_P^{\{c\}}}{\sum\limits_{i=1}^{N} \left[p\left(d_P^{\{i\}}\right) \cdot m_P^{\{i\}}\right]}, \tag{A.27}$$

with $i = 1...N$ representing all particle size classes considered in the simulation (here $N = 6$).

With this formulation the above link between particle number rate distribution $p\left(\dot{n}_c\right)$ and classified experimental particle size distribution $p\left(d_P^{\{c\}}\right)$, Eqn. (A.25), can be calculated:

$$p\left(\dot{n}_c\right) = \frac{p\left(m_P^{\{c\}}\right) \cdot \dot{m}_P}{p\left(n_P^{\{c\}}\right) \cdot n_{P,tot} \cdot m_P^{\{c\}}} \tag{A.28}$$

using the known total particle mass flux $\dot{m}_P$ and a chosen total number of model particles $n_{P,tot}$.

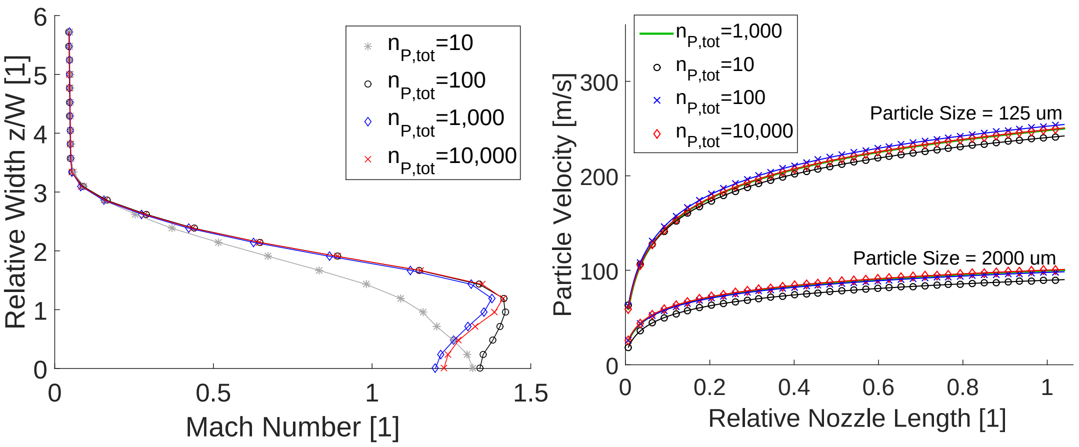

Figure A.11.: Mach number profiles at x/D=1 (left) and particle tracks for selected particle size classes (right) calculated with variable number of model particles.

The latter influences the accuracy of numerical solutions and must be parametrized in a-priori set-up calculations, which was done in this study with nozzle #1 at 8 bar nozzle pressure. Typical results from these initial calculations are discussed in Fig. A.11.

The left hand graph of Fig. A.11 shows Mach number profiles along the width axis at x/D=1 downstream nozzle #1 outlet. Significant differences can be seen between profiles calculated with 10 and 100 model particles, while there is only a negligible difference detectable between profiles from 1,000 and 10,000 model particles. The right-hand graph of Fig. A.11 contains representative particle tracks for two selected particle size classes calculated with the above numbers of model particles.

The most significant difference in particle tracks, all compared to the solution of 1,000 model particles, can be detected for results with 10 model particles. A slight difference is still detectable for 100 model particles and almost no difference can be seen between the predicted tracks from 1,000 and 10,000 simulated model particles.

This case is treated as representative for all nozzle simulations in this work and the number of model particles $n_{P,tot}$ considered in all nozzle simulations is selected to be 1,000.

Temperature effects

To account for the possible heat transfer between dry-ice particles and air in the linking tubes between the blasting machines and the nozzles, a 1D model calculation has been set-up to estimate the air inlet temperatures to the nozzles. This calculation procedure is illustrated schematically in Fig. 4.18 in Section 4.4.1 and the details of the procedure are described below. The number of 1D segments of the tube model in the calculation procedure was parametrized a priori to achieve a result independent from discretization (i.e. comparable to a grid study).

Particle, fluid and geometrical information of the process is necessary for the above estimation and the most important parameter to the results was found to be the particle size distribution. Convection from ambience to the tube was found to be negligible.

The following assumptions turned out to be valid for the final pre-calculations:

- heat-transfer mechanism fluid-particles: Nusselt model for ideal spheres (see e.g. [179])
- particle breakup in tube: linear blend function between initial and final diameter distribution (both known from experiments)
- particle velocity in tube: constant slip-factor from experiments

Further contributors to air temperature have been investigated, but were found to be negligible upon the predicted air temperatures:

- pressure losses in tube: dissipative heating based on pressure-loss estimation (see e.g. [179])
- convective losses via tube wall: Nusselt model for cylinder, free convection (see e.g. [179])
- sublimated mass proportions of CO_2
- dilute dry-ice loading (i.e. 5%)

The particle size distribution $p_i\left(d_P\right)$ in each segment i along the tube (total number of segments s) is estimated as follows

$$p_i\left(d_P\right) = \left[\frac{p_{end}\left(d_P\right) - p_0\left(d_P\right)}{s}\right] \cdot i + p_0\left(d_P\right) \tag{A.29}$$

for all particle size classes introduced for numerical simulations of dry-ice particles (see above, Eqn. (A.22) and (A.23)). The particle sizes are assumed to be uniformly distributed (i.e. $p_0\left(d_P\right)$) at the injection position (Fig. 4.10, pos. (3)) and to be distributed as given from experimental data (i.e. $p_{end}\left(d_P\right)$) at nozzle inlet (i.e. tube outlet).

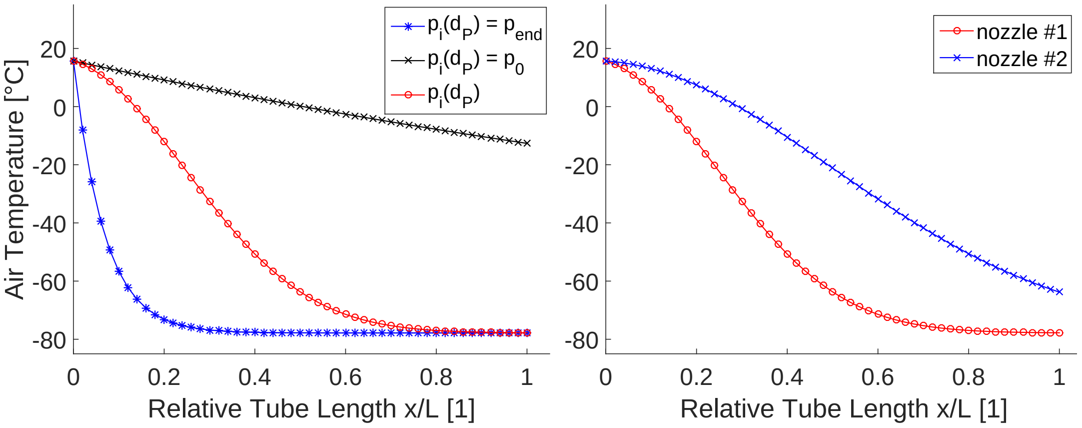

Figure A.12.: Air temperature trends from 1D a priori estimation for various particle size distributions (left) and for fully laden dry-ice flows through the linking tubes of nozzle #1 and #2 (right).

The influence of various discrete particle size distributions inside the tube upon the estimated air temperature at the nozzle inlet is shown in Fig. A.12, left. If uniform initial distribution of particles is assumed throughout the whole tube (i.e. $p_i\left(d_P\right) = p_0$, assuming no particle breakup inside the tube), a significantly higher air temperature is predicted at the nozzle inlet (i.e. x/L = 1) compared to those results in which changes in the particle size distribution due to breakup inside the tube are considered (i.e. $p_i\left(d_P\right)$ =Eqn. (A.29)). In the third case shown the final particle size distribution, which is measured at the outlet of the nozzle with the HSC experiment, is used directly at the particle injection position ($p_i\left(d_P\right) = p_{end}$, again assuming no particle breakup inside the tube). This total neglect of the particle disintegration process inside the tube leads to an earlier cool down of air temperature compared to both the other scenarios. However, it results in the same nozzle inlet temperature as estimated with the linear breakup assumption. A further parametrization of the initial particle size distribution p_0, assuming one large particle size class at the injection position of the particles, does not affect the temperature prediction significantly (trend comparable to the red one in Fig. A.12, not shown).

Because the particle size distributions at the inlet and at the outlet of the tube can be measured, the linear breakup assumption is used in the final temperature estimation. For this reason the approach shown in Fig. 4.18 in conjunction with Eqn. (A.29) is assumed to be a good estimate for temperature predictions of fully laden dry-ice flows in nozzles #1 and #2. Results from final estimations for both nozzles are shown in Fig.A.12, right.

A.7 Details of the study for the new drag-coefficient

Re-engineering procedure

The re-engineering procedure of drag coefficients is done using Eqn. (2.64), (2.66) and (2.70) in the following formulation:

$$c_D\left(x\right) = \frac{m_P \cdot \frac{\partial^2 \mathbf{x}_P}{\partial t^2} + \frac{\partial p}{\partial \mathbf{x}} \cdot \frac{m_P}{\rho_P}}{\frac{1}{2} \cdot \frac{\pi}{4} \cdot d_P^2 \cdot \rho_f \cdot \left|\mathbf{v}_P - \mathbf{u}\right| \cdot \left(\mathbf{v}_P - \mathbf{u}\right)} \tag{A.30}$$

accounting for experimental particle acceleration data and flow pressure- and velocity-field data from steady state numerical simulations. Figure A.13 presents re-engineered drag coefficients for all POM particle sizes and both high pressure settings investigated (i.e. 4 bar, left hand display and 6 bar, right-hand display) and compares this data to drag coefficients calculated by means of the Schiller-Naumann formulation (S-N-Corr) according to Eqn. (2.68).

In the convergent part of the nozzles the re-engineered drag coefficients are significantly higher than the values predicted by the default correlation. The

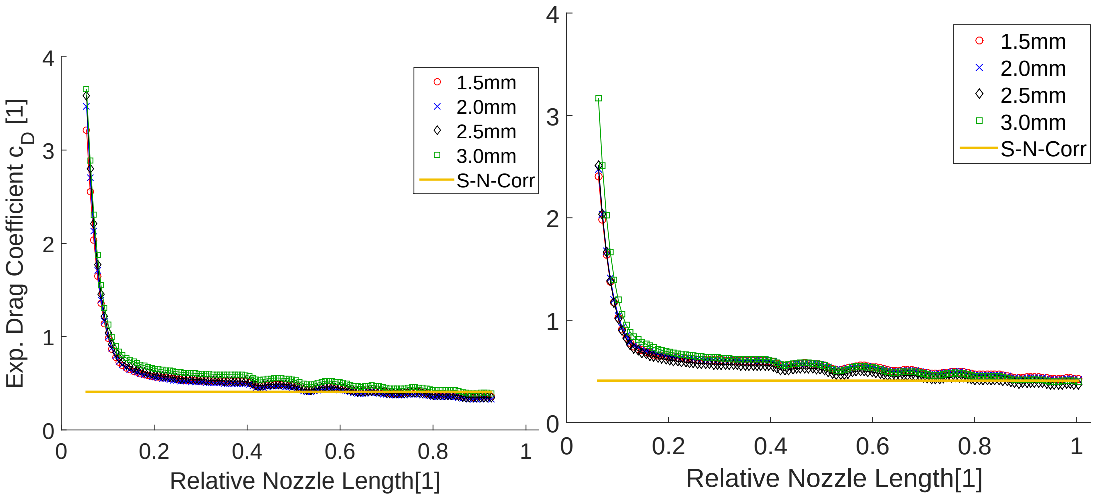

Figure A.13.: Experimental drag coefficients for model particles in transparent validation nozzle, 4 bar (left) and 6 bar (right).

differences encountered become negligible at a relative nozzle length of $x/L \approx 0.5$. The effects discussed above dealing with high forebody and low afterbody pressure as well as strong flow acceleration around particles are assumed to be active especially in the convergent nozzle parts (the nozzle throat is located at a relative nozzle length of $x/L \approx 0.12$) . A mean value comparison of the drag coefficients from Fig. A.13 reveals comparable deviations of experimental from correlated numbers for both pressure cases investigated

$$\frac{\int\limits_0^1 c_D^{\{exp\}}(x)\,dx}{\int\limits_0^1 c_D^{\{S-N\}}(x)\,dx} = 1.3638|_{6\,bar} \ldots 1.2926|_{4\,bar} \approx 1.33. \tag{A.31}$$

Correlation coefficients for the new drag-formulation

The new drag-coefficient formulation as a function of flow Mach number is derived and discussed in Section 4.5.2 and the correlation coefficients for this new formulation, Eqn (4.5), and both cases presented (i.e, 4 bar and 6 bar nozzle pressure) are summarized in Tab. A.5.

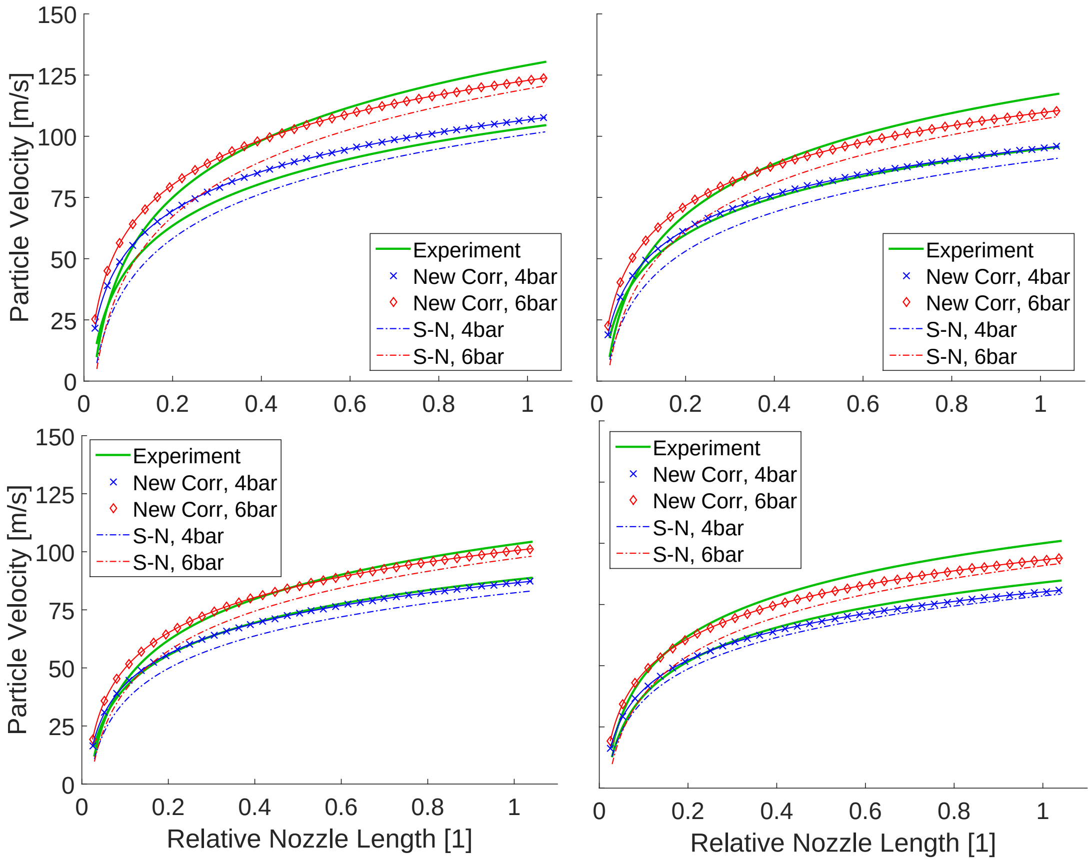

Figure A.14.: Results from repeated numerical simulations with modified empirical drag coefficient in comparison to old results and experimental data inside the nozzle operating at various pressure levels; particle size ranges from 1.5 mm POM particles (upper left display) to 3.0 mm POM particles (lower right display).

Case	K_1	K_0
4 bar	1.5550	1.496
6 bar	1.5898	1.370
mean	1.5724	1.433

Table A.5.: Correlation coefficients for new empirical drag coefficient formulation, Eqn (4.5).

With the modification presented above and in Section 4.5.2 all non-satisfactory simulations were repeated, leading to new results presented, amongst others, in Fig. A.14 (see previous page). The old predictions and experimental trends are compared to the new predictions. The trends shown comprise all POM particles sizes considered and those range from 1.5 mm (uppermost left-hand display) to 3.0 mm (lowermost right-hand display) . The particle velocities are plotted as functions of the nozzle length for 4 bar and 6 bar nozzle pressure.

A significant improvement of the predictions is achieved in all cases considered and the deviations of the mean particle velocities predicted at the nozzle outlet (i.e. at the relative nozzle length = 1) are minimized. However, the success of the improvement turns out to be particle size and nozzle pressure dependent because the deviations achieved with the new correlation increase with increasing operating pressure and particle size.

B Appendix to Chapter 5: Particle breakup modelling

B.1 Details of the sensitivity analysis

In order to simplify the describing set of equations for dry-ice breakup modelling, single contributors to the basic energy balance, Eqn. (5.1), are tested in terms of sensitivity to the application case. A range of dimensionless variables (energy quotients) Υ is derived for this purpose. Using these, the impact of all possible energy contributors is related to primary particle kinetic energy. If this proportion is is low enough (i.e. the limit is decided to be 10 %), the energetic contribution is neglected in the simulation procedure. Vector indications are neglected in what follows.

First, the kinetic energy is tested towards negligibility of the rotational component with

$$\Upsilon_{kin} = \frac{E_{rot}}{E_{trans}} = \frac{\frac{1}{2} \cdot \theta_i \cdot \omega_i^2}{\frac{1}{2} \cdot m_i \cdot v_i^2} = \frac{\frac{2}{5} \cdot m_i \cdot \frac{d_i^2}{4} \cdot \omega_i^2}{m_i \cdot v_i^2} = \frac{1}{10} \cdot \frac{d_i^2 \cdot \omega_i^2}{v_i^2} \tag{B.1}$$

and the critical case is a large secondary particle with a low translational velocity component. According to the HSC results from Section 4.3, the largest possible particle diameter is assumed to be $d_i = 1000\,\mu m$ and the velocity range taken into account is $v_i = 2.5 \ldots 20\,m/s$. By means of varying the rotational frequency, ω, Fig. B.1, left, is created. In case of the lowest velocity considered (i.e. $2.5\,m/s$), the model particle must rotate with a frequency of approximately $2,000\,s^{-1}$ to represent at least 5 % of the particles kinetic energy. For the highest translational velocity in the example there is a frequency of $20,000\,s^{-1}$ necessary to reach the critical value defined above. Rotation of secondary particles cannot be ruled out in general, but expecting higher translational velocities and lower particle sizes in the application case compared to what is considered in the model calculation from Eqn. (B.1), rotational components of energy are decided to be negligible in what follows.

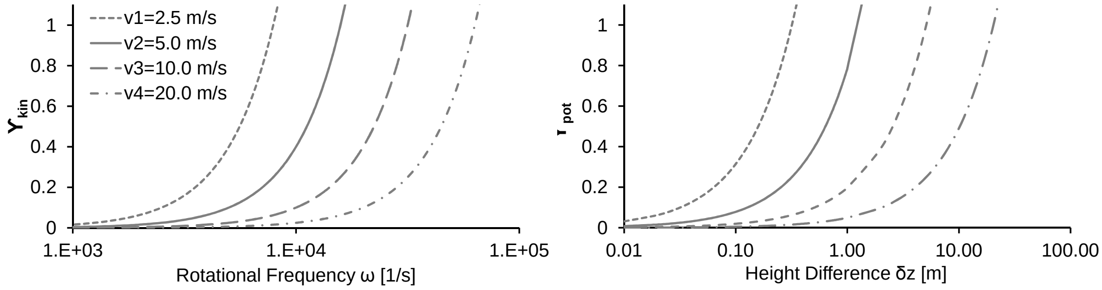

Figure B.1.: Rotational energy contribution (left) and potential energy contribution (right) related to translational kinetic energy for a range of critical variable values.

Next, the potential energy difference is related to kinetic energy (already neglecting rotation):

$$\Upsilon_{pot} = \frac{\Delta E_{pot}}{E_{kin}} = \frac{m_i \cdot \Delta z_i \cdot g}{\frac{1}{2} \cdot m_i \cdot v_i^2} = 2 \cdot \frac{\Delta z_i \cdot g}{v_i^2}. \tag{B.2}$$

The variable value considered in this equation is the critical height difference Δz. Gravity is treated as a constant, $g = 9.81\,\frac{m}{s^2}$, and particle velocity is parametrized in the same range as above. Figure B.1, right, shows the results for Υ_{pot} for a range of height differences.

It is visible, that for very slow particles (here $2.5\,\frac{m}{s}$) a height difference of approximately $3\,cm$ meets the above critical value of 10 %. The faster the particles are, the less important a potential height difference becomes. Keeping in mind that the final particle breakup model is designed to be used in numerical simulations and the balancing procedure is only executed in a very small control volume next to the wall, potential energy contribution to Eqn. (5.1) is decided to be negligible in what follows.

Conventional dry-ice pellets are assumed to be used at sublimation temperature, so there is no sensible heating to be considered. However, a theoretical relation of thermal energy to kinetic energy

$$\Upsilon_{th} = \frac{\Delta E_{th}}{E_{kin}} = \frac{m_i \cdot c_p \cdot \Delta T_i}{\frac{1}{2} \cdot m_i \cdot v_i^2} = 2 \cdot \frac{c_p \cdot \Delta T_i}{v_i^2} \tag{B.3}$$

is shown in Fig. B.2, left. The specific heat capacity of dry-ice is assumed to be $780 J/(kg \cdot K)$ following REDEKER [156]. It can be seen, that if the problem was not assumed to be isothermal, even small temperature differences would have a high impact upon the overall energy balance for low particle velocities. However, hence there are only slight temperature differences expected, if any, thermal energy contributions are deemed to be negligible in Eqn. (5.1). But in cases where the model is used for significantly subcooled dry-ice particles, thermal energy contributors might be considered.

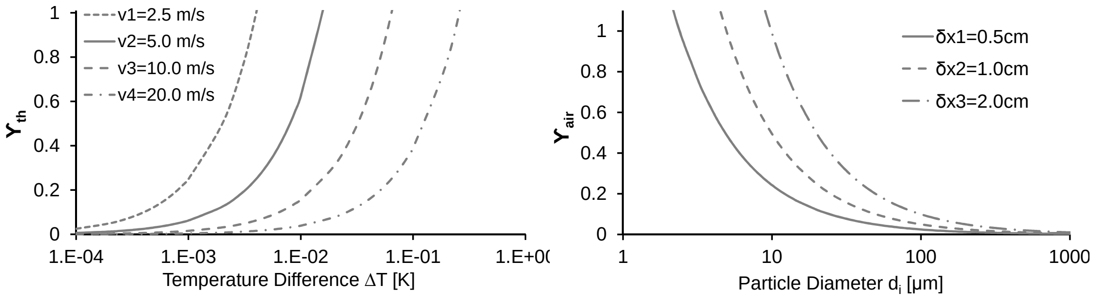

Figure B.2.: Thermal energy contribution (left) and air work energy contribution (right) related to kinetic energy for a range of critical variable values.

The work of aerodynamic forces on particles crossing the control volume of still air is considered

$$\Upsilon_{air} = \frac{E_{air}}{E_{kin}} = \frac{\left| c_D \cdot \frac{\rho_{air}}{2} \cdot v_i^2 \cdot A_{proj} \cdot \delta x_i \right|}{\frac{1}{2} \cdot m_i \cdot v_i^2} = \frac{3}{2} \cdot \frac{c_D \cdot \rho_{air} \cdot \delta x_i}{d_i \cdot \rho_P} \tag{B.4}$$

assuming the particle drag coefficient to be constant $c_D = 0.44$, the particle density too be $\rho_P = 1,560\,kg/m^3$ and an air density of $\rho_{air} = 1.169\,kg/m^3$ at standard ambient conditions. The flight distance between particle and wall is parametrized in the range of$\delta x = 0.5 \ldots 2.0\,cm$ and the particle diameters are varied. Figure B.2, right, shows trends of Υ_{air}.

For very small particle sizes of $20\,\mu m$, which is assumed to be the smallest dispersed particle contributing to erosion in this study (details can be found in Section 5.4.1), significant proportions of aerodynamic work energy up to 50 % can be seen, depending on the distance δx considered. In numerical simulations, when the last cell in front of the wall is considered as the control volume for the energy balance of the particle breakup such as shown in Fig. 5.1 (i.e. $\delta x \rightarrow 0$), aerodynamic work is negligible. However, in cases where the model should be used for rough discretized problem areas (i.e. an a priori calculation with $\delta x \gg 0$) aerodynamic work contributors must be considered.

Breakup energy contribution is left in this place and it is discussed in detail in what is presented below, as a model for internal bond energy of dry-ice must be introduced before discussing its contribution to the overall energy balance.

Next, sublimation energy required to sublimate a certain proportion of primary particle mass is discussed

$$\Upsilon_{sub} = \frac{E_{sub}}{E_{kin}} = \frac{\delta m_{pc} \cdot \delta h_{pc}}{\sum\limits_{i=1}^{n} \frac{1}{2} \cdot m_i \cdot v_i^2} = \frac{\epsilon_{sub} \cdot m_P \cdot \delta h_{pc}}{\frac{1}{2} \cdot \left(1 - \epsilon_{sub}\right) \cdot m_P \cdot \overline{v_i}^2} = 2 \cdot \frac{\epsilon_{sub} \cdot \delta h_{pc}}{\left(1 - \epsilon_{sub}\right) \cdot \overline{v_i}^2} \tag{B.5}$$

and ϵ_{sub} represents this proportion of mass and it is parametrized in the range from 0.05 to 0.0005 %. The heat of fusion of dry-ice is assumed to be $\delta h_{pc} = 573,020\,J/kg$ following KRIEG [103].

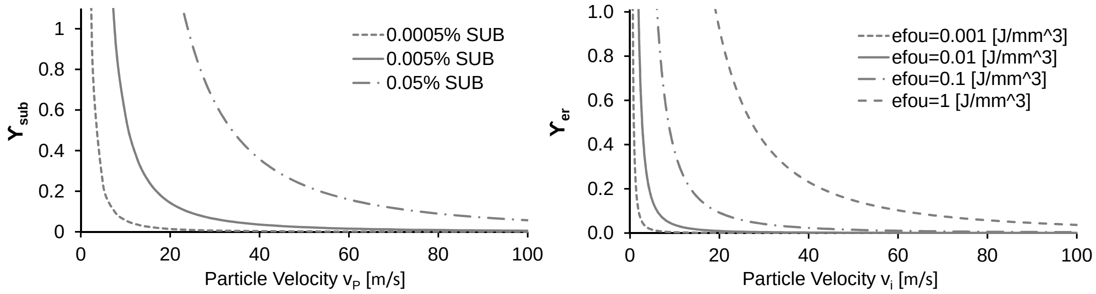

Figure B.3.: Sublimation energy contribution (left) and erosion energy contribution (right) related to kinetic energy for a range of critical variable values.

The particle velocity is variable and Fig. B.3, left, shows the outcomes. Sublimation energy is highly dependent on the sublimated proportion of primary particle mass. If a particle impact at $40\,m/s$ and only a sublimation of 0.05 % is considered approximately 35 % of kinetic energy would be consumed for sublimation, which is a not negligible value. Therefore sublimation energy is determined to be not negligible in Eqn. (5.1).

Next, the energy consumed for defouling erosion is related to kinetic energy as follows:

$$\Upsilon_{er} = \frac{E_{er}}{E_{kin}} = \frac{\delta m_{fou} \cdot e_{fou}}{\sum\limits_{i=1}^{n} \frac{1}{2} \cdot m_i \cdot v_i^2} = \frac{\delta m_{fou} \cdot \frac{1}{\rho_{fou}} \cdot e_{fou}}{\frac{1}{2} \cdot m_P \cdot \overline{v_i}^2} = 2 \cdot \frac{\delta V_{fou} \cdot e_{fou}}{m_P \cdot \overline{v_i}^2}. \tag{B.6}$$

Mean sized particles (i.e. $d_P = 250\,\mu m$) are assumed to impact fouled surfaces at various impact velocities. The fouling layer thickness is assumed to be $\delta_{fou} = 20\,\mu m$ (related to preliminary fouling layer investigations, details can be found in Section 6.3) and the indentation diameter is assumed to be $d_{IMP} = 100\,\mu m$. The fouling energy is parametrized in the range from 0.001 to $0.1\,J/mm^3$. These values are estimated following KLEIS and KULU [102], who reported a range of specific erosion energies for crystalline materials. It is assumed that appropriate values for fouling layers are lower than these and this topic is addressed in Chapter 6.

It can be seen from Fig. B.3, right, that the energy contribution of defouling depends on the fouling specific energy and on the particles impact velocity. In the case of $e_{fou} = 0.1\,J/mm^3$ defouling consumes only a negligible proportion of kinetic energy at particle impact velocity of $40\,m/s$. Increasing this fouling energy value by one order of magnitude leads to an proportional increase of the energy consumed, which turns out to be approximately 25 % in this example. Hence the proportion of defouling energy is only negligible if the fouling specific energy is low enough and it is dependent on the particle impact velocity and size. Therefore it must be generally considered in Eqn. (5.1). Determination of fouling specific energies considering typical foulants from aircraft defouling is a separate topic of this work and it is addressed in Chapter 6.

The amount of breakup energy for the breakup of one single secondary particle from an impinging primary particle can be expressed utilizing the internal bond energy of dry-ice particles. It is theoretically derived in Section B.2 in the Appendix. Inserting this model, Eqn. (B.18) and (B.23), into Eqn. (5.8) leads to the formulation of the breakup energy:

$$E_{i,bu} = 100 \cdot \frac{k_B \cdot T_{pc}}{r_0^2 \cdot \pi^2} \cdot C_{A,bu} \cdot d_i^2 = \gamma^{\{0\}} \cdot C_{A,bu} \cdot d_i^2. \tag{B.7}$$

Application of the above theory to estimate the energetic contribution of the breakup energy to the overall energy balance, Eqn. (5.1), leads to the describing dimensionless variable:

$$\Upsilon_{bu} = \frac{E_{bu}}{E_{kin}} = \frac{\sum_{i=1}^{n} \gamma^{\{0\}} \cdot A_i^{\{0\}}}{\sum_{i=1}^{n} \frac{1}{2} \cdot m_i \cdot v_i^2} = \frac{\gamma^{\{0\}} \cdot C_{A,bu} \cdot \overline{d}_i^2}{\frac{1}{2} \cdot \rho_P \cdot \frac{\pi}{6} \cdot \overline{d}_i^3 \cdot \overline{v}_i^2} = 12 \cdot \frac{\gamma^{\{0\}} \cdot C_{A,bu}}{\pi \cdot \rho_P \cdot \overline{d}_i \cdot \overline{v}_i^2} \tag{B.8}$$

and Υ_{bu} is discussed in Fig. B.4 with the model constants $\gamma^{\{0\}} = 0.095\,J/m^2$ and $C_{A,bu} = 0.242$ (assuming a manufacturing pressure of $p_{man} = 100\,bar$ for the dry-ice). Furthermore, the above ideal dry-ice density and a primary particle diameter of $d_P = 1000\,\mu m$ are assumed.

The mean secondary particle diameter $\bar{d}_i$ is varied in the range from $25\,\mu m$ to $100\,\mu m$ (i.e. producing 64,000 to 1,000 secondary particles assuming a void

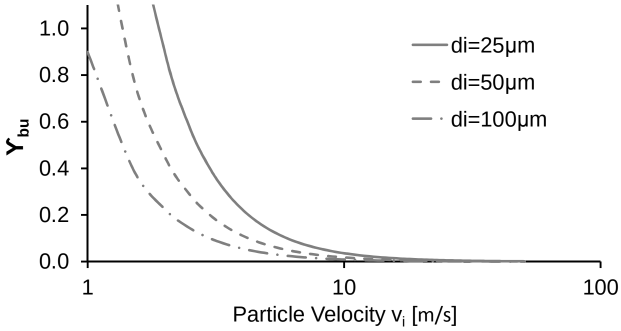

Figure B.4.: Breakup energy contribution related to the translational kinetic energy for a range of critical variable values.

fraction of 0) and the particle velocity is also varied. The velocity is valid for primary as well as for secondary particles, because the mass balance is assumed to be unity for this calculation (i.e. the total primary particle mass is transferred to the secondary particles).

Figure B.4 shows that the breakup energy is not negligible at low particle velocities (i.e. $v_i = 1...10\,m/s$) , which is confirmed for example in [192]. However, it turns out to be negligible for higher particle velocities (i.e. $v_i > 10\,m/s$), even if a large number of very small secondary particles is released on impact.

A summary of the sensitivity analysis to the basic energy balance, Eqn. (5.1), discussed above is given in Tab. B.1. The column-wise listing contains descriptions of the coefficients used, equations of the coefficients, critical variables used, maximum error estimates (i.e. based on the application case) and the final decision whether the energy contributor is negligible or not.

Referencing the above sensitivity analysis and resulting parameter study, it is concluded that from the original energy formulation, Eqn. (5.1), potential, thermal and aerodynamic work contributions can be neglected in the description of the impact process addressed here. Dissipative energy is assumed to be contained in the amount of breakup energy and it is therefore also neglected. The final simplified energy balance is written as follows:

$$E_{P,kin} = \sum_{i=1}^{n} \left(E_{i,kin} + E_{i,bu}\right) + E_{sub} + E_{er} \tag{B.9}$$

Energy Proportion	Coefficient	Critical Variables	Max. Error Estimate	Neglection
Rotational	$\Upsilon_{kin} = \frac{E_{rot}}{E_{trans}} = \frac{2}{5} \cdot \frac{r_i^2 \cdot \omega_i^2}{v_i^2}$	$r_i = 1000\,\mu m$ $\omega_i = 2000\,s^{-1}$ $v_i = 2.5\,m/s$	6.5 %	YES
Potential	$\Upsilon_{pot} = \frac{\Delta E_{pot}}{E_{kin}} = 2 \cdot \frac{\triangle z_i \cdot \vec{g}}{v_i^2}$	$\triangle z_i = 2\,cm$ $v_i = 2.5\,m/s$	6.3 %	YES
Sens. Heat	$\Upsilon_{th} = \frac{\Delta E_{th}}{E_{kin}} = 2 \cdot \frac{c_p \cdot \triangle T_i}{v_i^2}$	$\triangle T_i = 10^{-4}\,K$ $v_i = 2.5\,m/s$	2.5 %	YES
Air Work	$\Upsilon_{air} = \frac{E_{air}}{E_{kin}} = \frac{3}{2} \cdot \frac{c_d \cdot \rho_{air} \cdot \delta x_i}{d_i \cdot \rho_P}$	$\delta x_i = 2\,cm$ $d_i = 50\,\mu m$	20.8 %	...depends
Breakup	$\Upsilon_{bu} = \frac{E_{bu}}{E_{kin}} = 12 \cdot \frac{\gamma^{\{0\}} \cdot C_{A,bu}}{\pi \cdot \rho_P \cdot \bar{d}_i \cdot \bar{v}_i^2}$	$\bar{d}_i = 50\,\mu m$ $\bar{v}_i = 2.5\,m/s$ $(n_P = 8000)$	28.7 %	NO
Lat. Heat	$\Upsilon_{sub} = \frac{E_{sub}}{E_{kin}} = 2 \cdot \frac{\epsilon_{sub} \cdot \delta h_{pc}}{(1-\epsilon_{sub}) \cdot \overline{v_i}^2}$	$\epsilon_{sub} = 0.0005\%$ $\bar{v}_i = 2.5\,m/s$	91.7 %	NO
Erosion	$\Upsilon_{er} = \frac{E_{er}}{E_{kin}} = 2 \cdot \frac{\delta V_{fou} \cdot e_{fou}}{m_P \cdot \overline{v_i}^2}$	$V_{fou} = \frac{\pi}{4} \cdot (100\mu m)^2 \cdot 20\mu m$ $e_{fou} = 0.01\,J/mm^3$ $m_P = \frac{\pi}{6} \cdot (250\mu m)^3 \cdot \rho_P$ $\bar{v}_i = 2.5\,m/s$	59.1 %	...depends

Table B.1.: Summary of the sensitivity analysis to the basic model assumption.

B.2 Derivation of internal bond energy for dry-ice

To account for the particle breakup energy, a model assumption for internal bond energy of the dry-ice particles must be derived. Basically following the derivation by FOELL [57] and comparing it to publication from ASHBY and JONES [13] and this from FILSER and GAUCKLER [55], it is assumed that internal bond energy of a crystalline particle is a function of its Young's modulus Y and a characteristic length $d^{\star}$

$$\gamma^{\{0\}} = \frac{Y \cdot d^{\star}}{\pi^2}. \tag{B.10}$$

The only publication known to the author dealing with values for the Young's modulus of CO_2 dry-ice is this from REDEKER [156]. He performed compression tests with large artificial dry-ice specimen ($d_P = 30\,mm$) and reported a mean value of $Y_{CO2} \approx 0.23 \pm 0.07\,GPa$ from a total number of 12 tests.

This study, in contrast, presents a theoretical approach to the Young's modulus of dry-ice. It is based on macromolecular potential theory. Generally following the above publications [13, 55, 57], the Young's modulus, which is defined as derivative of stress σ with respect to strain ε, can be rewritten dependent on the energetic potential function $\Psi(r)$and on the molecular radius of a molecule at rest r_0:

$$Y = \frac{d\sigma}{d\varepsilon} \rightarrow \frac{d\sigma}{dr} \cdot \frac{dr}{d\varepsilon} \rightarrow \frac{1}{r_0} \cdot \frac{d^2\Psi(r)}{dr^2}. \tag{B.11}$$

Assuming stress to be the quotient of force F to area A

$$\sigma = \frac{F}{A} \approx \frac{F(r)}{r_0^2} = \frac{1}{r_0^2} \cdot \frac{d\Psi(r)}{dr} \rightarrow \frac{d\sigma}{dr} = \frac{1}{r_0^2} \cdot \frac{d^2\Psi(r)}{dr^2} \tag{B.12}$$

and strain to be the displacement of molecules from their position at rest (i.e. from the molecular distance r_0):

$$\varepsilon = \frac{r - r_0}{r_0} \rightarrow \frac{d\varepsilon}{dr} = \frac{1}{r_0}, \tag{B.13}$$

the energetic potential function can be expressed by means of the general equation

$$\Psi(r) = -\frac{A}{r^n} + \frac{B}{r^m} \tag{B.14}$$

taking into account that the potentials derivative at the molecules position at rest, r_0, must be zero

$$\frac{d\Psi}{dr}|_{r_0} = 0. \tag{B.15}$$

Its value $\Psi\left(r_0\right)$ at this position can be approximated by setting it equal to the energy necessary to melt all inner bonds [57]. Application of the Boltzmann constant k_B and assuming the particle to be at phase-change temperature T_{pc} leads to

$$\Psi\left(r_0\right) = \Psi_0 \approx k_B \cdot T_{pc}. \tag{B.16}$$

The Young's modulus can be rewritten by means of Eqn. (B.14) to (B.16):

$$Y \approx \frac{(m \cdot n) \cdot k_B \cdot T_{pc}}{r_0^3}. \tag{B.17}$$

In [57, 216] it was shown, that the product of the model exponents from Eqn (B.14) in Eqn. (B.17) can be approximated by $(n \cdot m) \approx 80$ for numerous crystalline materials including water-ice. The molecular ionic radius of CO_2 dry-ice is assumed to be $r_0 \approx 536\,pm$ following [43].

The Young's modulus is then calculated for dry-ice by means of Eqn. (B.17) and the result is 1.395 GPa. A comparison of this value (based on the assumption of micromolecular ionic bond behaviour following [29, 43]) with the above experimental value of $Y_{CO2} \approx 0.23 \pm 0.07\,GPa$ obtained by REDKER [156] shows satisfactory conformity. Theoretically derived values for ideal crystalline material were expected to be higher than these values from experimental investigations with large specimen. However, both values are of the same order of magnitude.

A further comparison of the the above derivation has been done for the Young's modulus for water-ice. Values for the latter can be found for example in comprehensive reviews in [113] or more recently reported in [62]. The listed values are in the range from 0.3 to $11.5\,GPa$ [113] and 4.35 to $7.78\,GPa$ [62]. ASHBY and JONES [13] reported a value for the Young's modulus for water-ice of $9.1\,GPa$, which is comparable to the aforementioned.

The calculation of the Young's modulus for water-ice with the above procedure results in $3.4\,GPa$ (with $r_0 \approx 446\,pm$ for water-ice from [43]) and this value lies in the same range as the values reported. Based on these results, the estimation adapted from [29, 55, 57], Eqn. (B.17), is assumed to be valid for the rough estimation of Young's moduli of ice particles and it is used in this work to determine such a value for dry-ice.

According to [55], a valid assumption for the displacement length of crystalline molecules is a strain of 25 % (i.e. $d^\star = 1.25 \cdot r_0$) until the onset of internal bond breakage. With this assumption, a new formulation for the internal bond energy of dry-ice particles can be written from Eqn. (B.10) and (B.17):

$$\gamma^{\{0\}} \approx \frac{80 \cdot k_B \cdot T_{pc}}{r_0^3} \cdot \frac{1.25 \cdot r_0}{\pi^2} = 100 \cdot \frac{k_B \cdot T_{pc}}{r_0^2 \cdot \pi^2}. \tag{B.18}$$

and the application this reveals an internal bond energy estimate of approximately $0.095\,J/m^2$.

The second unknown in Eqn. (5.8) is internal bond area, A_P, and it must also be approximated theoretically to calculate the breakup energy. This is done by applying Hertzian geometrical contact theory, reported for example in [94], to the above molecular ionic bond estimation. The corresponding model assumption for dry-ice is shown in Fig. B.5. A primary particle (here index P, grey) and a secondary particle (here index i, white) can be seen with yellow molecular particles at the surface of the secondary particle.

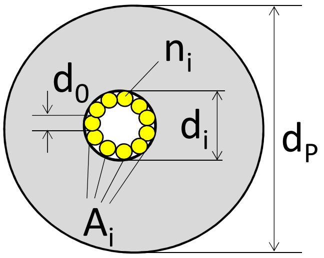

Figure B.5.: Assumption of internal bond area of dry-ice particles based on Hertzian contact theory.

It is assumed, that each of the n_i surface molecules of the secondary particle is in Hertzian contact with a molecular counterpart of the primary particle (not shown in Fig. B.5). Hence, the contact radius a_0 of one such molecular pairing can be calculated according to [94]

$$a_0^2 = \left(1.5 \cdot \left(1 - \nu^2\right) \cdot p_{man} \cdot \pi \cdot r_0^2 \cdot \frac{r_0}{Y}\right)^{\frac{2}{3}} = r_0^2 \cdot \left(1.5 \cdot \left(1 - \nu^2\right) \cdot p_{man} \cdot \frac{\pi}{Y}\right)^{\frac{2}{3}} \quad \text{(B.19)}$$

applying manufacturing pressure of dry-ice particles, p_{man}, and Poissons ratio of dry-ice,ν, which is assumed to be 0.33 in this study (comparable to the water-ice values reported in [113]) . The number of molecules engaged in each bond between the primary particle P and any secondary particle i can be estimated by balancing the available surface of the secondary particle to the projected area of a single molecule (in this case represented by $\frac{\pi}{4} \cdot r_0^2$)

$$n_i = \frac{4 \cdot \Gamma^{\frac{2}{3}} \cdot \pi \cdot r_i^2}{\pi \cdot r_0^2} = 4 \cdot (0.71)^{\frac{2}{3}} \cdot \frac{r_i^2}{r_0^2}. \quad \text{(B.20)}$$

Furthermore, a cubical void fraction for spheres $\Gamma = 0.71$ (reported for dry-ice in [43]) is considered and it is recalculated to a 2D information. The whole contact area describing the bond between any secondary particle i and the primary particle P can be calculated with Eqn. (B.19) and (B.20):

$$A_i = \pi \cdot a_i^2 = \pi \cdot n_i \cdot a_0^2 = \pi \cdot 4 \cdot (0.71)^{\frac{2}{3}} \cdot \frac{r_i^2}{r_0^2} \cdot r_0^2 \cdot \left(1.5 \cdot \left(1 - \nu^2\right) \cdot p_{man} \cdot \frac{\pi}{Y}\right)^{\frac{2}{3}}. \quad \text{(B.21)}$$

Rearrangement of this formulation by application of the diameter of the secondary particle instead of its radius $r_i^2 = \frac{d_i^2}{4}$ and computation of the constant values from Eqn. (B.21) leads to the final expression estimated for the bond area of dry-ice secondary particles:

$$A_i = \left[\pi^{\frac{5}{3}} \cdot \left(1.065 \cdot \left(1 - \nu^2\right) \cdot \frac{p_{man}}{Y}\right)^{\frac{2}{3}}\right] \cdot d_i^2. \tag{B.22}$$

The term in brackets is a constant which is known a-priori, and Eqn. (B.22) can be simplified by introduction of a breakup constant (i.e. $C_{A,bu}$) to

$$A_i = C_{A,bu} \cdot d_i^2. \tag{B.23}$$

Finally, the breakup energy for the breakup of one single secondary particle from an impinging primary particle can be expressed by inserting Eqn. (B.18) and Eqn. (B.23) into Eqn. (5.8):

$$E_{i,bu} = 100 \cdot \frac{k_B \cdot T_{pc}}{r_0^2 \cdot \pi^2} \cdot C_{A,bu} \cdot d_i^2 = \gamma^{\{0\}} \cdot C_{A,bu} \cdot d_i^2. \tag{B.24}$$

B.3 Model assumption for secondary particle velocities

In order to estimate secondary particle post-impact velocities, an elliptical envelope is assumed to contain these particles and the outer bounds of this ellipse are tracked. This ellipse is described by Eqn. (5.20) which is introduced in Section 5.3.1. The envelope is assumed to be represented by the fastest dispersed particles. However, the initial cloud of dust (see discussion of Fig. 5.7) remains neglected because it disappears form the HSCs field of view directly after impact. The temporal development of the envelope of secondary particles is tracked with both HSC #1 and #2 in relation to the primary particle impact point. This situation is schematically shown in Fig. B.6.

The primary particle impact point (red X) is shown in the left-hand image from side view (HSC #1) and an idealized distribution of secondary particles is indicated by the grey ellipse. The mid-point of this ellipse (yellow dot) is shifted tangentially along the target. The secondary particles envelope velocity in normal direction is v_z^-. The right-hand scheme shows the same situation from bottom view (HSC #2). Here, the ellipsoid of the secondary particles is indicated in dark grey and the velocityv_x^{ell} of its mid-point is related to the primary particles impact point. Furthermore, the velocities along both ellipse axes (here $dir = x, y$) are indicated: $v_{dir}^{+/-}$. With these values, maximum secondary particle velocity (neglecting the cloud of dust) can be estimated.

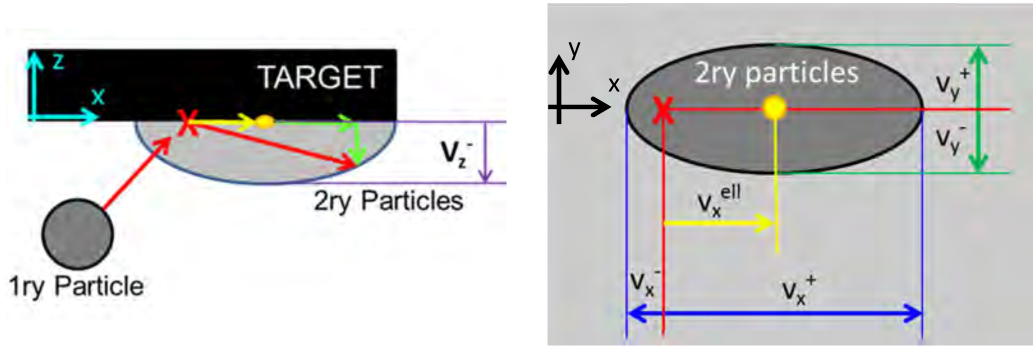

Figure B.6.: Schematic of secondary particles cloud tracking in side view (left) and bottom view (right).

It was experimentally observed that secondary particles are stochastically distributed between the impact point and the envelope of the ellipse. This observation was also reported in various water ice impact studies [69, 143, 158, 200]. Based on this finding, secondary particle velocities are stochastically modelled in the final particle breakup model by means of the elliptical formulation. It is assumed that absolute secondary particle velocities range from zero to maximum envelope velocity (which is derived from experimental data) and that the individual particle velocity vectors are stochastically distributed inside this elliptical envelope.

The theoretical values, all illustrated in Fig. B.6, are related to experimental outcomes as follows:

$$v_x^{\{mx\}} = \frac{v_x^+ + v_x^-}{2} := a \tag{B.25}$$

$$v_y^{\{mx\}} = \frac{v_y^+ + v_y^-}{2} := b \tag{B.26}$$

$$v_z^{\{mx\}} = v_z^- := c \tag{B.27}$$

$$v_x^{ell} := a_{ELL} \tag{B.28}$$

where the right-hand side variables a, b, c and a_{ELL} describe final mean results derived from the experimental recordings.

B.4 Proof of momentum conservation

The new particle breakup model applies a mass- and energy-balance to assure conservation and this is described in Sections 5.2 and 5.4. Momentum conservation is formally achieved by measured secondary particle velocities and by the model assumption that the secondary particle vectors are fitted inside the measured envelope of the cloud of secondary particles (for details see Sections 5.3.1 and B.3).

However, momentum conservation of the model is proved in what follows and it is demonstrated that there can be found a coefficient of restitution lower than 1 (i.e. the momentum residual) for each secondary particle velocity component if the measured secondary velocities and the elliptical distribution procedure described above are applied. To demonstrate this, an additional model assumption is introduced for the breakup situation and this is shown in Fig. B.7.

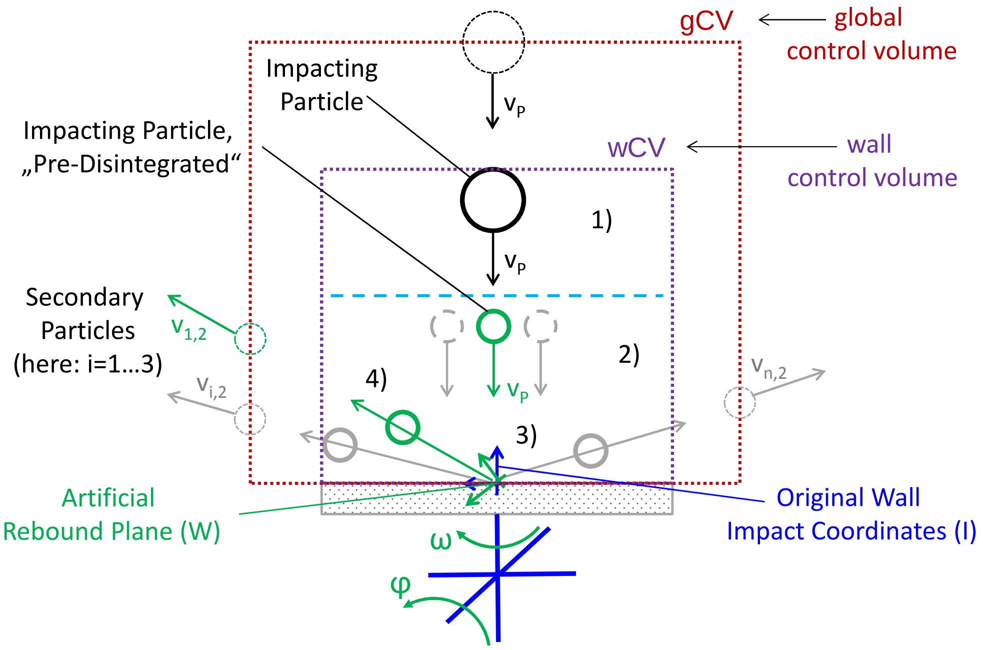

Figure B.7.: Schematic of the model assumption for the proof of momentum conservation of the particle-breakup model.

The breakup process is theoretically split into four steps. First, the impacting particle enters the wall control volume (wCV) and it is pre-disintegrated between steps 1) and 2) into all secondary particles (in this example 3) but it is not yet reflected from the wall. At the interface between steps 1) and 2) the residual of the mass balance (index m)

$$Res^{m}_{wCV} = \frac{\sum_{i=1}^{n} m_{i,2}}{m_P} = \delta m \tag{B.29}$$

these of all momentum balances (index M,dir)

$$Res^{M\{dir\}}_{wCV,P} = \frac{\sum_{i=1}^{n} m_{i,2} \cdot v^{\{dir\}}_{P,I}}{m_P \cdot v^{\{dir\}}_{P,I}} = \delta m \tag{B.30}$$

and this of the energy balance (index e)

$$Res^{e}_{wCV,P} = \frac{\frac{1}{2} \cdot \sum_{i=1}^{n} m_{i,2} \cdot \left\| \mathbf{v}_{P,I} \right\|^2}{\frac{1}{2} \cdot m_P \cdot \left\| \mathbf{v}_{P,I} \right\|^2} = \delta m \tag{B.31}$$

are therefore satisfied by the mass residuum measured δm (i.e. taken from the statistical database underpinning the model). For each of these secondary particles i an artificial particle-wall contact is assumed to take place at the impact point. Furthermore it is assumed that each of these pre-disintegrated secondary particles impinges the wall at the primary particle velocity $v_{P,I}$.

In a real breakup the secondary particles interact with the wall and with each other during the impact process. In the model, however, this interaction is covered by the assignment of secondary particle velocity vectors which are modelled based on experimental data. To prove that the model is momentum conservative it is shown, that for each of these pre-disintegrated secondary particles an artificial rebound plane can be found which is created by an individual rotation of the wall plane around both the tangential and the normal wall axes (here φ and ω) in a way that the coefficients of restitution for all velocity components of the particles are smaller than one.

To achieve this, the particle velocity vectors are transformed from step 2) to step 3) from the original wall coordinate system (index I, blue in Fig. B.7) into a modified, wall-bound coordinate system (index W, green in Fig. B.7) by means of individual rotation matrices $\mathbf{R}$ for the particle velocity before

$$\mathbf{v}_{P,W} = \mathbf{R}\left(\varphi, \omega\right) \cdot \mathbf{v}_{P,I} \tag{B.32}$$

and after impact

$$\mathbf{v}_{i,2,W} = \mathbf{R}\left(\varphi, \omega\right) \cdot \mathbf{v}_{i,2,I}\,. \tag{B.33}$$

These artificially rotated planes theoretically replace the real collision partners of the secondary particles. The idea for this theoretical approach is based on the publications by SOMMERFELD and HUBER [175] who used a rotated plane to predict particle-wall interaction between small particles and rough walls. In such situations the particles interact with the rough texture of the wall even if the wall is globally a plane and therefore the particle velocity vectors are modified after the impact and this modification cannot be described by global coefficients of restitution.

By means of the rotated planes it can be shown that the mass balance

$$Res^{m}_{wCV,i} = \frac{m_{i,2}}{m_{i,2}} = 1 \tag{B.34}$$

the momentum balances

$$Res^{M\{dir\}}_{wCV,i} = \frac{m_{i,2} \cdot v^{\{dir\}}_{i,2,W}}{m_{i,2} \cdot v^{\{dir\}}_{P,W}} = \varepsilon^{\{dir\}}_{i,W} \tag{B.35}$$

and the energy balance

$$Res^{e}_{wCV,i} = \frac{\frac{1}{2} \cdot m_{i,2} \cdot \left\| \mathbf{v}_{i,2,W} \right\|^2}{\frac{1}{2} \cdot m_{i,2} \cdot \left\| \mathbf{v}_{P,W} \right\|^2} = \left\| \mathbf{E}_{i,W} \right\| \tag{B.36}$$

can be satisfied by applying the measured and elliptically fitted secondary particle velocities $\mathbf{v}_{i,2,I}$. Thereby it is always possible to find coefficients of restitution for all velocity components of the particles in the modified, wall-bound coordinate system such as

$$\varepsilon^{\{dir\}}_{i,W} \overset{!}{<} 1 \tag{B.37}$$

and this statement was proved by numerous calculations from which two are presented below.

In the example discussed below the first rotation angle of the artificial rebound plane is chosen artificially and this is done as a function of the particle impact angle α_P

$$\varphi = \left| 90^\circ - \alpha_P \right| + 15^\circ \overset{!}{=} 0 \ldots \frac{\pi}{2} \,. \tag{B.38}$$

The second rotation angle of the rebound plane can then be calculated considering the same boundaries

$$\omega \overset{!}{=} 0 \ldots \frac{\pi}{2} \tag{B.39}$$

and under consideration of the requirement that all coefficients of restitution must be lower than unity. The rotation matrix can be expressed explicitly with these rotation angles

$$\mathbf{R}\left(\varphi,\omega\right) = \mathbf{R}_y\left(\varphi\right) \cdot \mathbf{R}_z\left(\omega\right) \tag{B.40}$$

and it is shown in Fig. B.9 for the example of a single particle impact and rebound presented in Fig. B.8 that there is always a solution which allows to find coefficients of restitution smaller than 1 for all velocity components, depending on the artificial plane selected.

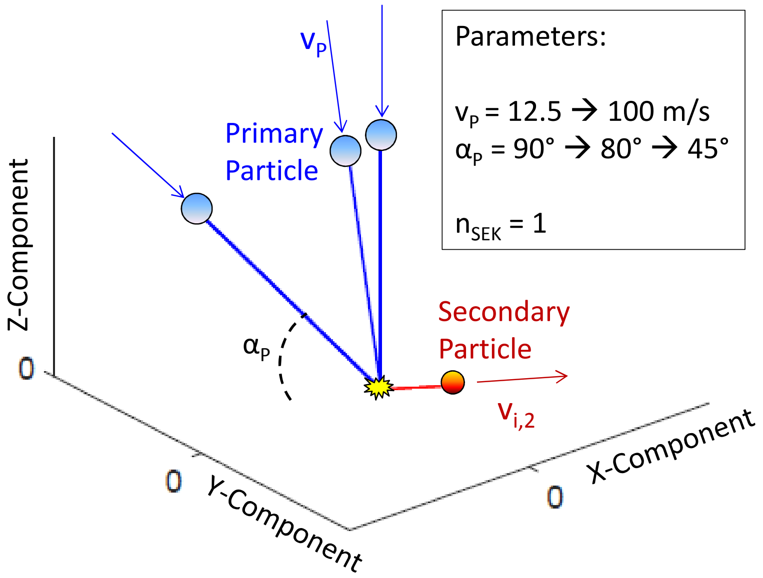

Figure B.8.: Example no. 1: primary particle impingement at various impact velocities and angles produces a single secondary particle.

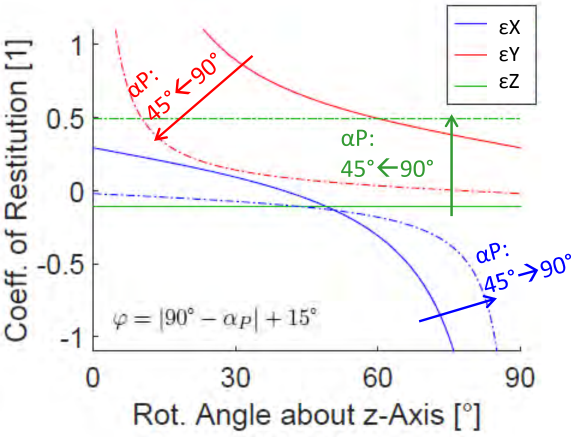

Figure B.9.: Solution of example no. 1 showing the coefficients of restitution linking the primary and the secondary particle velocity vector as a function of the selected artificial plane.

Based on this is demonstrated below that this principle is also applicable to a real situation, in which a primary particle is disintegrated into 4 secondary particles and each of these is redirected into various directions after impact (see Fig. B.10). The results of this calculation are shown in Fig. B.11, where the rectangular (i.e. $\alpha_P = 90°$) and the angular primary particle impact (i.e. $\alpha_P = 45°$) are considered and all residuals of the secondary particles for mass (m), momentum (M,dir) and energy (e) are plotted. Furthermore the calculated second rotation angle ω of the artificial rebound plane is shown whereas the first rotation angle φ is pre-selected as suggested above.

All values presented are lower than 1 and it is therefore concluded that the theory described above holds and that the model is mass-, momentum- and energy-conservative even if it only applies mass- and energy-conservation equations in its numerical formulation. Momentum conservation is achieved by measurement and application of the secondary particle velocities and it is implicitly integrated in the particle breakup model presented.

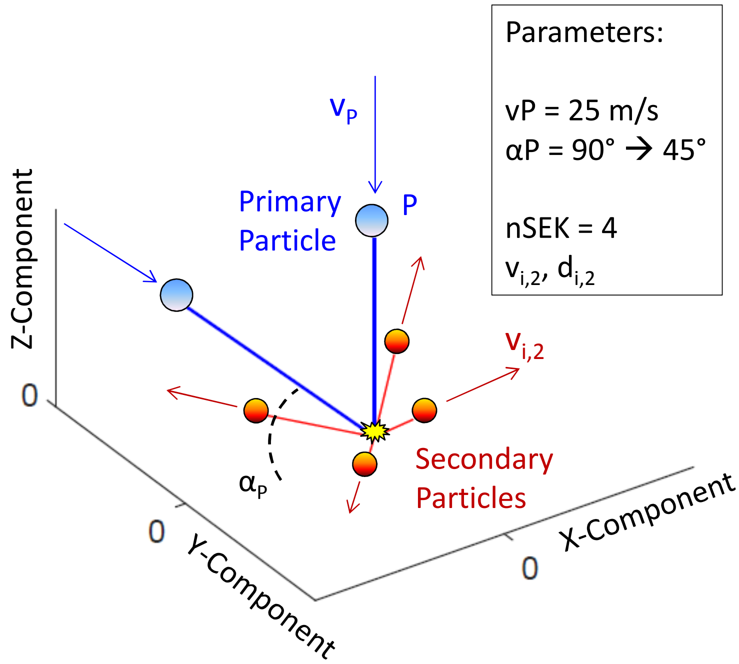

Figure B.10.: Example no. 2: primary particle impingement at two impact angles produces a number of secondary particles.

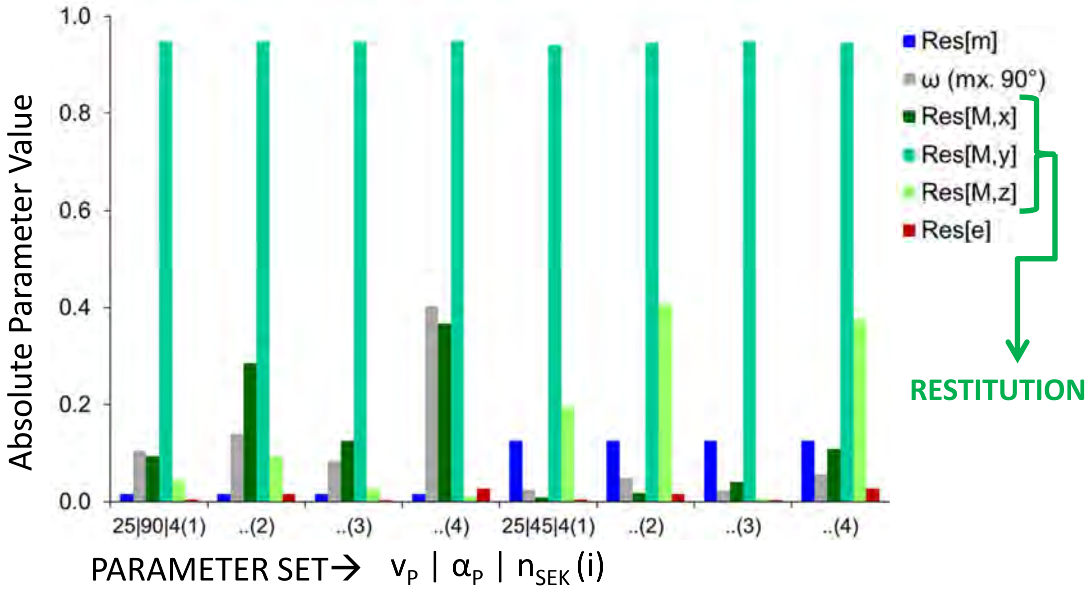

Figure B.11.: Solution of example no. 2 showing numbers lower than 1 for all residuals considered and for all secondary particles.

C Appendix to Chapter 6: Defouling erosion modelling

C.1 Defouling variations for angular impacts

Because angular impacts (i.e. not perpendicular to the wall's surface) produce non-spherical and displaced indentations, an additional formulation must be used to consider this fact in the model. Therefore the elliptical eccentricity of the experimental indentations is measured in the experiment

$$ecc^{\{part,fou,\alpha\}} := \left(\frac{a^2 - b^2}{a^2}\right)^{\left(\frac{1}{2}\right)} \tag{C.1}$$

Shape deviations from ideal spherical indentations and asymmetric displacement of indentations from the impact point are considered by processing this value into the geometric ellipse equation in Cartesian coordinates (described for example in [26]):

$$\left(\frac{x}{a}\right)^2 + \left(\frac{y}{b}\right)^2 = 1 \tag{C.2}$$

and into the formulation of the distance between the centre and each of the two foci of the ellipse (i.e. the focal distance)

$$f = \left(a^2 - b^2\right)^{\left(\frac{1}{2}\right)} \tag{C.3}$$

The geometrical meaning of this procedure to indentation predictions is shown in Fig. C.1. As an example a typical indentation area from an angular impact

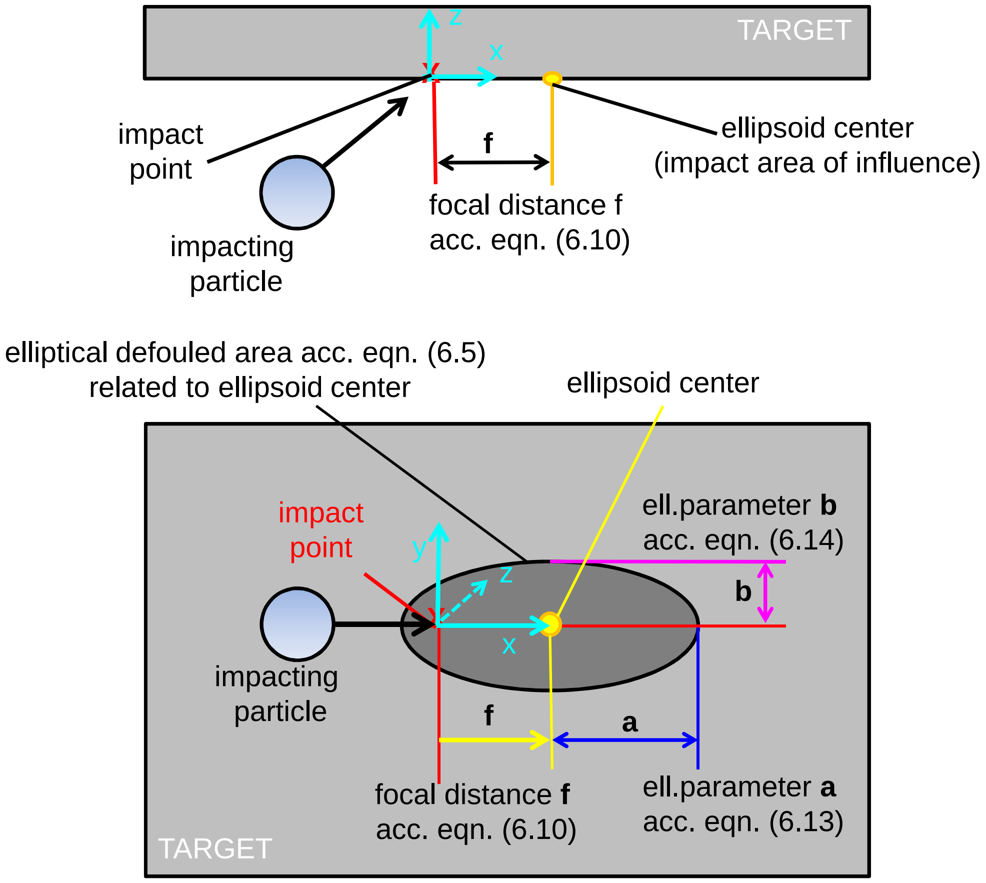

Figure C.1.: Schematic showing the assumptions and terminology used to describe the non-circular defouled area.

is fitted by means of the above variables, assuming the focal distance to be representative for the displacement of the centre of the defouled area.

The parameters to be used in Eqn. (C.2) and (C.3) are derived as follows from experimental data. First, the impact area is used to express the elliptic defouling area

$$A_{IMP}^{\{part,fou,\alpha\}} = \pi \cdot a \cdot b. \tag{C.4}$$

Rearrangement of the elliptical eccentricity formulation, Eqn. (C.1),

$$ecc^{\{part,fou,\alpha\}} = \left(1 - \left(\frac{b}{a}\right)^2\right)^{\left(\frac{1}{2}\right)} \tag{C.5}$$

in conjunction with the above defouling area description leads to two additional equations and these can be used to determine the two additional ellipse variables

$$a = \frac{b}{\left(1 - \left[ecc^{\{part,fou,\alpha\}}\right]^2\right)^{\left(\frac{1}{2}\right)}} \tag{C.6}$$

and

$$b = \frac{A_{IMP}^{\{part,fou,\alpha\}}}{\pi \cdot a}. \tag{C.7}$$

C.2 Details of the review of the restitution concept

The results of a study utilizing POM particles and an artificial coating are presented and these show that the coefficients of restitution are a function of Stokes number and that the diameter of the defouling produced is a function of the particle diameter and of the impact velocity. Spherical and non-spherical particles made from POM reference material of various sizes (i.e. diameters from 1.5 mm to 3.8 mm) and shape (i.e. spherical particles and granules) are used to determine experimental restitution and defouling data. These trends are examined regarding their comparability and the outcomes of this study are shown in Fig. C.2.

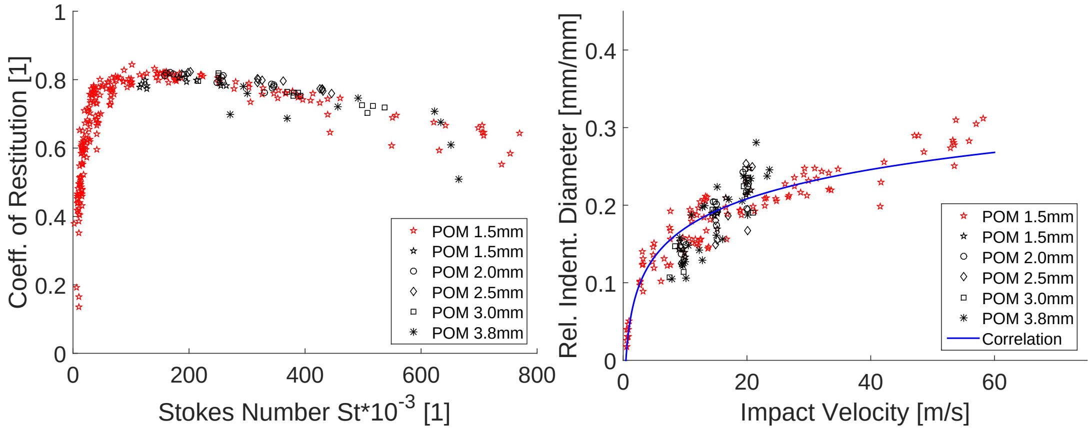

Figure C.2.: Restitution data (left) and defouling data (right) for variously sized and shaped POM particles.

The left-hand display shows comparable coefficients of restitution measured for impacts of particles with various sizes (1.5 to 3.0 mm) and shape (3.8 mm particles are irregularly shaped granules) and this coefficient is expressed as a function of the Stokes number. Even the irregularly shaped particles show restitution data comparable to spherical particles, as long as their rotational speed remains low after impact compared to translational velocity components. The coefficient of restitution could not be accurately determined for particles having high post-impact angular velocity; such particles are not shown in the graph (Fig. C.2, left). Furthermore, the graph contains the whole dataset from the basic experiment with 1.5 mm POM particles.

The above comparability is also valid for indentations caused by these particles upon PTFE coated targets and this is shown in Fig. C.2, right. The corresponding defouling indentation diameter can be described by a logarithmic correlation as a function of particle impact velocity. It must be related to the impacting particles diameter to account for various indentation sizes generated by various primary particle sizes. The correlation presented has a coefficient of determination of $R^2 \approx 0.9$ and the results are found to be independent from particle shape and size.

It must be noted that the author previously postulated [VII] the correlation of indentation diameters as a function of Stokes number. However, this procedure fails when various particle sizes of the same material are considered. The indentation size turned out to be linearly dependent on particle size but not logarithmic.

C.3 Detailed experimental defouling data

In this section all experimental results considered for the determination of the defouling functions are presented.

The results for both original fouling materials defouled with reference material particles at normal impact angles are shown in Fig. C.3 (i.e. ORIG1 defouled with POM, left-hand display, and ORIG2 defouled with stainless-steel, right-hand display). The impact velocity of the stainless-steel particles is recalculated to equivalent dry-ice velocity values by means of Eqn. (6.4).

Figure C.4 shows the defouling data for both original fouling materials defouled with dry-ice particles at normal impact angles (left-hand displays) and at angular impacts (right-hand displays). Both upper displays in Fig. C.4 contain data from ORIG1 defouling tests and these lower displays contain data from ORIG2 defouling.

It must be noted that there was almost no defouling detectable for angular dry-ice impacts upon ORIG1 fouling (Fig. C.4, upper right display). The logarithmic correlation of this dataset is formally not valid but it is decided to accept this uncertainty here to be able to provide a comparable description for all materials considered.

Figure C.5 shows the experimental data and the corresponding logarithmic correlations for PTFE fouling defouled with POM particles (upper displays) and with dry-ice particles (lower displays) at normal impact angle (left displays) and at angular impacts (right displays). The scattering increases if dry-ice is used instead of POM and this effect is discussed in detail in Section 6.3.2. Figure C.6 shows comparable experimental data and the corresponding logarithmic correlations for SALT fouling defouled with the same parameters as the PTFE above.

Some representative figures are given and the trends for the whole range of materials and parameters investigated are discussed in detail in Section C.3.

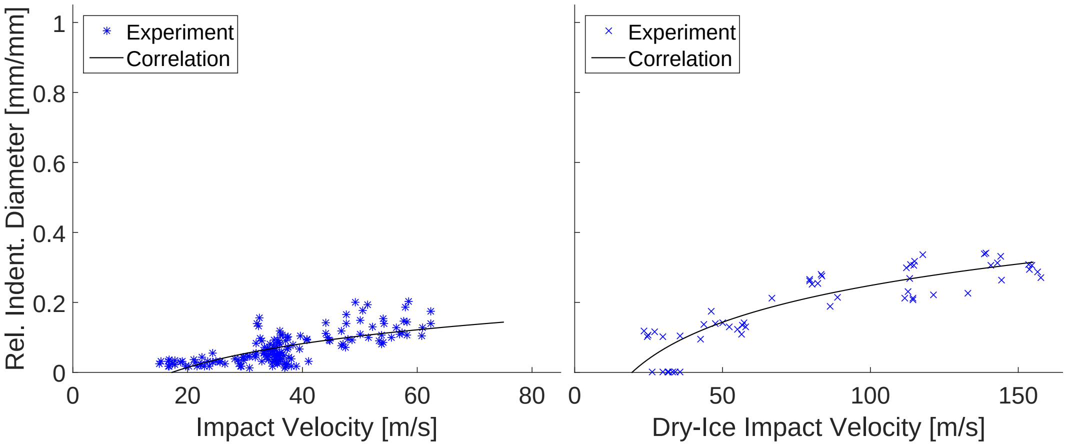

Figure C.3.: ORIG1 defouling with POM particles (left) and ORIG2 defouling with stainless-steel particles (right), both at normal impact angles (i.e. 0°).

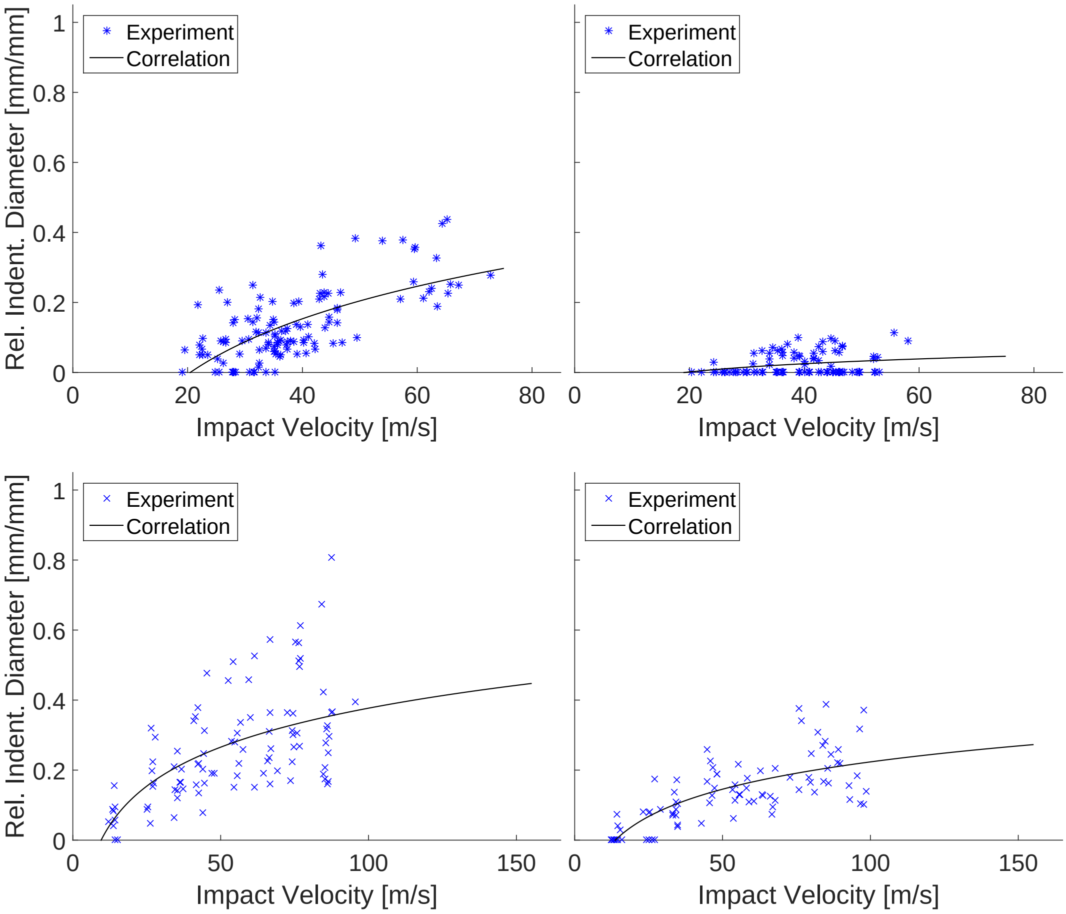

Figure C.4.: Original fouling - normal impact defouling (0°, left displays) and angular impact defouling (60°, right displays) with dry-ice particles upon ORIG1 fouling (upper displays) and upon ORIG2 fouling (lower displays).

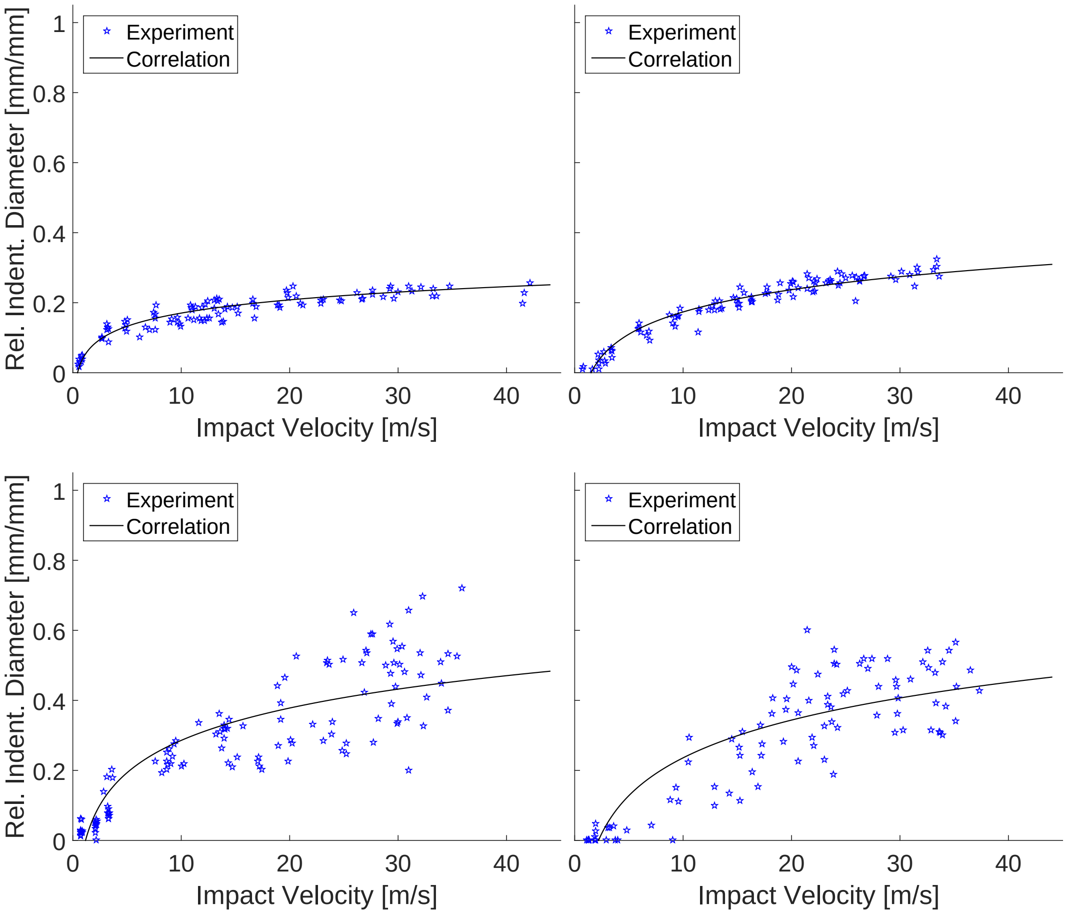

Figure C.5.: PFTE fouling - normal impact defouling (0°, left displays) and angular impact defouling (60°, right displays) with POM particles (upper displays) and with dry-ice particles (lower displays).

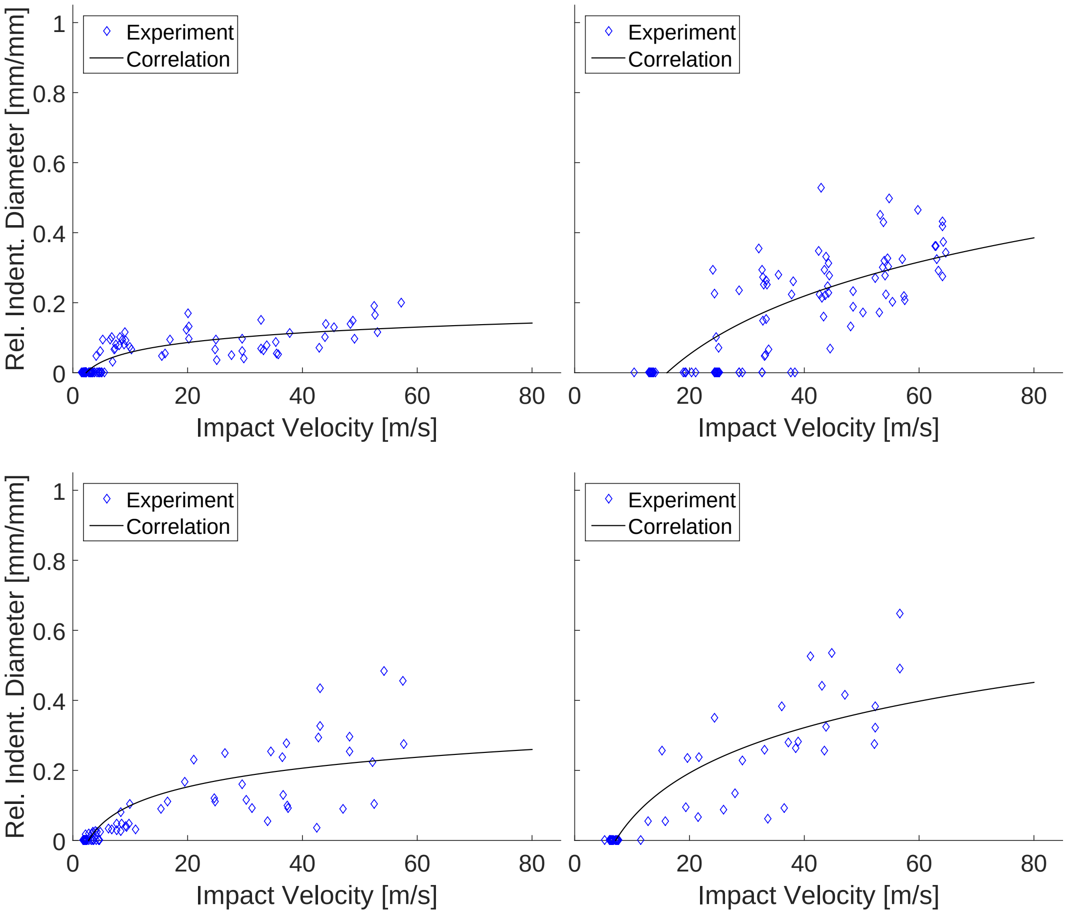

Figure C.6.: SALT fouling - normal impact defouling (0°, left displays) and angular impact defouling (60°, right displays) with POM particles (upper displays) and with dry-ice particles (lower displays).

D Appendix to Chapter 7: Validation case study

D.1 Details of the numerical set-up

Details of the numerical set-up used for the wind-tunnel simulations are given below. The spatial discretization of the relevant numerical volume is made by means of scalable block-meshing technique with respect to sufficient resolution of the boundary layers (a priori estimated first cell: $y+ \leq 1$, at least 30 cells inside of the boundary layer). The Ansys MESHER tool, version 17.2 was utilized and meshing details are presented in Fig. D.1. A preliminary grid-study led to a total problem description consisting of approximately 6,000,000 grid-points. The mesh was refined block-wise and the mostly refined meshing zone is located around the target plate. The O-gird around the plate and the rectangular mesh in the channel are linked with an unstructured buffer-layer meshing, which allows to parametrize the target angle easily without complete re-meshing of the area of interest.

The boundary conditions selected are mass-flux and total temperature at the inlet as well as static pressure and open boundaries at the outlet. The selection of the outlet boundary condition is depending on the target plate angle and this is discussed in more detail in Section 7.2. Furthermore, the particle velocity vector (adapted from experimental measurement) and a predefined injection position (measured in the experiment) are selected as inlet conditions for the dispersed phase. In the case of dry-ice the experimentally derived particle size distribution is applied to the particles.

Ambient pressure and temperature are: $p_{amb} = 101,300\,Pa$ and $T_{amb} = 20.00°C$ for all cases simulated with particles (according to experimental conditions to which the simulations are referred). The most important grid and

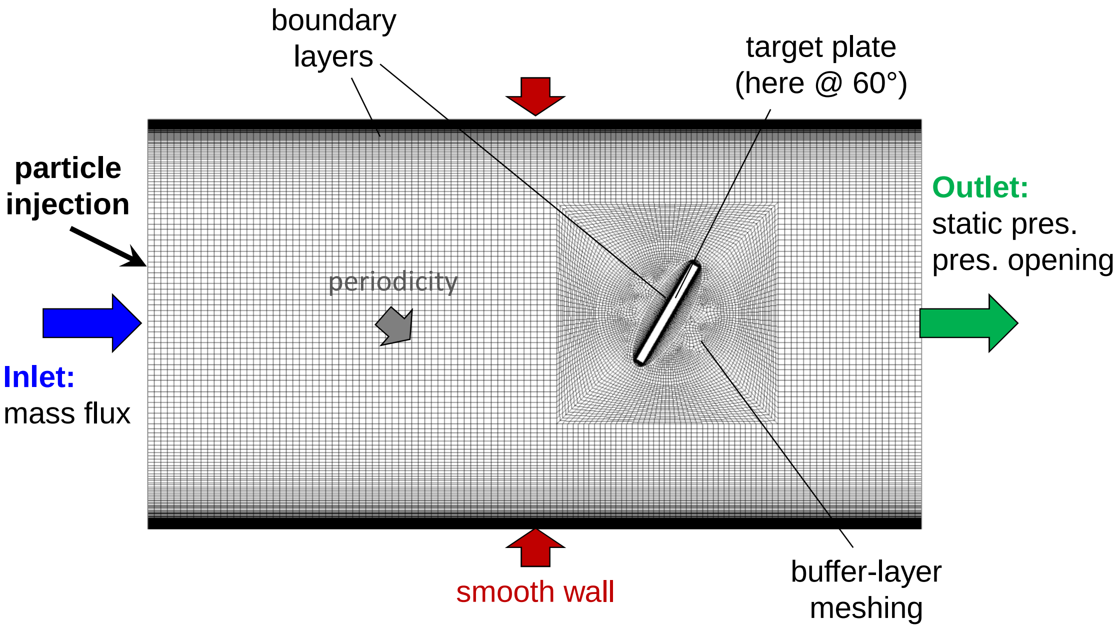

Figure D.1.: Details of a representative stream channel meshing for the wind-tunnel experiment.

set-up information is summarized in Tab. D.1 and Tab. D.2 contains the most important parameters of the cases considered, the corresponding boundary conditions for the simulations and the reference values selected for the discussion of pressure and velocity profiles in Section 7.2 and in Sections D.2 and D.3 in the Appendix below.

GRID	Scalable	Grid study	Critical elem. size $h/D^{\star}$	No. of layers in boundary layer	Total no. of grid points	Boundary layer first cell y+
	yes	yes	0.04	44	6,000,000	1

SET-UP	State	Turbulence	Pseudo Timestepping	Advection Schemes	Turbulence Numerics	Energy equation
step1	steady	$k-\omega-SST$	physical, adaptive	1st order	1st order	isothermal
step2	steady	$k-\omega-SST$	physical, 1e-4 s	Upwind	High-Res	total energy

Table D.1.: Most important grid and set-up information of the wind-tunnel validation case simulations.

Case No	Air Inlet Velocity [m/s]	Target Angle [°]	BC Inlet	BC Outlet	Reference Pressure [Pa]	Reference Velocity [m/s]
1	30	30	mass-flux	Opening, p-constr.	4.1 (in), 203.9 (out)	32.55
2	50	30	mass-flux	Opening, p-constr.	n.a.	n.a.
3	25	60	mass-flux	Static pressure	14.8 (in), 1498.6 (out)	61.47
4	45	60	mass-flux	Static pressure	n.a.	n.a.

Table D.2.: Overview of validation case parameters, applied numerical boundary conditions (BC) and pressure (p_{ref}) and velocity (u_{ref}) reference values used in diagrams below.

D.2 Details of the symmetry assumption study

It is assumed that the behaviour of the validation experiment can be predicted numerically by considering a mid-plane cut through the rectangular part of the experimental set-up assuming periodical symmetry at its sides. This assumption is based on preliminary observations of POM and dry-ice particle tracks. These particles are injected at the mid-channel and they impact the target in all cases considered in the central 33 % of the channel.

In order to show that side wall effects do not significantly influence the mid-plane flow, flow parameters were measured at a grid of locations across three vertical and four horizontal positions across the section at the inlet and outlet. Typical results showing the most significant deviations of the pressure and velocity field measured in the mid plane (i.e. 0 % depth) compared to near side-wall results (i.e. 90 % depth) are shown in Fig. D.2 to D.3 for the cases #1 and #4 and the inlet and outlet planes of the channel.

The most significant deviations are encountered at the outlet-plane (i.e. behind the target plate) and there are almost negligible differences found for comparable measurements at the inlet planes (shown in the upper displays of Fig. D.2 and D.3). Influences of the side walls are clearly visible in the measurements of static pressure nearest to the wall (i.e. 90 % channel depth) in all cases and these influences are also visible in the corresponding velocity data. The differences are more significant for low velocity flows with smaller target angles, such as shown in Fig. D.2, compared to higher velocity flows with steeper target angles, such as shown in Fig. D.3, and this can be attributed to denser streamline formation and the related changes in the pressure and velocity field near the upper wall of the stream channel.

However, the deviations decrease and become negligible for almost all measuerements further away from the wall and based on these results and the above particle tracking observations it was decided to simulate the central 33 % of the channel depth (i.e. a depth of 41 mm) with free-slip conditions at the sides.

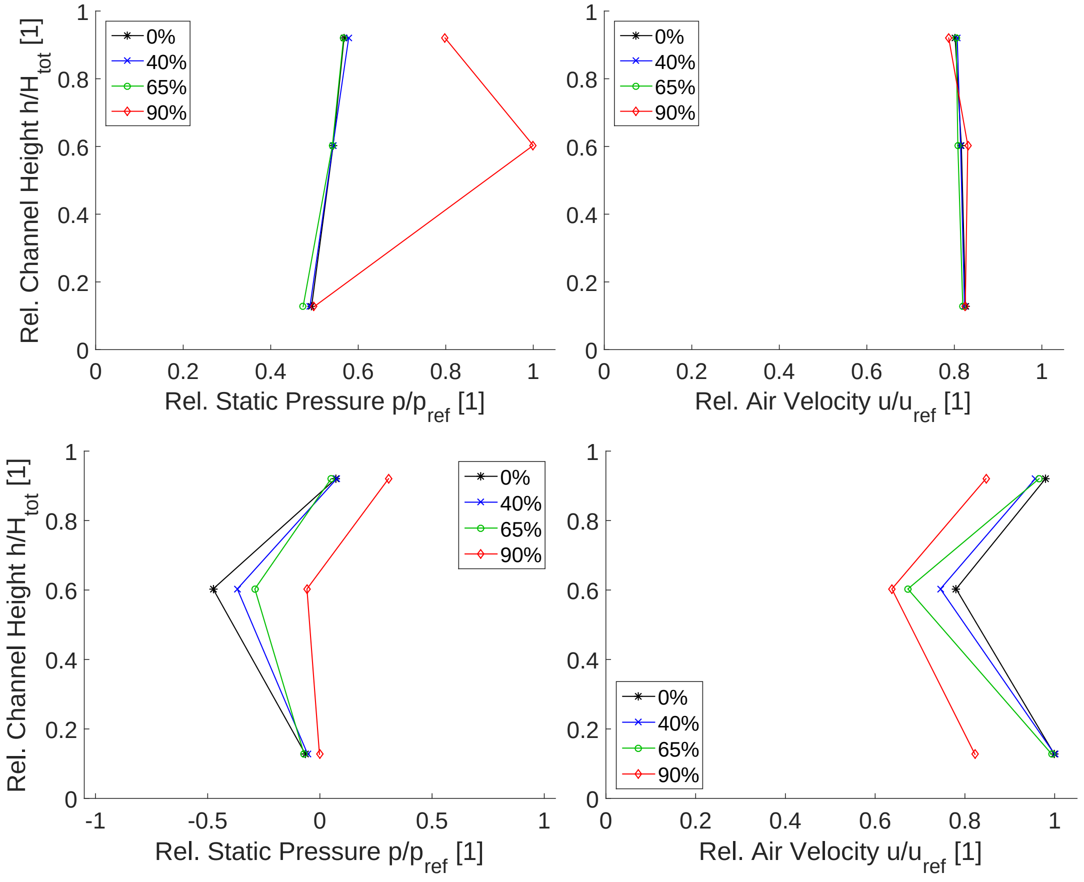

Figure D.2.: Case#1: air flow pressure (left) and velocity measurements (right) at the INLET plane (upper displays) and at the OUTLET plane (lower displays) at three vertical and four depth positions (i.e. depth in %, 0 % = mid channel, 90 % = nearest to the side wall).

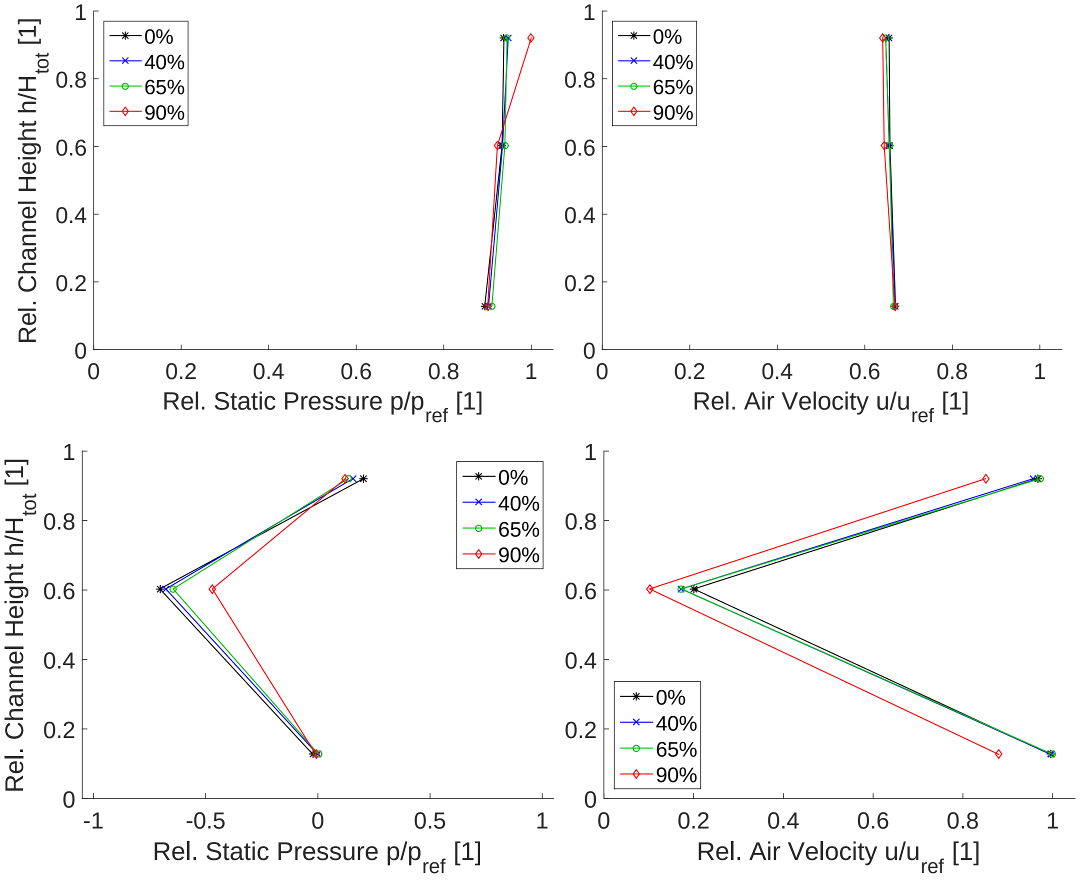

Figure D.3.: Case#4: air flow pressure (left) and velocity measurements (right) at the INLET plane (upper displays) and at the OUTLET plane (lower displays) at three vertical and four depth positions (i.e. depth in %, 0 % = mid channel, 90 % = nearest to the side wall).

D.3 Details of the air-flow validation study

A detailed comparison of the pressure and velocity profiles at the inlet and at the outlet measurement planes of the channel are shown in Fig. D.4 to D.5 for the cases #1 and #4. The predicted pressure and velocity trends are generally comparable to the experimental data.

The strong deviations of the predicted pressure profiles at the outlet for the low target angle cases (i.e. cases #1 and #2; case #1 is shown in Fig. D.4, lower left display) are accepted in order to achieve numerical stability of the solution by applying an opened boundary instead of static pressure at this position (for details see Section D.1). Due to very low absolute pressure values of the order of 100 Pa and the afterbody position of these deviations this local pressure field is assumed to be less influencing upon the particle tracks compared to the predicted air flow velocity profiles in these cases which match the experimental data well. Therefore those deviations are assumed to be acceptable in favour of a numerically stable solution.

In contrast to the low air velocity cases, the high air velocity cases numerically converged satisfactorily applying mass-flux inlet and static pressure outlet boundary conditions. In all cases the most significant differences between the numerical and the experimental data are found at the outlet planes and much lower deviations are found at the inlet planes (compare upper displays to lower displays in both figures).

The mean deviations between numerical and experimental data are summarized in Tab. D.3. The listing reveals that the velocity profiles are predicted with mean deviations in the range from 1 % to 16 %. Those deviations of the pressure profiles range from 3 % to 17 % but it must be noted that the deviations of the pressure profiles with low target angles are significantly higher. However, this situation was decided to be acceptable for the purpose of the simulations and this decision is discussed above.

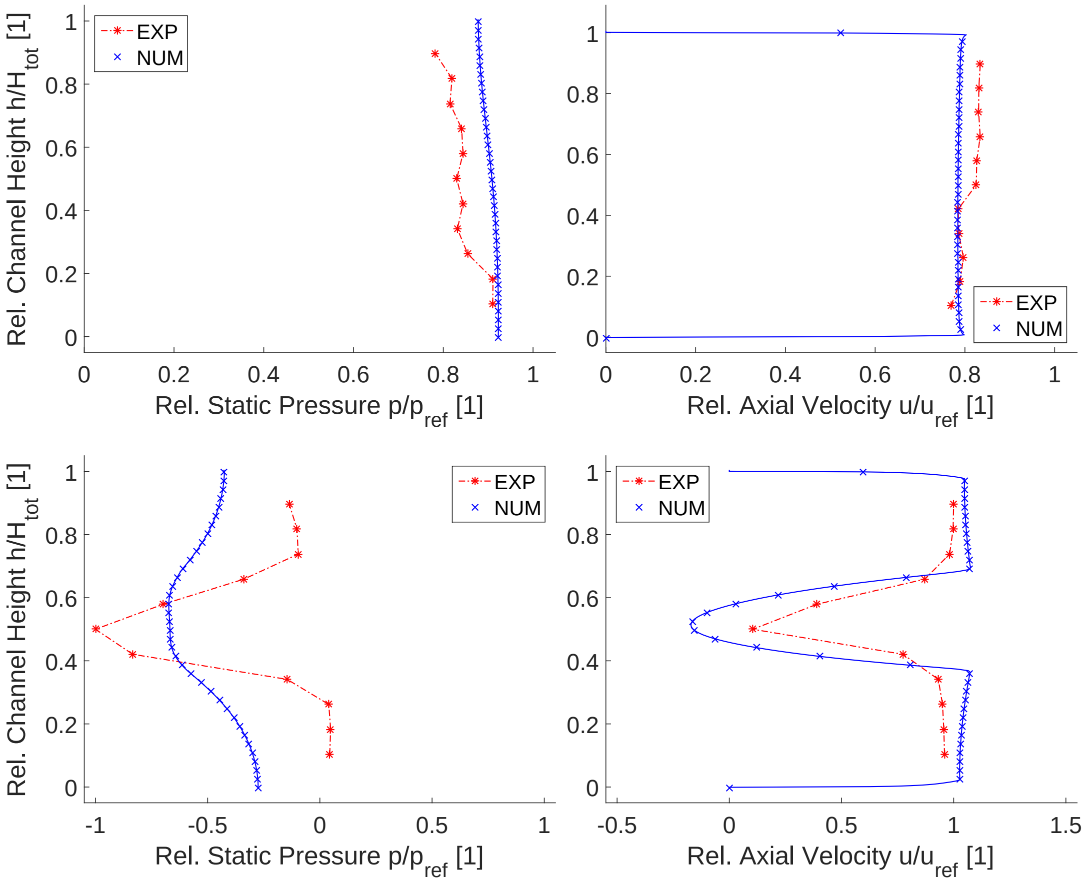

Figure D.4.: Case#1: air flow pressure (left) and velocity (right) profiles at the INLET plane (upper displays) and at the OUTLET plane (lower displays) - comparison of numerical to experimental data.

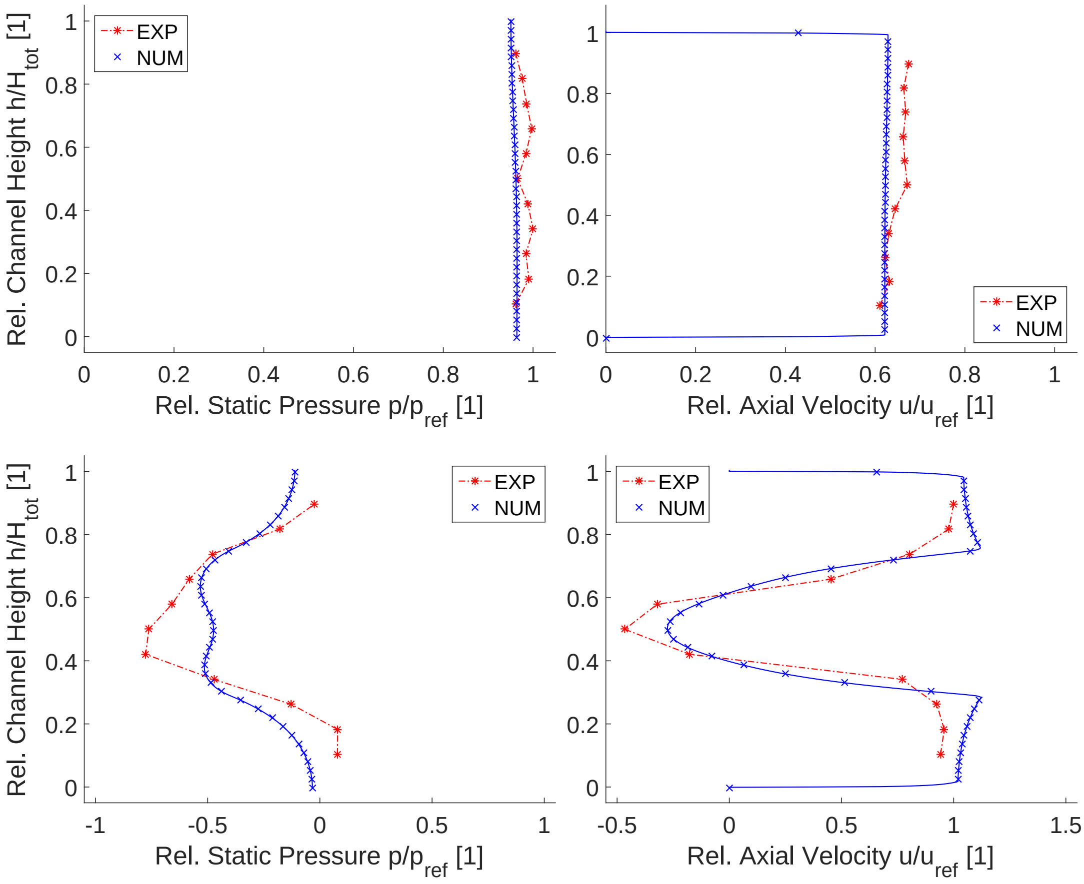

Figure D.5.: Case#4: air flow pressure (left) and velocity (right) profiles at the INLET plane (upper displays) and at the OUTLET plane (lower displays) - comparison of numerical to experimental data.

Case No	Air Inlet Velocity [m/s]	Air Outlet Velocity [m/s]	Air Inlet Pressure [Pa]	Air Outlet Pressure [Pa]	Particle Impact Velocity [m/s]	Particle Rebound Velocity [m/s]	Particle Impact Angle [°]	Particle Rebound Angle [°]
1	0.9602	0.9619	1.0719	*(1.7084)*	0.9893	1.0099	0.9566	1.1022
2	0.9521	0.9922	1.0936	*(1.7543)*	0.9570	0.9893	0.8820	1.1133
3	0.9514	1.1315	1.1627	1.0617	n.a.	n.a.	n.a.	n.a.
4	0.9496	1.1573	0.9779	0.8871	n.a.	n.a.	n.a.	n.a.

Table D.3.: Mean value comparison of validation data for air-flow and particle impingement.

D.4 Details of the particle breakup model set-up

This section describes the a-priori settings of various parameters of the particle breakup model implementation in Ansys CFX. These settings are necessary because there is a number of additional parameters applied in the CFX implementation of the breakup model and these are not originally contained in the model. However, these parameters are useful to avoid possible computational or memory exceptions caused by numerous breakup scenarios and huge amounts of secondary particles in large scale simulations. These parameters can be used for set-up and model calibration studies and they increase numerical robustness but decrease the degree of predictive capabilities of the model.

The most important additional parameters are:

- the total number of secondary particles n_{SEK},
- the number-rate of secondary classes $\dot{n}_i$,
- the maximum number of breakups n_{GEN},
- the minimum breakup diameter $d_{BU,min}$ and
- various random flags C_ξ.

The total number of secondary particles describes how many model particles are numerically generated by a primary particle impact. These secondary particles are distributed into the secondary size classes (i.e. residual, debris, dust dispersed and dust continuous) resulting in the secondary particle number rates.

By means of the maximum number of breakups it is possible to set a maximum limit of breakup processes in which a particle (either the primary particles or the secondary particles resulting from one particular primary particle) can participate. The minimum breakup diameter can be applied to clip the lowest size of particles considered for breakup and this is additional to the breakup boundary function presented in Section 5.3.3.

Finally it is possible to apply experimental randomness of secondary particle values by selecting the random flags for all data underpinned experimentally (i.e. number, diameters and velocity components of secondary particles).

To assess the above simplifications of a numerical set-up, the degree of abstraction is introduced

$$\Lambda_\phi = 1 - \frac{\min\left(\phi_{CFX}, \phi_{EXP}\right)}{\max\left(\phi_{CFX}, \phi_{EXP}\right)} \tag{D.1}$$

and it can be applied to each of the above variables (here ϕ). It relates model values (index: CFX) to real values (index: EXP) which are derived from the basic experiments. This assessment criterion is used in the model parameter overview given in Tab. D.4 and orders of magnitude are compared when dealing with the numbers of particles.

These settings represent a possible choice for later engine defouling simulations and therefore these are used for the validation case presented here. The maximum degree of abstraction takes place in the numbers of particles considered in the small particle size classes.

Model Parameter ϕ	Setting	Reality	Degree of Abstraction $\Lambda_\phi \cdot 100\%$
n_{SEK}	$\mathcal{O}\left(10^1\right)$	$\mathcal{O}\left(10^3\right)$	**99%**
$\dot{n}_{RES}$	$\mathcal{O}\left(10^0\right)$	$\mathcal{O}\left(10^1\right)$	90%
$\dot{n}_{DEB}$	$\mathcal{O}\left(10^1\right)$	$\mathcal{O}\left(10^2\right)$	90%
$\dot{n}_{DUST}$	$\mathcal{O}\left(10^1\right)$	$\mathcal{O}\left(10^3\right)$	**99%**
$\dot{n}_{CONT}$	$\mathcal{O}\left(10^0\right)$	$\mathcal{O}\left(10^4\right)$	**99%**
n_{GEN}	3	3	0%
$d_{BU,min}$	$80\mu m$	$20\mu m$	75%
C_ξ	1	1	0%

Table D.4.: Overview of model parameters and their impact upon the modelled degree of abstraction.

E Appendix to Chapter 8: Application case study

E.1 Details of the measurements in the test engine

A more detailed description of the probe positioning and of the measurement concept of the test engine is presented below.

The Prandtl probes (see Fig. 8.1) are positioned within the vane rows. For these experiments one vane is removed and the probe is installed in its place. This situation is shown in Fig. E.1. The total pressure holes are placed approximately at the axial position of the leading edges of the corresponding vanes and their radial position can be varied to measure flow profiles along the span of the blading. In the case of counter-current flows it is possible to turn the probes around the axis of the stator row and if the probes are turned by 180° their front bores are at the axial positions of the trailing edges of the corresponding vanes.

The data from the probes is recorded by a „Can-Bus“ system with a sample rate of 10 Hz and physical results are generated by means of a specially developed

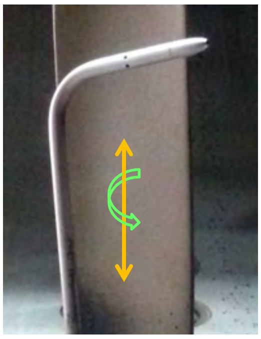

Figure E.1.: Typical position of Prandtl probe within stator row, degrees of freedom are indicated.

Position	Temp. range	Max. deviation	Pressure range	Max. deviation
AMB	-40 ... +400 °C	0.05 %	0 ... 105,000 Pa	0.09 %
BLMH	as above	as above	0 ... 250 Pa	9.5 %
BYPS	as above	as above	as above	as above
LPC-IGV to HPC-3	-40 ... +400 °C	0.05 %	0 ... 250 Pa	2.9 %
HPC-5 to HPC-14	as above	as above	0 ... 10,000 Pa	4.0 %

Table E.1.: Overview of measurement technique applied.

analysis code. Both shafts of the engine are equipped with separate revolution counters. Sensor details are given in Tab. E.1 below. The instrumentation of the engine was done by MUCKENHAUPT [IX]; details of the analysis code, calibration procedures, measurement strategy and an error chain analysis can be found in his thesis.

E.2 Details of the numerical set-up

Details of the numerical set-up used for the aircraft engine simulations are given below. The spatial discretization of the relevant numerical volumes are made by means of scalable block-meshing technique with respect to a fine resolution of the boundary layers (here no a priori estimation of the first cell height was made). The Ansys ICEM tool, version 16.2 was utilized and meshing details are presented in Fig. E.2 (note: only a proportion of the mesh is displayed to assure that the features are visible). In order to be able to efficiently simulate the particle laden defouling process it has been decided to use 100,000 grid-points per airfoil passage. Note that the meshing of the engine was carried out by Lufthansa Technik.

The boundary conditions used are total pressure and temperature at the inlet as well as open boundaries with static pressure and total temperature constraints at the outlet. A preliminary numerical study has been carried out to select the outlet boundary conditions. The boundary conditions of the particle phase

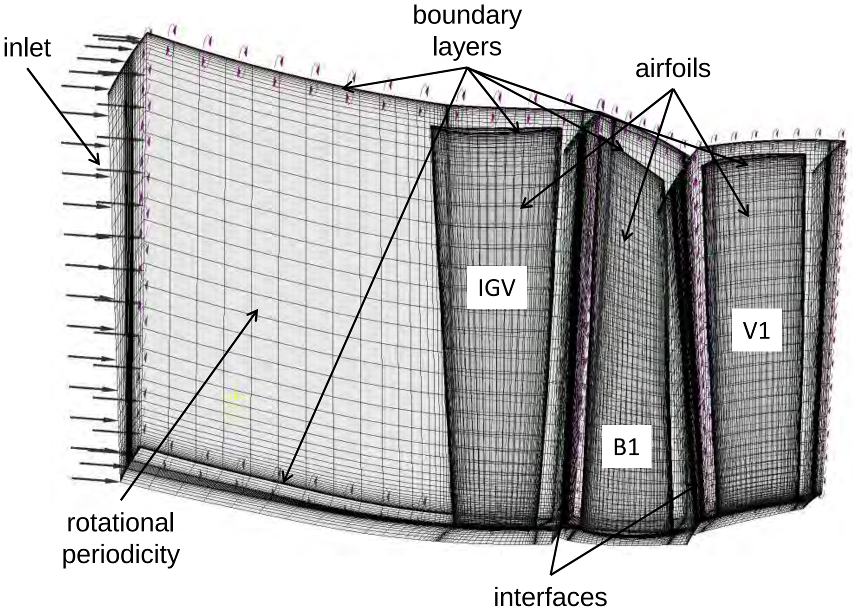

Figure E.2.: Details of a number of representative airfoil control volumes meshing for the defouling simulations (note: meshing was carried out by Lufthansa Technik).

are described in detail in Section 8.3. The most important grid and set-up information of the flow field simulations is summarized in Tab. E.2.

GRID	Scalable	Grid study	Mean elem. size [um]	No. of points per passage	Total no. of grid points	Boundary layer y+ size
	yes	no	1,000	100,000	3,700,000	n.a.

SET-UP	State	Turbulence	Pseudo Timestepping	Advection Schemes	Turbulence Numerics	Expert parameters
step1	steady	$k-\omega-SST$	physical, adaptive	Upwind	1st order	no
step2	steady	$k-\omega-SST$	physical, 1e-5 s	High-Res	High-Res	no

Table E.2.: Most important grid and set-up information of the engine simulations.

E.3 Details of the particle breakup model set-up

The most important model parameters of the new particle breakup model in Ansys CFX are calibrated for the engine defouling simulations (details about the calibration can be found in Section D.4) and this is done using a range of preliminary numerical convergence studies. The values determined by these studies are the cleaning pattern, the particle size distributions and the particle velocity distributions at various significant positions of the engine. The parameters used in the final defouling simulations are summarized in Tab. E.3.

Model Parameter ϕ	Setting LPC	Setting HPC	Simulated Magnitude	Real Magnitude
n_{SEK}	19	19	$\mathcal{O}\left(10^1\right)$	$\mathcal{O}\left(10^3\right)$
$\dot{n}_{RES}$	3	3	$\mathcal{O}\left(10^0\right)$	$\mathcal{O}\left(10^1\right)$
$\dot{n}_{DEB}$	6	6	$\mathcal{O}\left(10^0\right)$	$\mathcal{O}\left(10^2\right)$
$\dot{n}_{DUST}$	9	9	$\mathcal{O}\left(10^1\right)$	$\mathcal{O}\left(10^3\right)$
$\dot{n}_{CONT}$	1	1	$\mathcal{O}\left(10^0\right)$	$\mathcal{O}(10^4)$
n_{GEN}	12	28	n.a.	n.a.
$d_{BU,min}$	$1500\,\mu m$	$105\,\mu m$	n.a.	n.a.
C_ξ	1	1	n.a.	n.a.

Table E.3.: Overview of model parameter settings and their impact upon the modelled degree of abstraction.

List of Publications

[I] RUDEK, Arthur; RUSS, Gerald; DUIGNAN, Barry; An Experimental and Numerical Validation Study of Particle Laden Supersonic Flows; Paper presented at the 9th International Conference on Multiphase Flow, Firenze, Italy (2016)

[II] RUDEK, Arthur; RUSS, Gerald; DUIGNAN, Barry; Particle laden flow investigations in special purpose dry-ice blasting applications; International Journal of Computational Methods and Experimental Measurement, Vol. 4, pp. 393-402 (this paper was also presented at the 11th International Conference on Advances in Fluid Mechanics, Ancona, Italy (2016))

[III] BERGHOFF, Gerrit; Numerical simulation of CO_2 dry-ice blasting nozzles (in German); Master-Thesis, Hochschule Darmstadt (2017)

[IV] ZITZMANN, Thomas-Alexander; Development of an experimental test-rig for investigations of the breakup process of CO_2 dry-ice; Master-Thesis, Hochschule Darmstadt (2015)

[V] LUONG, Hung; Detailed experiments on particle breakup and erosive defouling in dry-ice based aircraft engine defouling applications; Master-Thesis, Hochschule Darmstadt (2017)

[VI] REIS, Patrick; Verification and validation study of the hda particle breakup model in Ansys CFX; Master-Thesis; Hochschule Darmstadt (2017)

[VII] RUDEK, Arthur; ZITZMANN, Thomas-Alexander; RUSS, Gerald; DUIGNAN, Barry; An energy-based approach to assess and predict erosive airfoil defouling; International Journal of Computational Methods and Experimental Measurement, Vol. 6, pp. 476-486 (this paper was also presented at the 9th International Conference on Materials and Contact Characterization, Tallinn, Estonia (2017))

[VIII] MUCKENHAUPT, David; SCHIEMER, Bjoern; Development of a wind-tunnel experiment for the validation of the hda particle breakup model for dry-ice; Internal Seminar Paper; Hochschule Darmstadt (2017)

[IX] MUCKENHAUPT, David; Development of a new datalogging concept for the hda aircraft engine test-rig; Bachelor-Thesis; Hochschule Darmstadt (2015)

[X] ENGEL, Mario; Optical high-speed camera measurements of particle laden flows inside the high-pressure compressor of an aircraft engine; Master-Thesis; Hochschule Darmstadt (2015)

[XI] ROSSMEISSL, Daniel; Throttling experiments towards a possible performance analysis of aircraft engines operating at low rotational speeds; Master-Thesis; Hochschule Darmstadt (2016)